博士論文

An application of the MaxEnt/fragment EP method to ferroelectric polarization analysis

(マキシマムエントロピー法による静電ポテンシャルフラグメント解析法の強誘電分極解析への応用)

金 栄勲

博士論文

An application of the MaxEnt/fragment EP method to ferroelectric polarization analysis

(マキシマムエントロピー法による静電ポテンシャルフラグメント解析法の強誘電分極解析への応用)

金 栄勲

Table of Contents

List of Figures

List of Tables

Chapter 1

Introduction

Designing and controlling of intense local polarization in solids are vital for emerging electronics, such as high-performance field-effect transistors, Ferroelectric Random Access Memories (FeRAMs) and multiferroic devices in nano-scale.[1~8] The use of spontaneous polarization is one of the most convincing approaches to achieving this. On a parallel with the evolution from magnetics to spintronics, control of individual electric dipole is a key technology in dielectrics. Neither microscopic characterization nor design of individual dipoles, however, has been intensively investigated so far: the properties have been mainly described in terms of macroscopic properties based on measurements of dielectric permittivity and electric polarization *P* under electric field *E* for bulk samples.[9] The method is, however, restricted to the sample conditions such as single crystal with measurable shape or enough quantity of powder samples for fabricating ceramic sample. For other methods of polarization-estimation, there are theoretical calculation[10~13] and point charge model[14~15]. Theoretical calculation evaluates the polarization using the Born-effective charge and the band structure obtained by the optimized structure. However, obtained results are strongly dependent to the calculation method such as choice of exchange-correlation function. In

point charge model, polarization is calculated by using relative displacement of oppositely charged ions and formal charge of each ion. Although this method can estimate the local polarization, the calculated polarization value shows a difference from the observed value, because covalent characteristic and/or electronic polarization are not considered in the model. Thus, the method of estimation of local polarization has not been investigated yet; microscopic behavior of polarization has not been fully explored yet.

In order to visualize a microscopic structure strongly related to the property of material, the study of charge density level structure has been rapidly progressed by means of Maximum Entropy Method (MEM) based on Synchrotron Radiation X-ray diffraction data.[16~20] Recently, based on the MEM results, a method of electrostatic potential (MaxEnt/EP) analysis has been developed[21,22]; it has successfully visualized the structural characteristics directly related to the physical property[23~27], such as emergence of ferroelectricity by enhanced electronic/ionic polarization, magnetic property change by charge transfer between ions, and thermal conductivity affected by rattling behavior of atom/molecule and so on.

In this research, an estimation method of the local/total polarization in the crystal structure was developed based on the MaxEnt/EP analysis *via* Synchrotron Radiation X-ray powder diffraction; the fragment concept was introduced for the estimation of the local polarization as well as total polarization with free cell-choice. We call this procedure the MaxEnt/fragment EP method. For validity test of this method, well-known Perovskite materials were used. Furthermore, we applied the MaxEnt/fragment EP method to the polarization-estimation of lead-free ferroelectric material Bi_2SiO_2.

In chapter 2, the theoretical background for ferroelectricity strongly coupled with

structural characteristics, analysis of the electron charge density level structure by means of MEM electron charge density and electrostatic potential, and the process of local polarization estimation by the MaxEnt/fragment EP method were explained. Chapter 3 describes Synchrotron X-ray powder diffraction experiment for a precise structural analysis and the details of the MaxEnt/EP analysis for materials. In chapter 4, the validity of the MaxEnt/fragment EP method was investigated with well-known Pervoskite materials, $PbTiO_3$ and $BaTiO_3$. Obtained polarization results were compared to the previously reported results. In Chapter 5, we studied ferroelectric polarization of recently developed Pb-free ferroelectric material, Bi_2SiO_5 by the MaxEnt/fragment EP method. Chapter 6 summarized the thesis and presents future plan.

Chapter 2

Theoretical Background

Ferroelectric polarization is strongly correlated to the degree of bonding distortion and the asymmetrical electron density distribution of atoms or molecules in the crystal structure. Therefore, investigating the electron charge density distribution and the crystal structure in a ferroelectric material is indispensable in understanding ferroelectric polarization and in designing high performance of the material.

In this research, we developed new method for estimation of the ferroelectric polarization in the crystal structure by means of MEM electron charge density analysis combined with electrostatic potential (EP) analysis via Synchrotron Radiation X-ray powder diffraction. Thus, in the chapter 2, the fundamental framework for the research is explained; (1) we studied the crystallographic point group for ferroelectricity. (2) The method of MEM charge density and EP are replicated for the charge density level structure study. (3) The method of polarization estimation is explained based on the result of MEM charge density and EP.

2.1 Ferroelectricity and crystal structure

A dielectric material is defined as an electrical insulator that can be polarized by an applied external field.[28~30] The displacement of charge in an atom or molecule gives rise to an electrical dipole moment. Polarization is generated by the alignment of internal electric dipole moments by the applied external electric field. Dielectric materials can be categorized by several subclasses on the basis of physical property.[31] Figure 2.1 shows the several groups of dielectric materials. Piezoelectric materials have the property of converting the applied stress to electrical energy and vice versa. Pyroelectric materials generate an electrical potential under the influence of temperature gradients. Ferroelectricity has the spontaneous polarization below the Curie temperature, which can be reversed between equilibrium states by the external applied field. It should be noted that Ferroelectric materials are a subgroup of the polar materials and are both pyroelectric and piezoelectric materials. It means that all ferroelectric materials can have piezoelectric effect, while not all piezoelectric and pyroelectric materials are ferroelectric.

Most ferroelectric materials undergo a structural phase transition at the Curie temperature from high temperature paraelectric state to low temperature ferroelectric state.[32] The symmetry of ferroelectric phase is always lower than the that of the paraelectric phase. The spontaneous polarization is defined as the net electric dipole moment per unit volume. It is strongly related to the arrnagement of electric dipole moment in the crystal. Generally, it has been known that ferroelectricity can be generated only in specific crystal structures which have a unit polar axis. Therefore, whether or not a material can have ferroelectricity is determined solely by its crystal structure, in other words, point group symmetry.

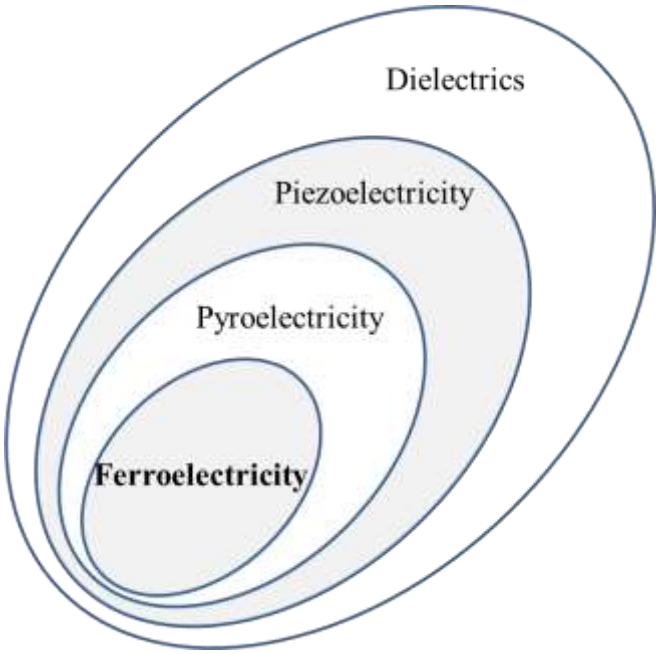

Figure 2-1. Classification of dielectric, piezoelectric, pyroelectric and ferroelectric materials.

A crystallographic point group is characterized by a set of symmetry elements such as rotations, mirror plane, center of symmetry, rotary inversion.[33] The elements of a point group are generally termed point symmetries. The number of point groups is infinite. However, limited rotation symmetry for point groups is employed such as 60 °, 90 °, 120 ° and 180 °. It results in only 32 different possible crystallographic point groups for the three-dimension.

In addition to the symmetry operations of the point group, the space group is a description of the symmetry in the structure.[34] The combination of the 32 crystallographic point groups with the 14 Bravais lattices compromise the 230 different space groups in

three-dimension. They are expressed by the translational symmetry of a unit cell and the point group symmetry operations such as improper rotation, reflection and rotation; the screw axis and the glide plane symmetry operations should be also considered because the space groups show the translational symmetry operation in contrast to the point groups.

Symbols of the 32 crystallographic point groups with the Bravais lattice are shown in Figure 2-2. Black colored symbols have the inversion symmetry operation. The materials with the inversion symmetry operation cannot have a polar property because electric dipole moments are canceled out each other; it leads paraelectric property. Of the remaining 21 point groups, the 20 point groups have electrical polarity by the external stress; they can exhibit the piezoelectric effect. The *O* point group (Cubic 432) has non-piezoelectric property because the piezoelectric charges generated along the [111] polar axes cancel out each other. Blue colored 10 point groups have no unique polar axis, and they are excluded from the piezoelectric classes. Ferroelectricity can be contained by only 10 red colored point groups, which have a unique polar axis. This classification is illustrated in Figure 2-2.

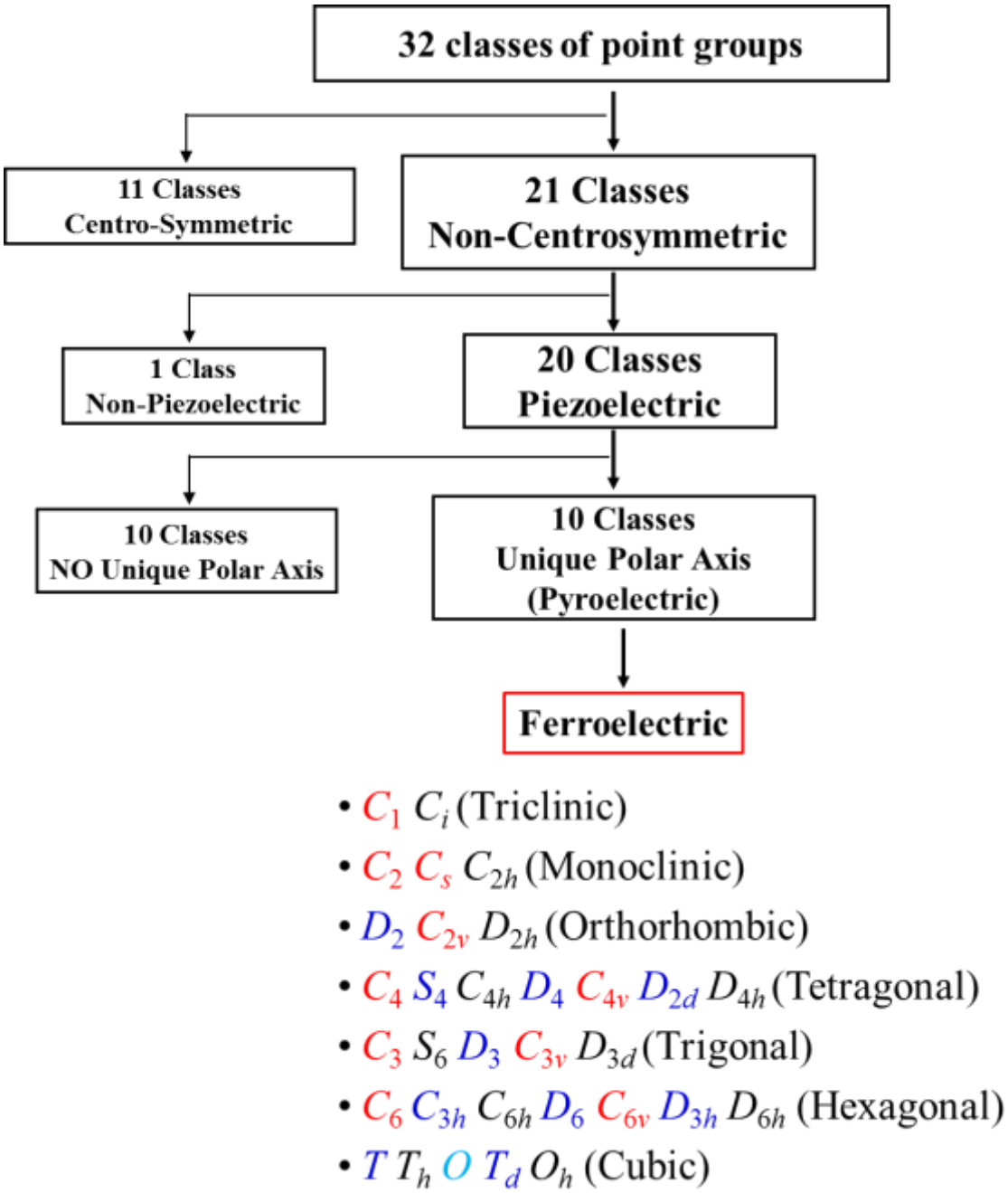

Figure 2-2. Flow chart of point groups for ferroelectricity and symbols of 32 point groups with the Bravais lattice.

As it was quoted, a unique polar axis is not the direct meaning of ferroelectricity. The schematic view of behaviors for ferroelectric, antiferroelectric and pyroelectric is shown in Figure 2-3. In the Figure 2-3, T_c is the Curie temperature and E is the applied electric field which has direction from left to right. When the temperature is above the Curie temperature, they have cubic structure which has the inversion symmetry. They have not net dipole moment in the unit cell, and it causes the paraelectric state. When the temperature is below the Curie temperature, they show the net dipole moment in the unit cell. For ferroelectric and pyroelectric state, dipole moments of each unit cell are oriented to the same direction. On the other hands, for antiferroelectric state, dipole moments of each unit cell have different direction, and it generates the no net polarization in the whole crystal. If the external electric field is applied at the temperature below the Curie temperature, electric dipole moments in the unit cell for ferroelectric and antiferroelectric state are reoriented to the direction of the applied field. However, there is no movement of electric dipole moments in the pyroelectric state by the applied field. This unique property of ferroelectricity, reversible spontaneous polarization by the electric field, allows the ferroelectric materials to be applied at various industrial areas.

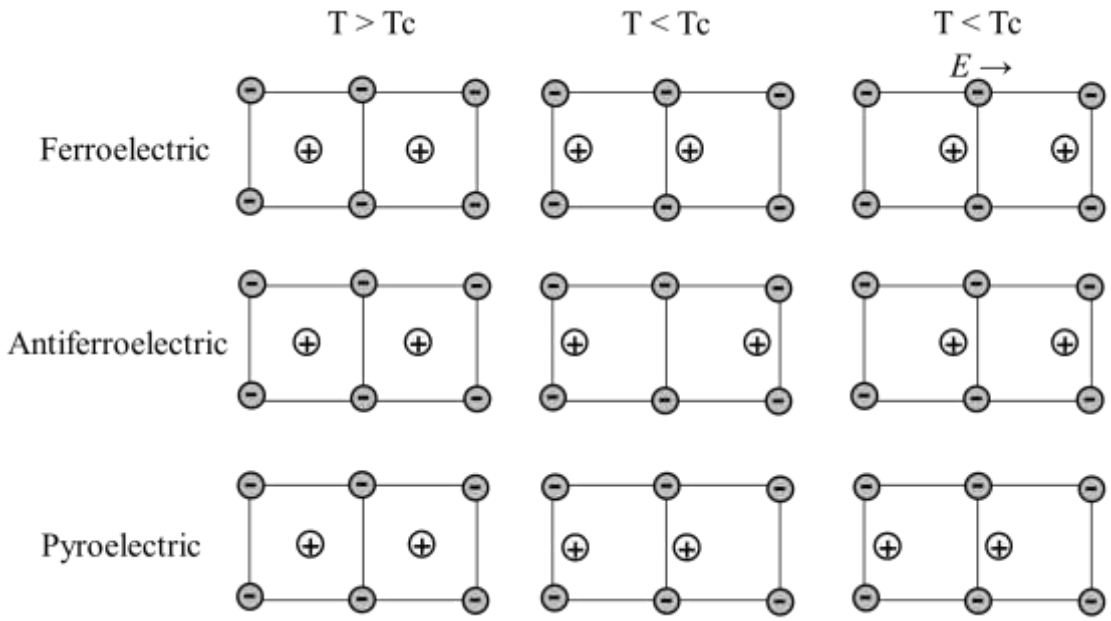

Figure 2-3. Schematic representation of electric dipole moments in ferroelectric, antiferorelectric and pyroelectric state.

2.2 Determination of the electron density level structure by means of X-ray diffraction

2.2.1 X-ray diffraction

X-ray interacts with electron to emit radiation at the same wavelength as the incident X-ray: this process is called Thomson scattering and expressed by the following equation:

$$I = \frac{I_0}{r^2}\left[\frac{e^2}{m_e c^2}\right]^2 \frac{1 + cos^2(2\theta)}{2} \tag{2.1}$$

where I_0 is the intensity of the incident X-ray, r is the distance from scattering electron to the observation position, e is the electron charge, m_e is the mass of the electron and c is the speed of light. The cosine term is the polarization factor indicating that the incident non-polarized beam is polarized.

Atom is composed of the electron clouds around the nucleus. When the X-ray is incident to atom, scattering by an atom is the sum of the scattering of the electron clouds. Because X-rays are also scattered from the different electron clouds part in the atom, there is a path difference between the scattered X-rays as shown Figure 2-4. It is more convenient to express the path difference in terms of an angle, phase difference:

$$Phase\ difference = (MQ + QN) \times 2\pi = 2\pi\{\boldsymbol{r_{21}} \cdot (\boldsymbol{s_0} - \boldsymbol{s})\} = 2\pi \boldsymbol{r_{21}} \cdot \boldsymbol{S} \tag{2.2}$$

If the phase difference is some integer multiple of the wavelength, constructive interference of the scattered X-rays occurs; if the phase difference is a non-integer number of wavelength, destructive interference occurs. Total scattering from the atom is obtained by

summing the electron density contribution $\rho(\boldsymbol{r})$ in volume element dv with a phase difference $\exp\{2\pi i(\boldsymbol{r}\cdot\boldsymbol{S})\}$, and it is expressed as:

$$f(\boldsymbol{S}) = \int_V \rho(\boldsymbol{r})\exp\{2\pi i(\boldsymbol{r}\cdot\boldsymbol{S})\}dv \tag{2.3}$$

, where $f(\boldsymbol{S})$ is the atomic scattering factor. The value of scattering factor at the zero scattering angle is equal to the number of electrons in atom. In real situation, atomic scattering factor is modified due to the anomalous dispersion caused by photoelectric effect and the thermal motion of the atoms.

Crystal has a set of atoms arranged periodically in 3 dimensions. Repeating unit is called unit cell. If the electron density $\rho(\boldsymbol{r})$ from each atom is supposed to have spherical distribution and not overlapped, schematic view for unit cell can be represented as in Figure 2-5.

In the Figure 2-5, a parallelogram means unit cell and circles are the electron density from each atom. $\boldsymbol{r_j}$ is the potion of *j*th atom and $\boldsymbol{r_j'}$ is the position of the electron from the nucleus. Thus, ***r*** and $\rho(\boldsymbol{r})$ can be written as:

$$\boldsymbol{r} = \boldsymbol{r_j} + \boldsymbol{r_j'} \tag{2.4}$$

$$\rho(r) = \sum_{j=1}^{n} \rho(\boldsymbol{r_j'}) \tag{2.5}$$

F(***S***), scattering factor in the whole unit cell, can be described as the scattering factor from an atom:

$$F(S) = \int_V \rho(r)\exp\{2\pi i(\boldsymbol{r}\cdot\boldsymbol{S})\}dv \tag{2.6}$$

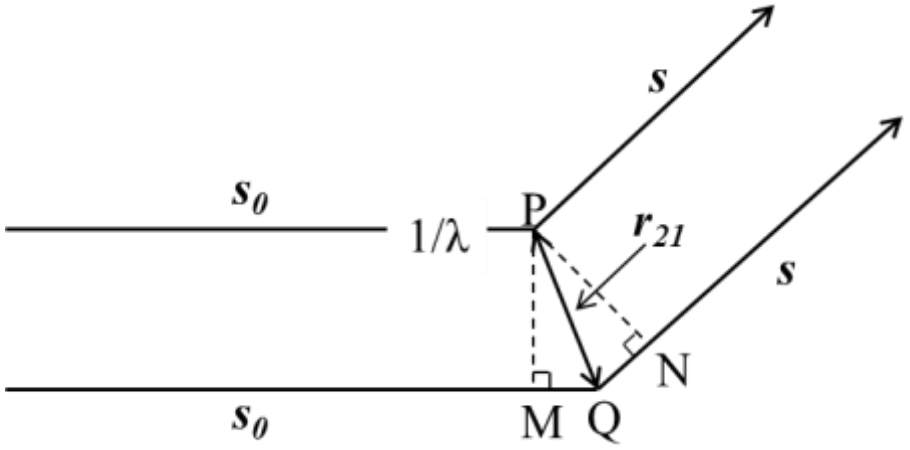

Figure 2-4. Path difference between the scattered X-rays.

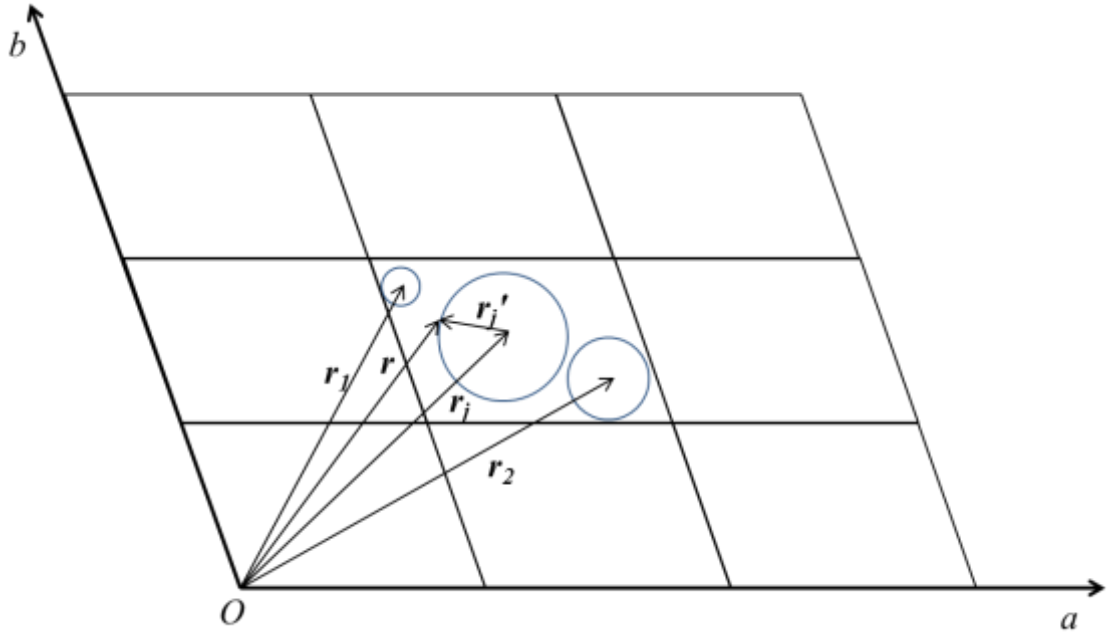

Figure 2-5. Schematic view for unit cell with the electron density.

From equation (2.4) and (2.5), equation (2.6) can be rewritten:

$$F(S) = \int_V \sum_{j=1}^{n} \rho(\boldsymbol{r}_j') \exp\left[\, 2\pi i\{(\boldsymbol{r}_j + \boldsymbol{r}_j') \cdot \boldsymbol{S}\}\right] dv$$

$$= \sum_{j=1}^{n} \int_V \rho(\boldsymbol{r}_j') \exp\{2\pi i(\boldsymbol{r}_j + \boldsymbol{r}_j') \cdot \boldsymbol{S}\} dv \cdot \exp\{2\pi i(\boldsymbol{r}_j \cdot \boldsymbol{S})\} \tag{2.7}$$

Since $\int_V \rho(\boldsymbol{r}_j') \exp\{2\pi i(\boldsymbol{r}_j + \boldsymbol{r}_j') \cdot \boldsymbol{S}\} dv$ is the same as atomic scattering factor, equation (2.7) is expressed as:

$$F(\boldsymbol{S}) = \sum_{j=1}^{n} f(\boldsymbol{S}) \exp\{2\pi i(\boldsymbol{r} \cdot \boldsymbol{S})\} \tag{2.8}$$

where $F(\boldsymbol{S})$ is the structure factor related to the atomic scattering factor of each atom and the phase difference. Structure factor is obtained from the Fourier transformation of the electron density $\rho(\boldsymbol{r})$ as shown in equation (2.6). In mathematically, the Fourier inversion transform is also possible for the function which was transformed. Thus, equation (2.8) can be written:

$$\rho(\boldsymbol{r}) = \frac{1}{V} \int_V F(\boldsymbol{S}) \exp\{-2\pi i(\boldsymbol{S} \cdot \boldsymbol{r})\} dv \tag{2.9}$$

where V is the volume of unit cell and integration is carried out over elements dv. In addition, the system is involved to periodic arrangement of unit cell. Therefore, equation (2.9) can be expressed as summation form:

$$\rho(\boldsymbol{r}) = \frac{1}{V} \sum_{S} F(\boldsymbol{S}) \exp\{-2\pi i(\boldsymbol{S} \cdot \boldsymbol{r})\} \tag{2.10}$$

where the summation is over all the structure factors. According to equation (2.10), electron density can be calculated at any point by the Fourier transformation of the obtained

structure factors. This is a basic idea for determination of electron density.

2.2.2 Maximum Entropy Method (MEM) for the electron charge density

There are conventional methods such as Fourier transform and difference Fourier synthesis to find the electron density from experimental data. As indicated at equation (2-10), direct Fourier transformation of observed structure factors is the electron density.[35,36] In mathematically, it requires infinite number of the structure factors to obtain the perfect electron density in the material. However, the condition is not satisfied with the experimental measurement. Unknown structure parameters are treated as zero value in the calculation process, and it causes the negative electron density. To complement the Fourier transform for the electron density, difference Fourier synthesis is used.[37] It finds the difference of electron density ($\Delta\rho$), not the electron density (ρ) by subtracting structure factors between $F_{\text{obs}}(hkl)$ from the measurement and $F_{\text{model}}(hkl)$ from the structure model, as shown following equation:

$$\Delta\rho(x,y,z)=\frac{1}{V}\sum_{h}\sum_{k}\sum_{l}\left[F_{\text{obs}}(hkl)-F_{\text{model}}(hkl)\right]\exp\left\{-2\pi i(hx+ky+lz)\right\} \qquad (2.11)$$

$\Delta\rho$ is related to covalent or delocalized electrons. If there is a large positive $\Delta\rho$ in the result, it means that there is electron density in the measured data which is not considered in the model. If the difference is very small, it means that an atom exists in that position. However, this method requires the structural model and it cannot directly find the value of ρ.

The Maximum Entropy Method (MEM) is developed to find the most probable value

of electron charge density based on the information theory.[38] It extracts information as much as possible from the measurement data. D. M. Collins[39] suggested the MEM can be applied to the charge density study with the limited number of observed data. It provides the least biased charge density distribution in a unit cell.

The entropy (*S*) equation for the information of the charge density is expressed as:

$$S = -\sum_{r} \rho'(\boldsymbol{r}) \ln \frac{\rho'(\boldsymbol{r})}{\tau'(\boldsymbol{r})} \tag{2.12}$$

Dimensionless variables, the probability $\rho'(\boldsymbol{r})$ and the prior probability $\tau'(\boldsymbol{r})$, in the equation are connected with the actual charge density by:

$$\rho'(\boldsymbol{r}) = \rho(\boldsymbol{r}) / \sum_r \rho(\boldsymbol{r}) \text{ and } \tau'(\boldsymbol{r}) = \tau(\boldsymbol{r}) / \sum_k \tau(\boldsymbol{r}) \tag{2.13}$$

where $\rho(\boldsymbol{r})$ is the electron density and $\tau'(\boldsymbol{r})$ is the prior electron density at a pixel in a unit cell. $\rho(\boldsymbol{r})$ is distributed within whole unit cell as:

$$\rho'(\boldsymbol{r}) = \rho(\boldsymbol{r}) / Q_{\text{total}} \tag{2.14}$$

where Q_{total} is the total number of electrons in a unit cell. The entropy is maximized following to the constraint

$$C = \frac{1}{N} \sum_{k} \frac{|F_{obs}(\boldsymbol{k}) - F_{cal}(\boldsymbol{k})|^2}{{\sigma_k}^2} \tag{2.15}$$

where *N* is the number of structure factors used in the MEM analysis, σ_k is the standard deviation of the observed structure factor, $F_{obs}(\boldsymbol{k})$ and $F_{cal}(\boldsymbol{k})$ is the calculated structure factor by

$$F_{cal}(\boldsymbol{k}) = V \sum_{r} \rho(\boldsymbol{r}) \exp(-2\pi i \boldsymbol{r} \cdot \boldsymbol{k}) \tag{2.16}$$

where *V* is the unit cell volume. If the calculated structure factors are in a good agreement

with the observed structure factors, the value of *C* becomes 1.

Lagrange's method of undetermined multiplier is applied to constrain the equation (2.15) to be 1 while keeping the entropy in the equation (2.12) maximized. Then, we have

$$Q(\lambda) = \mathrm{S} - \frac{\lambda}{2}C$$

$$= -\sum_{r} \rho'(\boldsymbol{r}) \ln \frac{\rho'(\boldsymbol{r})}{\tau'(\boldsymbol{r})} - \frac{\lambda}{2}C \tag{2.17}$$

By setting

$$\frac{\partial Q(\lambda)}{\partial \rho(\boldsymbol{r})} = 0 \tag{2.18}$$

$$F_{cal}(\boldsymbol{k}) = V \sum_{r} \tau(\boldsymbol{r}) \exp(-2\pi i \boldsymbol{r} \cdot \boldsymbol{k}) \tag{2.19}$$

We have,

$$\rho(\boldsymbol{r}) = \tau(\boldsymbol{r}) \exp[\frac{\lambda F_0}{N} \sum_{k} \frac{1}{\sigma(\boldsymbol{k})^2} \{F_{obs}(\boldsymbol{k}) - F_{cal}(\boldsymbol{k})\} \exp(-2\pi i \boldsymbol{k} \cdot \boldsymbol{r})] \tag{2.20}$$

where F_0 is the total number of electrons in a unit cell. Equation (2.20) can be solved through iteration method from the initial density for the prior distribution. Reliability for MEM analysis was evaluated by the R_{MEM} factor:

$$R_{MEM} = \frac{\sum_k |F_{obs}(\boldsymbol{k}) - F_{cal}(\boldsymbol{k})|}{\sum_k |F_{obs}(\boldsymbol{k})|} \tag{2.21}$$

With this method, it is possible to estimate the accurate charge density distribution by considering the missing structure factors from the experiment with the most probable values.

2.2.3 Visualization of electrostatic potential

Electrostatic potential has provided insight into electrical interaction between charges, positively charge nuclei and negatively charged electron clouds. It is related to dipole moment, electronegativity and partial charges of the molecules in the crystal structure. Therefore, electrostatic potential method can visualize the polarization of a molecule. In positive electrostatic potential region, repulsion between nuclei is dominant with low concentration of the electron density. On the other hand, region of negative electrostatic potential corresponds to high concentration of the electron density. Large difference of electrostatic potential value between molecules or atoms in the structure is strongly related to ionic polarization. In this study, electrostatic potential is estimated with the method developed by M. Tanaka *et al*.[21,22] Because this electrostatic potential analysis is based on the MEM charge density from Synchrotron Radiation X-ray diffraction experiment, all molecules or atoms in the unit cell are considered.

Electrostatic potential is composed of the positively charged nucleus and negatively charged electron clouds contribution:

$$U(\boldsymbol{r}) = U_{nuc}(\boldsymbol{r}) + U_{ele}(\boldsymbol{r}) = \sum_{l}\sum_{t}\frac{Z_t}{|\boldsymbol{r}-\boldsymbol{l}-\boldsymbol{R_t}|} - \int\frac{\rho(\boldsymbol{r})}{\boldsymbol{r}-\boldsymbol{r'}}d\boldsymbol{r'} \qquad (2.22)$$

where Z_t, $\boldsymbol{l}$, and $\boldsymbol{R_t}$ are the atom number of the *i*th basis atom, the lattice point vector, and the position vector of the *i*th basis atom relative to the lattice point, respectively.

The electrostatic potential caused by the electron charge density can be calculated in the reciprocal space $\boldsymbol{G}$:

$$U_{ele}(\boldsymbol{r}) = -4\pi \sum_{G} \frac{\tilde{\rho}(\boldsymbol{G})\exp(i\boldsymbol{G}\boldsymbol{r})}{|\boldsymbol{G}|^2} \tag{2.23}$$

where $\boldsymbol{G}$ is the reciprocal vector. $\tilde{\rho}(\boldsymbol{G})$ is the Fourier transformation of the charge density. $\tilde{\rho}(\boldsymbol{G})$ is related to the structure factor $F(\boldsymbol{G})$ by the relation, $F(\boldsymbol{G}) = V\tilde{\rho}(\boldsymbol{G})$ with the volume of the unit cell V in real space. Therefore, equation (2.23) can be rewritten by

$$U_{ele}(\boldsymbol{r}) = -4\pi \sum_{G} \frac{F(\boldsymbol{G})\exp(i\boldsymbol{G}\boldsymbol{r})}{V|\boldsymbol{G}|^2} \tag{2.24}$$

However, it is practically difficult to get a sufficient number of structure factors from the experiment to get a converged value from equation (2.22). In order to solve this problem, the structure factor from MEM analysis, $F_{cal}(\boldsymbol{G})$, is applied to extrapolate the structure factors for convergence of equation (2.22).

For the electrostatic potential by the positive nucleus charge, Ewald's method is used based on the atom position from Rietveld refinement. The final equation for total electrostatic potential is expressed as:

$$\begin{aligned} U(\boldsymbol{r}) = 4\pi \sum_{G} \frac{\sum_t Z_t \, exp\left(-\frac{|\boldsymbol{G}|^2}{\eta^2} - i\boldsymbol{G}\boldsymbol{R_t}\right) - F_{cal}(\boldsymbol{G})}{V|\boldsymbol{G}|^2} \times exp(i\boldsymbol{G}\boldsymbol{r}) \\ + \sum_{l}\sum_{t} \frac{Z_t}{|\boldsymbol{r} - \boldsymbol{l} - \boldsymbol{R_t}|} erfc(\eta|\boldsymbol{r} - \boldsymbol{l} - \boldsymbol{R_t}|) \end{aligned} \tag{2.25}$$

where $erfc(x)$ is the complementary error function and η is the parameter for rapid convergence of the calculation.

Electric field is calculated by the minus gradient of electrostatic potential at each point. It is shown as black arrows in the Figure 2.7 which shows electrostatic potential of the SiO_3 layer in Bi_2SiO_5 colored from -30 V to 314 V. Electric fields are directed from the

atom position to outward and perpendicular to surface of constant electrostatic potential. In the low electrostatic potential region, change of electric field is more clearly distinguished than that of electrostatic potential. Electric fields encounter other electric fields from other atom at the position of the local minimum electrostatic potential to make the boundary. The region enclosed by the boundary is called fragment in this research. Total number of electron charge in the fragment is same with total nucleus charge, showing the charge neutrality of fragments. This can be explained by Gauss theorem.[40,41] As it was explained, boundary of fragments is determined by following the local minimum point of electrostatic potential. And the derivative of a function, electrostatic potential dependent to bond length, at the local minimum is 0. An Electric field is the minus gradient of potential:

$$\boldsymbol{E} = -\nabla V_E \tag{2.26}$$

where $\boldsymbol{E}$ is the electric field and V_E is the electrostatic potential. Thus, value of electric field at the local minim of electrostatic potential is 0. Gauss's law says that the net flux of the electric field through a closed surface is proportional to the enclosed electric charges. This law can be expressed as:

$$\oiint_S^a \epsilon_0 \boldsymbol{E} \cdot dS = \iiint_V^a \rho \, dV \tag{2.27}$$

where ϵ_0 is the vacuum permittivity and ρ is the volume of enclosed surface. For fragment, the closed surface which is the determined boundary has no value of electric field. As a result, total number of charges within fragment is 0, and it means that net charge of fragment is neutral. Because fragment should have the charge neutrality by the Gauss theorem, it can be used as the criteria whether each fragment is well distinguished from the structure or not.

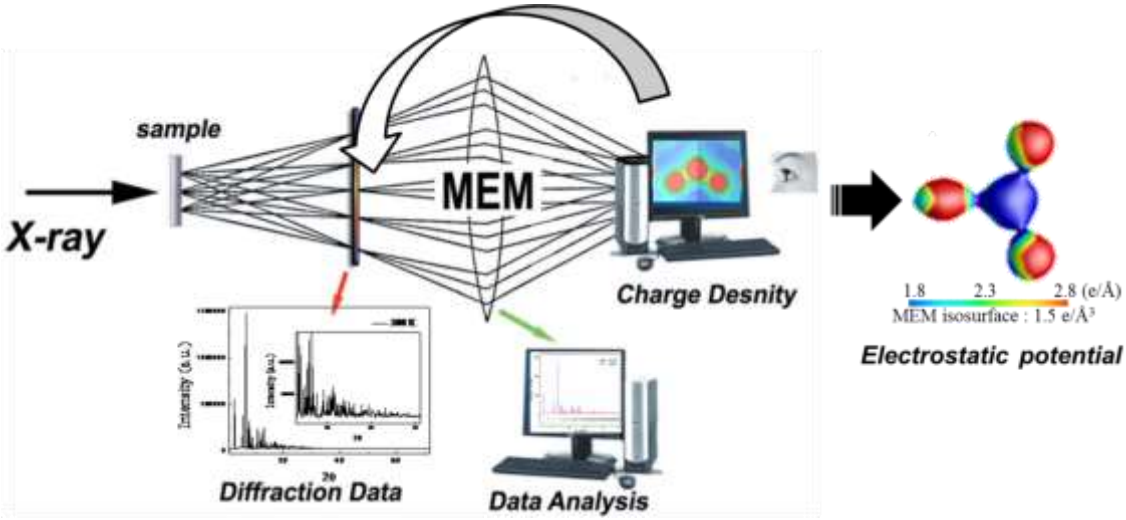

Figure 2-6. Process of the MaxEnt/EP analysis by using Synchrotron X-ray powder diffraction.

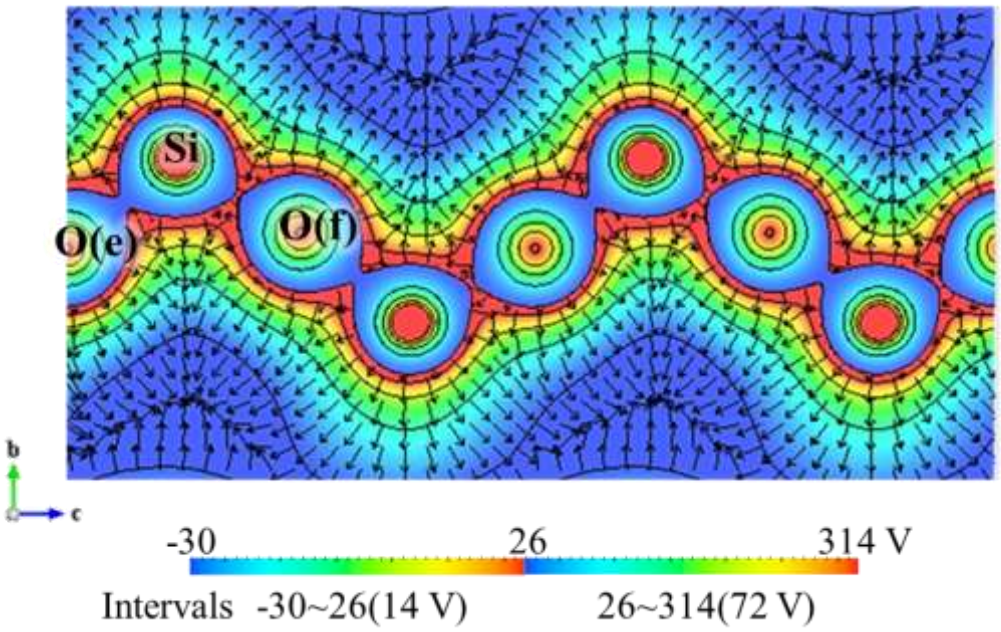

Figure 2-7. Two-dimensional electrostatic potential map of the SiO_3 layer in Bi_2SiO_5. Electric fields are indicated as black arrows.

2.3 Ferroelectric polarization

2.3.1 Electric dipole moment and polarization

The electric dipole moment is a vector quantity related to the separation of positive and negative charges.[42,43] If the separation between positive and negative charges appears without the application of the external perturbation, such as electric field, it is a permanent electric dipole moment. Typical example of the permanent dipole is water molecule having net direction of charged atoms, one O^{2-} and two H^{+}. In the simple case for two point charges of equal magnitude and opposite sign, the electric dipole moment $\vec{p}$ is written as:

$$\vec{p} = q \cdot \vec{d} \tag{2.28}$$

where q is the charge and $\vec{d}$ is the displacement vector from the negative charge to the positive charge. In the real molecule, electrons have a continuous distribution confined to a specific volume. The general expression for the dipole moment can be expressed as:[44]

$$\vec{p}(\mathrm{r}) = \int_V \rho(\vec{r}_0 - \vec{r}) dV \tag{2.29}$$

where $\vec{r}$ is the observation point and dV is an elementary volume for charge density. The dipole moment in the system which has neutral charge is independent to the choice of observation point. For a non-neutral system, however, the dipole moment is dependent to the choice of observation point. In this case, the center of mass in the system is treated as the observation point for calculation of the dipole moment.

Ferroelectric materials have a net permanent dipole moment calculated by the vector

summing of the every dipole moments in the unit cell. Existence of the net permanent dipole moment can be assumed using symmetry relation of the point groups. If the structure has a center of symmetry, a dipole moment caused by the separation of negative and positive charges is offset by other dipole moment which has same magnitude and opposite direction. Thus, non-centrosymmetry is required to have spontaneous polarization.

2.3.2 Polarization estimation based on the charge density distribution

The electric polarization $\vec{P}$ is defined as the net electric dipole moment per unit volume *V*. General expression of electric dipole moment can be expressed from the charge density as below:

$$\vec{P} = \frac{1}{V}\int_V \vec{r}\rho(\vec{r})d\vec{r} \tag{2.30}$$

The Polarization based on the nucleus charge and the electron charge density in the unit cell can be calculated *via*:[45~47]

$$\vec{P} = \frac{e}{V}[\sum_i z_i(R_i - r_0)\hat{R} - \int_V (r_i - r_0)\rho_i(r_i)dr\hat{r}] \tag{2.31}$$

where *V* and *e* are the volume of the dipole unit and elementary charge (1.602×10^{-19} C). z_i and R_i are atom number and position of *i*th atom. $\rho(r_i)$ is the electron density located at *i*th pixel. r_i and r_o are the position of *i*th pixel and the center of mass. Many text books define the polarization as the dipole moment of its unit-cell volume *V*. However, this approach has problem, because the obtained polarization using equation (2.30) is strongly dependent to the shape and choice of the unit cell. This problem is illustrated in Figure 2-8 with classical

point charges denoted by + and – sings. The colored regions are arbitrary determined unit cell. Every unit cell has same volume and net charge, however, the dipole moment of the unit cell is quite different depending of the unit cell choice. In addition, because electron density is continuously distributed in the unit cell, determination of the boundary for electron density of each atom is also difficult problem. Thus, definite boundary is required to obtain the polarization which is independent to unit cell choice. In order to solve this problem, we employed electrostatic potential analysis in this research. As it was explained, local structure which is enclosed by the minimum of electrostatic potential can be determined. We expect this method can show the polarization value which is independent to the unit cell choice.

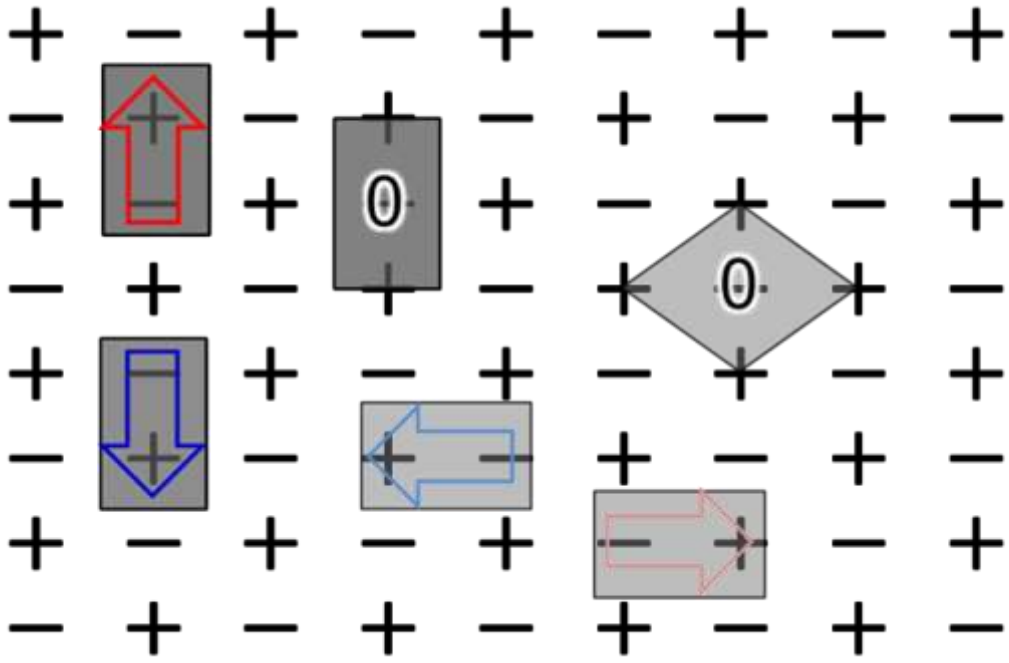

Figure 2-8. Classical point charges with various unit cell choice.[13]

2.4 The MaxEnt/fragment EP method for estimation of local/total polarization

2.4.1 Process of the MaxEnt/fragment EP method

Flowchart of the process of local/total polarization estimation is shown in Figure 2-9. The MaxEnt/fragment EP method is based on the conventional MEM and electrostatic potential analysis. At first, using high quality data measured at Synchrotron Radiation facility, the structure analysis was performed by MEM/Rietveld refinement. The structure parameter and atom position were determined from Rietveld refinement. The MEM charge density was obtained by an ENIGMA program.[48] Obtained electron density was assigned to a pixel which constructs a whole unit cell divided by 128 × 128 × 128 pixel grids. The volume of one pixel was about 0.03 × 0.03 × 0.03 $Å^3$. For Bi_2SiO_5, unit cell was divided into 256 × 128 × 128 pixels, and the volume of one pixel was about 0.06 × 0.04 × 0.04 $Å^3$. Total electron in the unit cell for $PbTiO_3$, $BaTiO_3$ and Bi_2SiO_5 was 128 *e*, 102 *e* and 880 *e*, respectively. They corresponded to the number of total nucleus in the unit cell. Using the result of MEM electron charge density and atom position from Rietveld refinement, electrostatic potential was calculated.

In the research, we introduce new concept, fragment. Fragment is determined by tracing the local minimum of electrostatic potential; it has weak electrostatic interaction between fragments. In order to estimate the polarization of fragment, electron density is quantized. Using position of nucleus charge and electron density inside the fragment unit, local polarization of fragment can be estimated. Details of determination of fragment and

calculation method are explained in chapter 2.4.2 and 2.4.3.

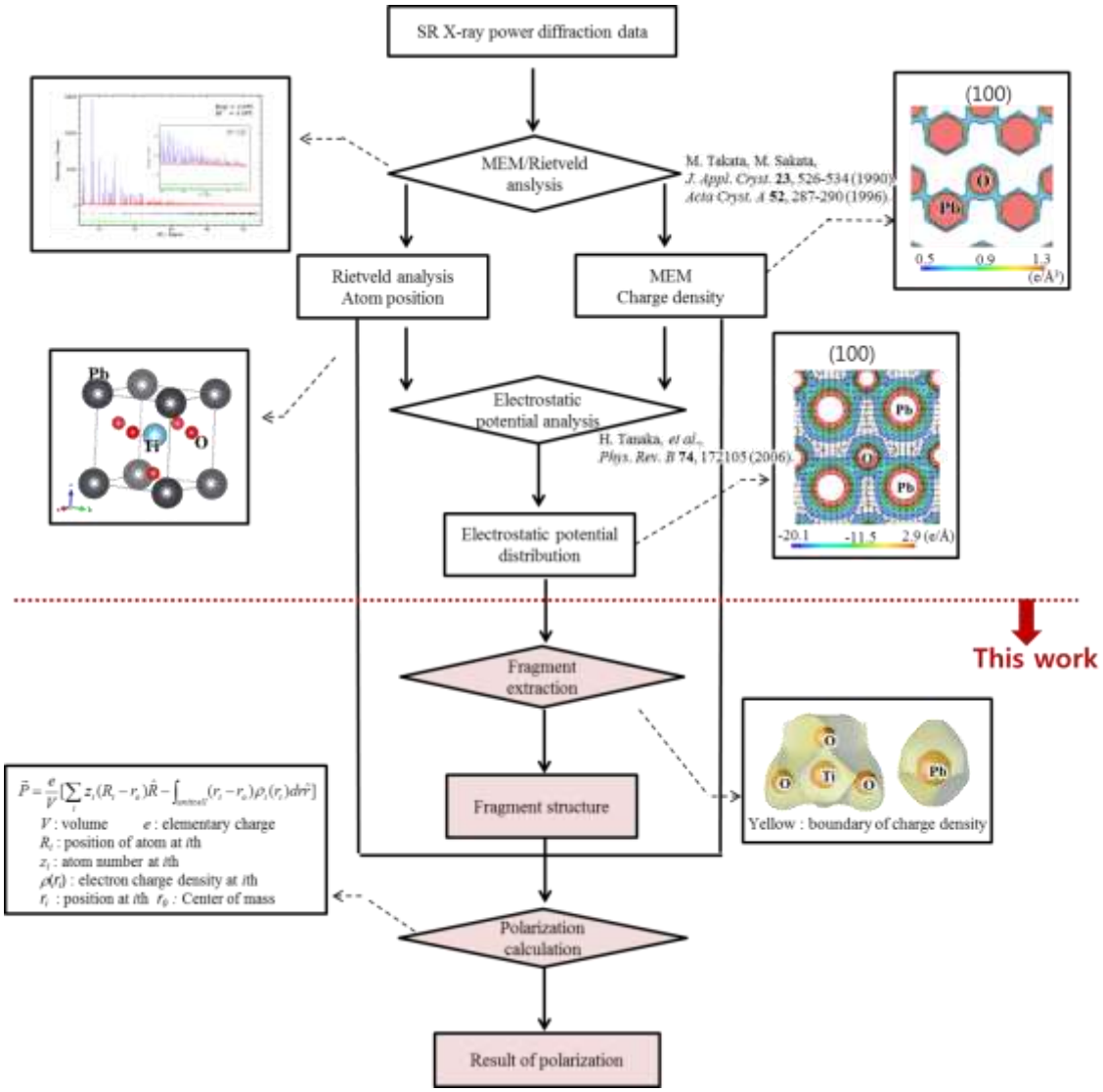

Figure 2-9. Flowchart for the determination of the local and the total polarization value by the MaxEnt/fragment EP method.

2.4.2 Fragment determination by boundary of electrostatic potential

The determination method of fragment is shown in Figure 2-10 and Figure 2-11, which are the two-dimensional electrostatic potential of $PbTiO_3$. Figure 2-10 shows the electrical interaction between Ti-O and Pb-O bonds on the (200) plane. It is colored from -18.0 V to 3.6 V with the 3.0 V intervals of equipotential line. Red and Blue indicated the high potential (3.6 V) and the low potential (-18.0 V) region, respectively. Black arrows in the Figure 2-10 are electric field calculated by negative gradient of the electrostatic potential at each position. The electric field has advantage to easily see the change of electrostatic potential, especially the change in the low electrostatic potential region.

At a first stage to determine fragment, the minimum values of bonding electrostatic potential in every bond are compared. For example, O1 in Figure 2-10 has two neighboring cations such as Pb and Ti; the minimum value of Ti-O1 and Pb-O1 is 13.5(4) V and -14.8(1) V, respectively. The same processes are also applied to other bonds as shown in Figure 2-11. It is compared that the value of minimum electrostatic potential between Ti-O2 and Pb-O2; the minimum value of Ti-O2 and Pb-O2 is -4.3(1) V and -17.6(1) V, respectively. An assembly of the all paired bonds is designated as fragment. For polarization estimation in the fragment, the MEM electron charge density is quantized. Value of MEM electron density is located at each pixel which constitutes the unit cell. MEM electron density has continuous distribution in the structure.

Fragment of TiO_3 in $PbTiO_3$ is shown in Figure 2-12. Yellow color means the determined boundary by tracing the local minimum of electrostatic potential around the

fragment.

In order to estimate error of total electron in the fragment, we count the electron density inside finite pixel size. MEM and EP are a well-established method with finite dataset; errors for analyzed data cannot be extracted. On the other hands, the result of MEM and EP include errors due to the finite pixel size, and the error bars originating from this ambiguity have been shown for all data. Figure 2-13 shows the schematic view of electron charge density at TiO_3 fragment. Black line is the determined boundary for the fragment. Red and Blue indicate the position of pixel which is obtained by increasing and decreasing 1 pixel from the boundary, respectively. Difference of total electron density in red and blue region Figure 2-13 is considered as error bar. Number of electron charge in TiO_3 fragment is 46.01(1) e, and it is coincident to the number of nucleus charge in the error range.

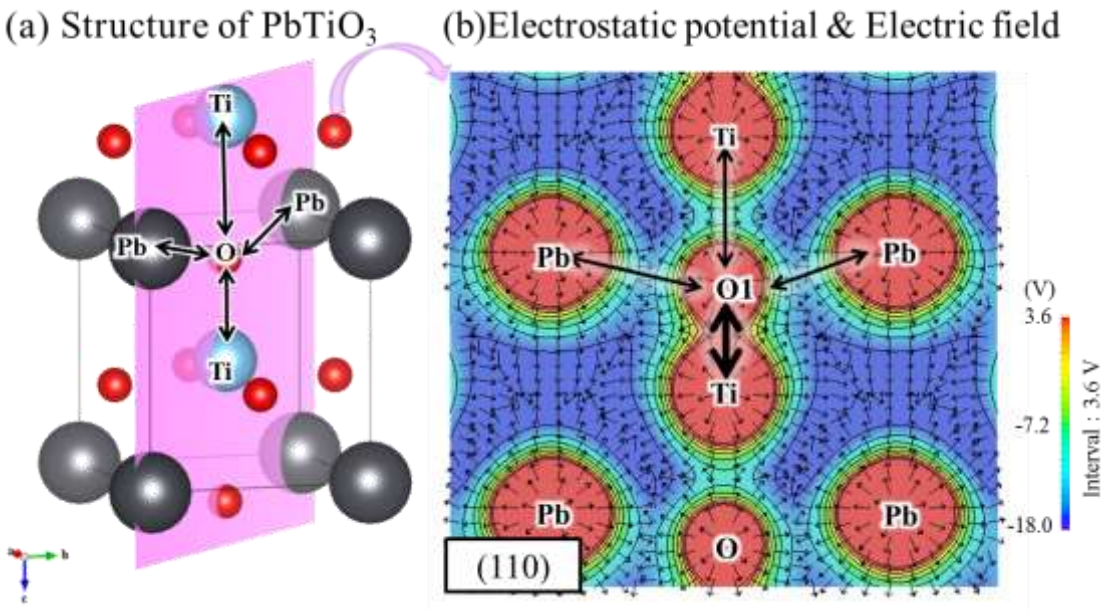

Figure 2-10. (a) Structure of $PbTiO_3$ and (b) two-dimensional electrostatic potential of $PbTiO_3$ on the (110) plane for Pb-O1 and Ti-O1 bonds.

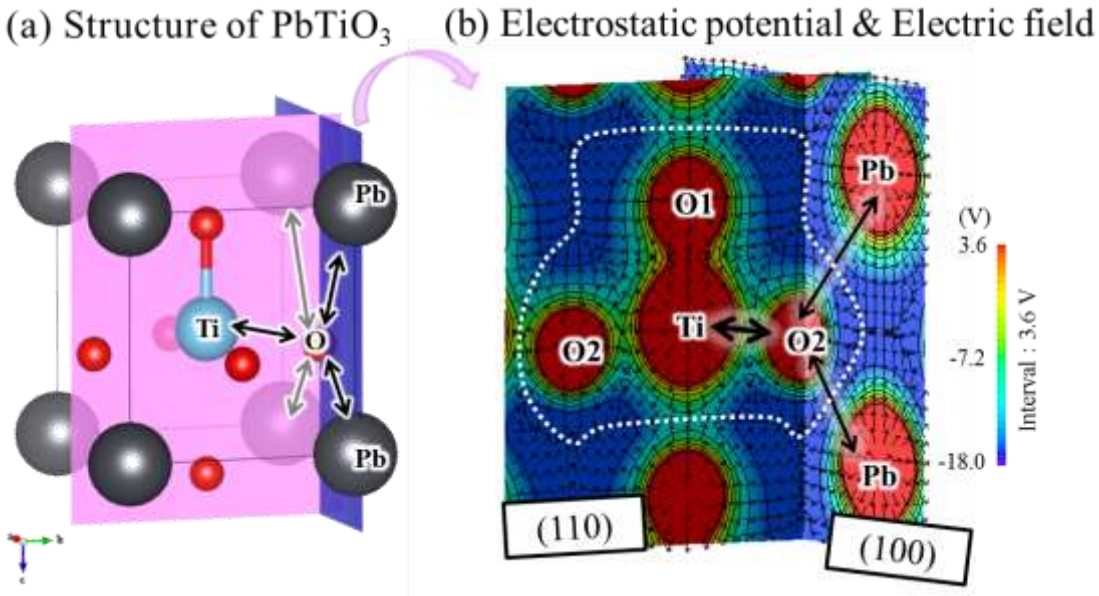

Figure 2-11. (a) Structure of $PbTiO_3$ and (b) two-dimensional electrostatic potential of $PbTiO_3$ on the (110) and the (100) planes for Pb-O2 and Ti-O2 bonds.

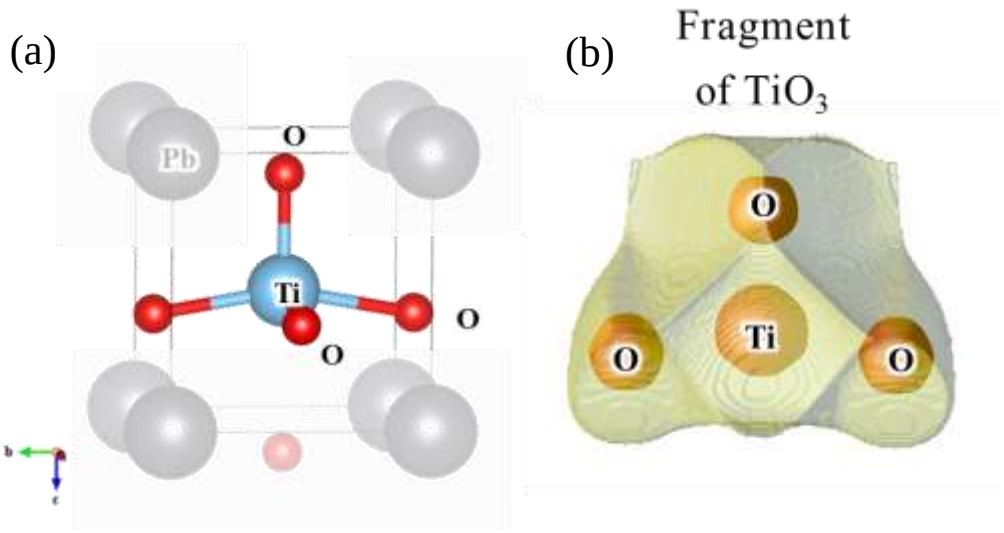

Figure 2-12. (a) Structure model of $PbTiO_3$ and (b) determined fragment of TiO_3 in $PbTiO_3$

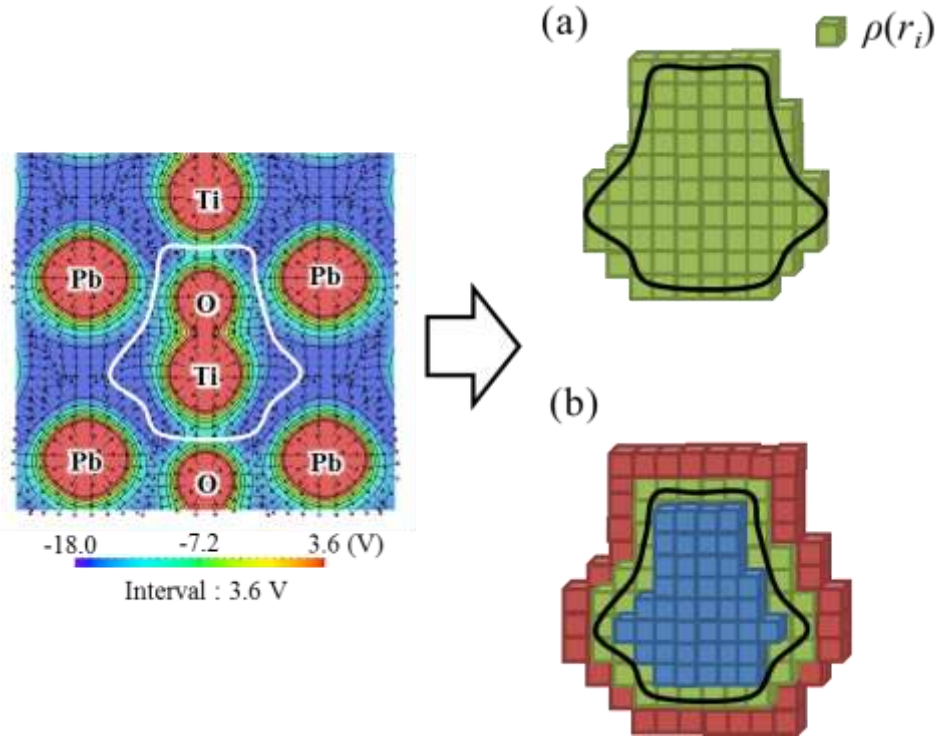

Figure 2-13. (a) Schematic figure of pixels determined by fragment with electron density (green color) and (b) the method of error bar estimation with finite pixel size.

2.4.3 Polarization calculation by the MaxEnt/fragment EP method

The electric polarization $\vec{P}$ is defined as the net electric dipole moment per unit volume V. The equation of electric dipole moment is expressed from the charge density as equation (2.31). Equation (2.31) can be rewritten as:

$$\vec{P} = \frac{e}{V}\left[\sum_i A_i\{(X_i - x_o)\hat{x} + (Y_i - y_o)\hat{y} + (Z_i - z_o)\hat{z}\}\right.$$
$$\left. -\{\int (x_i - x_o)\rho_i(x_i)dx_i\hat{x} + \int (y_i - y_o)\rho_i(y_i)dy_i\hat{y} + \int (z_i - z_o)\rho_i(z_i)dz_i\hat{z}\}\right] \qquad (2.32)$$

where e and V are the elementary charge (1.602×10^{-19} C) and the unit cell volume, respectively. A_i and (X_i, Y_i, Z_i) are the atom number and position of ith atom. (x_o, y_o, z_o) is the position of the center of mass in the fragment unit. $\rho_i(x_i, y_i, z_i)$ is the electron density located at ith pixel. (x_i, y_i, z_i) are the position of ith pixel for electron charge contribution. $(\hat{x}, \hat{y}, \hat{z})$ are the unit vectors, and integration is carried out over the fragment unit. In the calculation process for polarization, nucleus charge from Rietveld refinement and electron charge inside fragment were applied to the equation (2.32). Error bar of polarization value is estimated by considering the error bar of the number of electrons in fragment.

2.4.4 Original program using C++ language for computational process

All calculation was carried out using original program with C++ language, because electron density and electrostatic potential should be quantized in too many numbers of

pixels in unit cell: for Perovskite materials and Bi_2SiO_5, unit cell was divided by 128 × 128 × 128 pixels and 256 × 128 × 128 pixels, respectively. Whole computational process is subdivided as into 3 steps, expanding the quantized electron density and electrostatic potential by the symmetry operation, finding the position of the minimum electrostatic potential for fragment and calculation of polarization. Original MEM and electrostatic potential results have the data in asymmetric unit, which is a smallest closed part of space. By application of symmetry operation at the space group, the whole of space can be filled. For the following calculation, the electron density in the materials was expanded to the lowest symmetry structure by using symmetry operation, in which asymmetric unit has same pixel size with the unit cell.

The fragment was determined based on the minimum value of electrostatic potential. We tried to find the position of the local minimum of electrostatic potential from the position of atom. For example, Pb in $PbTiO_3$ is located at (0, 0, 0) pixel. One-dimensional electrostatic potential value from (0, 0, 0) to (127, 0, 0) is plotted, and position of the local minimum of electrostatic potential is obtained. Then, same process is carried out from (0, 1, 0) to (127, 1, 0). This is continued until the full boundary for Pb atom is traced. As a result, it is possible to determine the all fragment in the structure. Because we knew the position of pixel at each fragment, the electron density is directly assigned from the MEM data. In order to know whether the fragment is well separated from the unit cell, total number of electron and nucleus charge was compared whenever each fragment was determined. Calculation of polarization is iteratively carried out until every electron density in fragment is applied to equation (2.32). During the calculation process, each axis is treated independently for simple calculation.

Chapter 3

Experimental measurement

In order to analyze the electron density level structure, high quality diffraction data with high counting statics and high resolution are required. In this research, X-ray powder diffraction experiment was carried out at powder diffraction beamline, BL02B2, in SPring-8 (Figure 3-1). The advantage of the Synchrotron radiation X-ray powder experiment is as follows. It eliminated the need for considering extinction effect and problems of ferroelectric multidomains. In addition, high-energy of Synchrotron X-ray minimized the absorption effect for samples via appropriate selection of the measurement wavelength. A large Debye-Scherrer camera equipped with an imaging plate was used;[49,50] the measurement was carried out in transmission geometry to ignore the absorption and extinction effect as well as to avoid the preferred orientation by rotating capillary during measurement.[49] For the in-situ temperature controlled X-ray diffraction, we used N_2 gas flow system: the temperatures were controlled from 300 K to 900 K.

In the chapter 3, to obtain X-ray diffraction data of high quality which is sufficient to analyze the charge density level structure, the details of the sample preparation and the selection method of capillary size and wavelength are described.

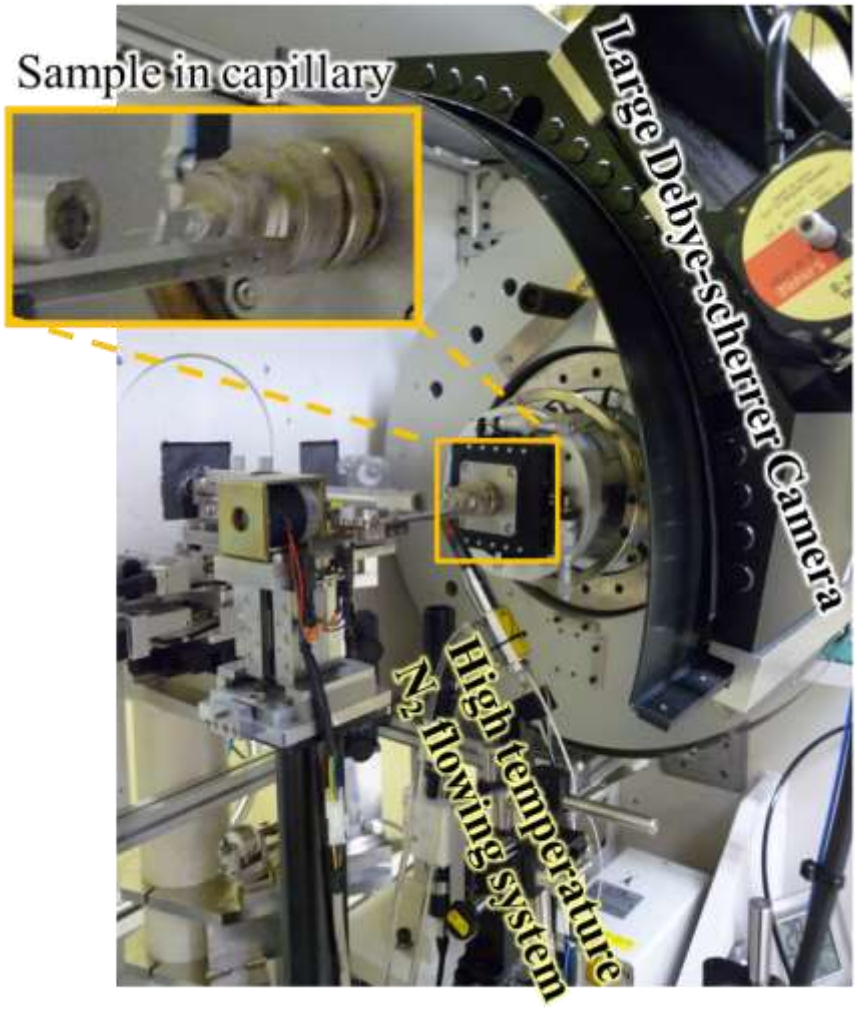

Figure 3-1. Debye-Scherrer camera at BL02B2 in SPring-8.

3.1 Sample preparation

In the research, we used the three samples: the samples of $PbTiO_3$, $BaTiO_3$ and Bi_2SiO_5. Perovskite materials, $PbTiO_3$ and $BaTiO_3$, were purchased from Sigma Aldrich ($PbTiO_3$: CAS 12060-00-3, $BaTiO_3$: CAS 12047-27-7). Because their ferroelectric property had been well known, they were used for the verification test of the MaxEnt/fragment EP method by comparing the obtained results. As application of the MaxEnt/fragment EP method, ferroelectric polarization of Bi_2SiO_5 was studied, which is one of the lead-free ferroelectric materials. Powder Bi_2SiO_5 sample was synthesized by Taniguchi *et al* and details of sample preparation were explained in the previous report.[51] All samples were carefully prepared to get the high quality diffraction data with homogeneity of intensity distribution on Debye-Scherrer rings: the accuracy of the powder diffraction data is influenced by the uniformity of grain size in the powder sample. The powder sample is composed of many crystallites of varying size and orientation; the diffraction pattern of the powder sample having a random orientation distribution is observed with Debye-Scherrer rings. When the distribution of crystal size is not uniform, homogeneous distribution of Debye-Scherrer ring is not observed: some spots from large size of crystal are obtained on the Debye-Scherrer rings. To fabricate a uniform crystal size for a homogeneous granularity, there is a method to grind the powder sample. However, a smaller crystal size below about 0.1 micrometers by excessive grinding gives influence on the peak broadening as explained by Scherrer equation; line broadening makes it difficult to separate partially overlapped peaks. The appropriate crystal size of the powder sample for precise structure analysis is known as sub micrometer range.

In the research, we have measured X-ray diffraction using the prepared samples after grinding for several minutes; the sample with diffraction data having homogeneous intensity distribution on Debye-Scherrer rings was selected for the main measurement to analyze the electron density level structure. Figure 3-2 (a) and (b) show X-ray diffraction pattern of Bi_2SiO_5 measured at 300 K. The samples for (a) and (b) diffraction pattern were prepared by grinding for 10 minutes and 30 minutes, respectively. At the first stage, test measurement to find the most suitable condition for sample preparation was carried out. The X-ray exposure time was 5 minutes. Shape of Debye-Scherrer rings on the IP and FWHM of peaks at high angle region were checked after the each test measurement was finished. In the data of the grinded Bi_2SiO_5 sample for 10 minutes, the spots on the Debye-Scherrer rings were observed. To reduce the spots, the powder sample was re-grinded, and X-ray diffraction measurement was also carried out again. This process was repeated to obtain homogeneous Debye-Scherrer rings: total grinding time was 30 minutes and we prepared the high quality sample with homogeneous diffraction pattern excluding spot and peak broadening (Figure 3-2(b)).

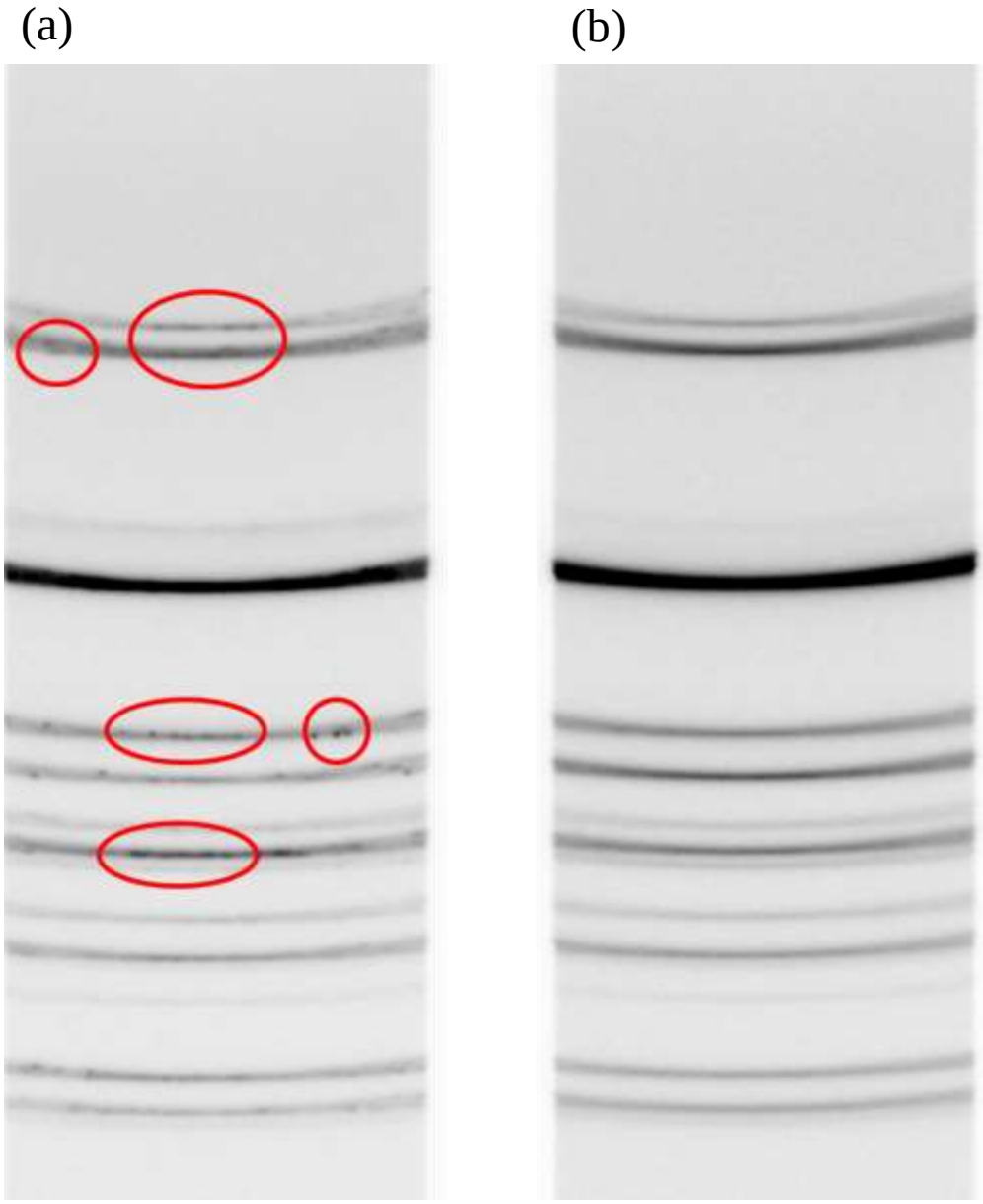

Figure 3-2. Debye-Scherrer rings of Bi_2SiO_5 at 300 K. The sample was prepared by grinding for (a) 10 minutes and for (b) 30 minutes.

3.2 Selection of capillary size and wavelength

The prepared powder samples were sealed in a glass capillary. The glass capillary is a useful container for powder samples when measuring the X-ray diffraction data using transmittance geometry. In order to obtain high statistics and high resolution data, we should select an appropriate capillary size and capillary material for a wavelength with minimal absorption effects.

Some capillaries have higher melting points than others and can be utilized in elevated temperature experiments, while other capillaries might contribute less to the background signal. Sample thickness, which is a result of capillary size, affects Imaging-plate saturation time as well as resolution. The saturation time determines optimal exposure time. In this experiment, Lindemann glass capillary was chosen to obtain data with low background effects, and a capillary size of 0.1mmϕ was selected to obtain high angle resolution data and to avoid absorption effect caused by heavy atoms such like Pb and Bi in the material.

The appropriate wavelength with minimal absorption effect was chosen by calculation of relative transmission factor. Depending on what sample is inside the capillary, it will absorb a certain amount of the X-ray radiation. This absorption depends on the angle between the reflected beam and the incident x-ray. As such, if this absorption effect is high, the data will have to be corrected to account for it. The relative transmittance factor, described in the literature, is a way of comparing the absorption for different 2θ values.[52,53] In the case of powder x-ray diffraction, this crystal radius corresponds to the diameter of the

capillary. One can therefore calculate the relative transmittance between 0 degrees in 2θ and other angles. If this relative transmittance has the value less than 1% for the sample in question, the absorption effect is negligible, and no absorption correction is needed for the diffraction data. The equation of relative transmittance factor is the following: The linear absorption coefficient is a quantity to characterize how the X-ray easily can penetrate the material and is written as below equation:

$$I = I_0 \exp(-\mu x) \tag{3.1}$$

where, μ is the linear absorption coefficient. I_0 is the intensity of the incident X-ray and I is the measured intensity after the incident X-ray transmitted through the material with thickness x. As the value of linear absorption coefficient is large, intensity of transmitted beam is quickly weakened. Linear absorption coefficient can be calculated by the equation (3.2):

$$\mu = z \sum_i (MA)_i / (V \cdot 10^{-24}) \tag{3.2}$$

where, z is the chemical unit, i is the number of atoms in one unit cell, MA is the atomic absorption coefficient, V is the unit cell volume in Angstrom unit, and the summation is taken over all constituent elements. Value of MA is dependent to wavelength of the incident X-ray, and it is taken from the database. Using linear absorption coefficient, Rouse *et al*. suggested the relative transmission factor (A_{hkl}) to measure the X-ray diffraction without considering the absorption correction.[53] The following equation (3-3) is for the relative transmission factor:

$$A_{hkl} = \exp\{-(a_1 + b_1 sin^2\theta)\mu R - (a_2 + b_2 sin^2\theta)(\mu R)^2\} \tag{3.3}$$

where R is the radius of the sample, θ is the Bragg angle and μ is the linear absorption

coefficient. For the material of cylinder shape, the coefficients are a_1=1.7133, a_2=-0.0927, b_1=-0.0368 and b_2=-0.3750.

In this research, we calculated the relative transmission factor from 0° and 80° of 2θ angle with 0.1mmϕ capillary size. The results shown in Figure 3-3: it is the result of relative transmission factors of $BaTiO_3$/$PbTiO_3$ and Bi_2SiO_5 depending on the wavelength of incident X-ray beam at 80 ° of 2θ angle. For the Bi_2SiO_5, when using below 0.5 Å radiation is well below the limit of 1%, so absorption effects do not have to be corrected after data acquisition. In the research, we selected the wavelength of 0.35 Å for high accuracy data analysis with much more information of structure; the corrected wavelength was 0.35206(1) Å using the diffraction data of standard sample CeO_2(NIST 674a, lattice parameter=5.4111(1) Å). For the Perovskite materials, the wavelength of 0.35 Å is not suitable because $BaTiO_3$ has the absorption edge near 0.35 Å. For this reason, 0.4 Å was selected as the measurement wavelength; it was corrected with the wavelength of 0.40085(1) Å. Measurement time of the data for the electron density level structure analysis was determined based on the saturation time for IP, which is related to the maximum capacity of IP for diffracted data. For example, saturation time for each sample was found by test measurement for 5 minutes. Then, measurement time was determined by 0.9 times the saturation time. For $PbTiO_3$, $BaTiO_3$ and Bi_2SiO_5, data were corrected during 51, 13 and 45 minutes, respectively. Two dimensional diffraction patterns on the IP were obtained as shown in Figure 3-4. Figure 3-4 is two dimensional data of the Bi_2SiO_5 from room temperature to 773 K. Different brightness is related to the different measurement time. All of two dimensional diffraction patterns were transformed to the one dimensional diffraction data.

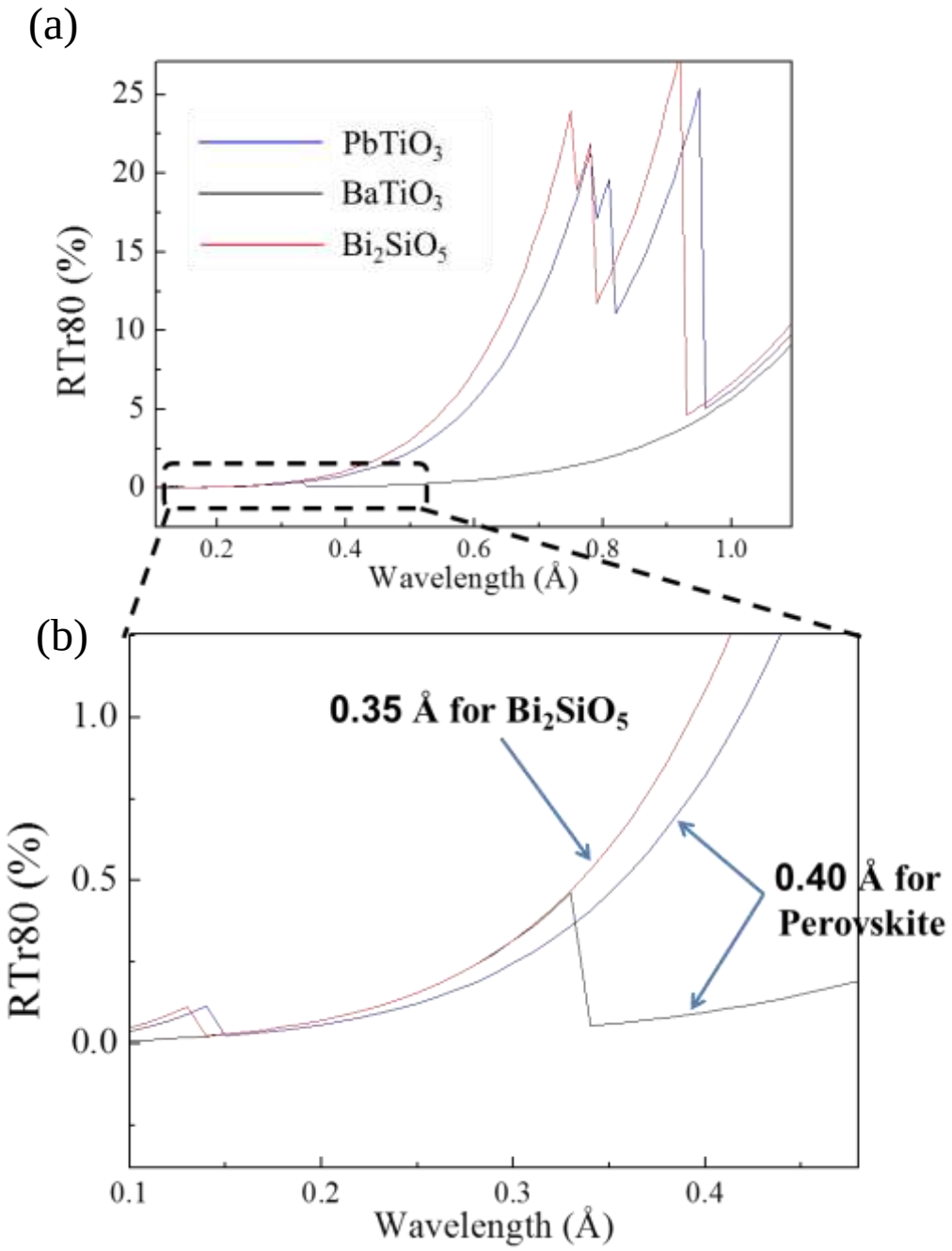

Figure 3-3. (a) Relative transmission factor between 2θ = 0 ° and 80 ° of $PbTiO_3$, $BaTiO_3$ and Bi_2SiO_5 dependent to wavelength. (b) Magnified region near wavelength of 0.3 Å . Capillary size of 0.1 mm in diameter was used.

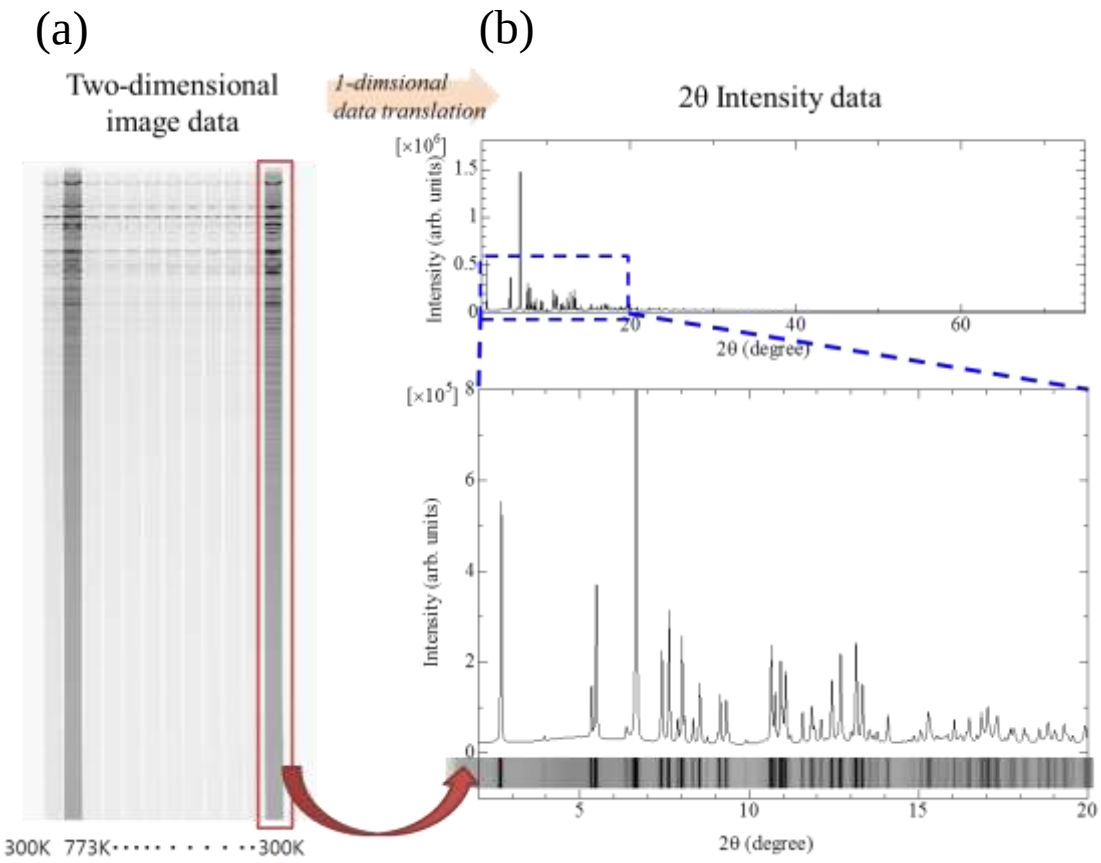

Figure 3-4. Two-dimensional diffraction patterns on (a) the IP and conversion to (b) 2θ intensity data.

Chapter 4

Validity test of the MaxEnt/fragment EP method using Perovskite materials ($PbTiO_3$ & $BaTiO_3$)

We applied the MaxEnt/fragment EP method to well-known Perovskite materials, $PbTiO_3$ and $BaTiO_3$, in order to verify the validity of the method. For the estimation of polarization, conventional MEM/Rietveld and electrostatic potential analysis were carried out. The result of MEM analysis showed an apparent difference of bonding characteristic in both materials; covalency between cation (Pb/Ba, Ti) and anion (O) in $PbTiO_3$ is more enhanced than that in $BaTiO_3$. Electrostatic potential imaging revealed that $PbTiO_3$ has strong ionic polarization of TiO and electronic polarization of Pb ion. Using the MEM electron density inside the each atom, the neighboring cation-anion pair and the fragment, we estimated the local/total polarization of $PbTiO_3$ and $BaTiO_3$. Based on the results, we discuss the validity of this MaxEnt/fragment EP method.

4.1 Crystal structure and ferroelectricity of $PbTiO_3$ and $BaTiO_3$

$PbTiO_3$ and $BaTiO_3$ have a Perovskite structure. Perovskite structure is described as a formula ABO_3, in which B is a cation of a small size surrounded by six O anions in an octahedral configuration, and A is a cation with a large size forming the octahedron within the structure.[54~56] In $PbTiO_3$ and $BaTiO_3$, Pb and Ba atoms are located at A site, and Ti is positioned at B site in the Perovskite structure.[54~56] It has been known that the ferroelectricity in Perovskite oxide materials is involved with structural phase transition from high symmetry to low symmetry with cooling.

For the validity test of the MaxEnt/fragment EP method, $PbTiO_3$ and $BaTiO_3$ were investigated because their ferroelectric property has been well know. Furthermore, they have a large difference of ferroelectricity, although they have same crystallographic point group at room temperature and high temperature above T_c. Structure of $PbTiO_3$ and $BaTiO_3$ is shown in Figure 4-1. As temperature decreases, $PbTiO_3$ and $BaTiO_3$ undergo the structural phase transition from high temperature cubic (*Pm*3*m*, #221) to low temperature tetragonal phase (*P*4*mm*, #99). Curie temperature (T_c) for $PbTiO_3$ and $BaTiO_3$ is about 673 K and 393 K, respectively.[57,58] Displacement of anion and cation by structural phase transition causes a spontaneous polarization of the material; it was proposed that the hybridization between Ti-3d state and O-2p state in $PbTiO_3$ and $BaTiO_3$, which reduced a short range Coulomb repulsion between Ti and O ion;[59~62] polarization value by *PE*-hysteresis measurement for $PbTiO_3$ and $BaTiO_3$ has been reported with the value of 52~75 $\mu C/cm^2$ and 15~25 $\mu C/cm^2$, respectively.[63~74]

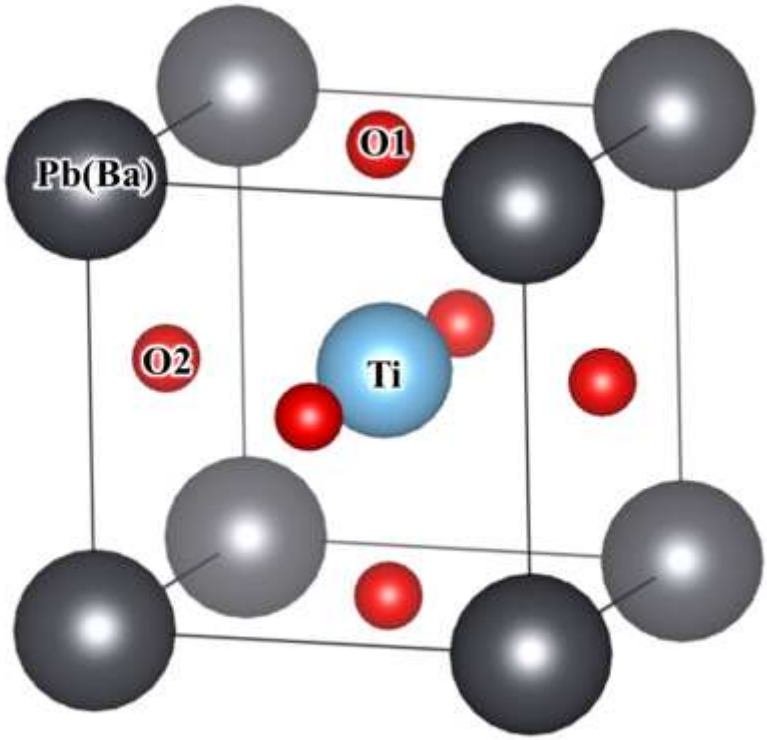

Figure 4-1. Crystal structure of $PbTiO_3$ and $BaTiO_3$. O1 and O2 are placed with same site symmetry at high temperature cubic phase.

Table 4-1. Reported polarization value of $PbTiO_3$ and $BaTiO_3$

$\mu C/cm^2$

	$PbTiO_3$	$BaTiO_3$
PE measurement	52~75 [63,66]	15~25 [68,70,73]
First-principle calculation	70~87 [64,65,67]	23~29 [69,71,72,74]

We estimated the polarization value in $PbTiO_3$ and $BaTiO_3$ by the MaxEnt/fragment EP method, and the results were compared to the reported result for the validity test of the method. As a first step, the conventional MaxEnt/EP analysis was carried out. The Synchrotron X-ray powder diffraction data were analyzed by Rietveld refinement to obtain the lattice parameter, the atom position and the structure factors. The lattice parameter and the atom position were used for the volume and position of positive charge during the calculation process for polarization by the MaxEnt/fragment EP method. The structure factors were required for the electron density by MEM, which is related to the polarization caused by the negative charge.

$PbTiO_3$ showed the structural phase transition from cubic to tetragonal phase. Contrary to the $PbTiO_3$ structure, $BaTiO_3$ has core-shell structure:[75~78] the core structure is tetragonal and shell structure is cubic phase at 300 K. The ferroelectric core structure is covered with the paraelectric shell structure.[78] For the estimation of polarization at ferroelectric phase, the separation of tetragonal and cubic phase is required for $BaTiO_3$ at 300 K. In our data, $BaTiO_3$ has 1 phase of tetragonal and 2 phases of cubic at room temperature; high temperature phase has 3 cubic phases. In this study, ferroelectric phase at both materials is used to compare the structural difference and to estimate the polarization. The results are plotted in Figure 4-2 and Figure 4-3, respectively. The red dot and blue line are the observe data and calculated result, respectively. Sky blue line shows background which was analyzed by Rietveld refinement. Green line is a difference between the calculated and observed data. Ranges in *d* spacing for $PbTiO_3$ ($BaTiO_3$) at ferroelectric and paraelectric phase are 0.37 Å (0.34 Å) and 0.56 Å (0.56 Å), respectively. Calculated integrated intensity for $PbTiO_3$ and $BaTiO_3$ is well matched to the measured intensity even

in the high angle region as shown in Figure 4-2 and Figure 4-3.

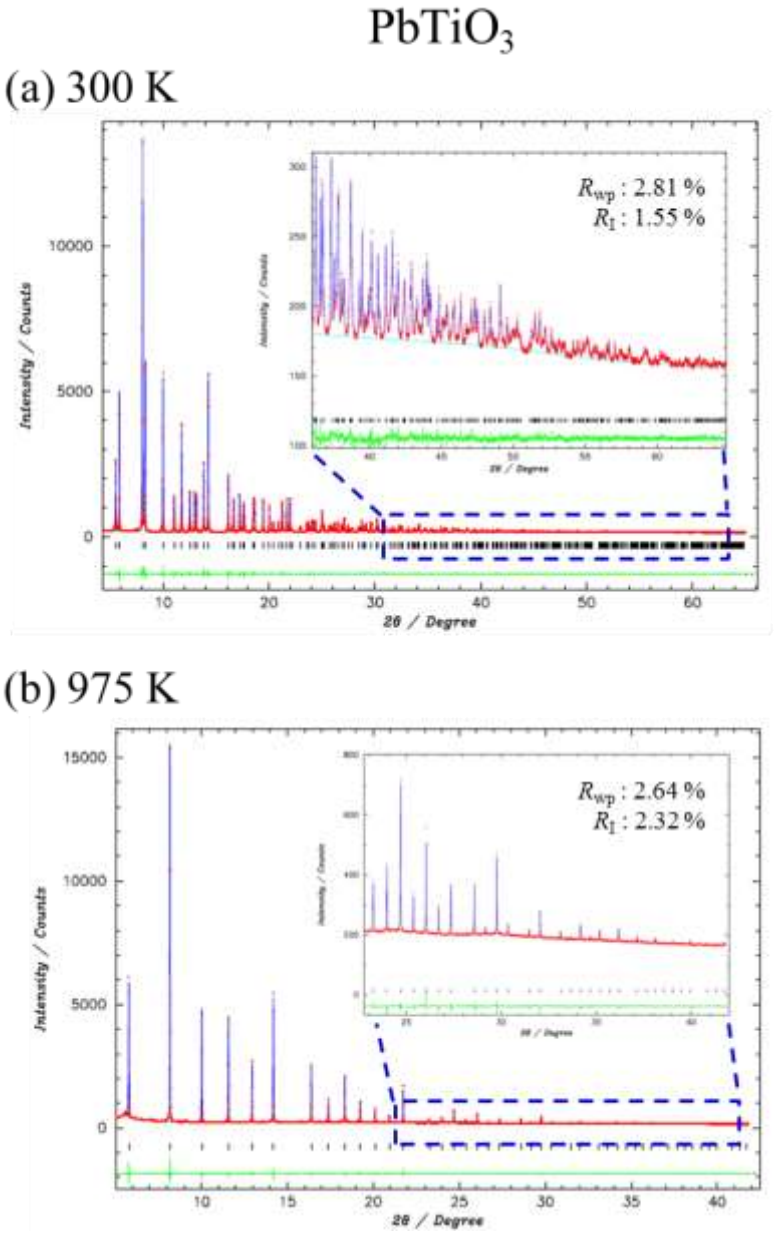

Figure 4-2. Results of Rietveld refinement for $PbTiO_3$ (a) ferroelectric phase at 300 K and (b) paraelectric phase at 975 K.

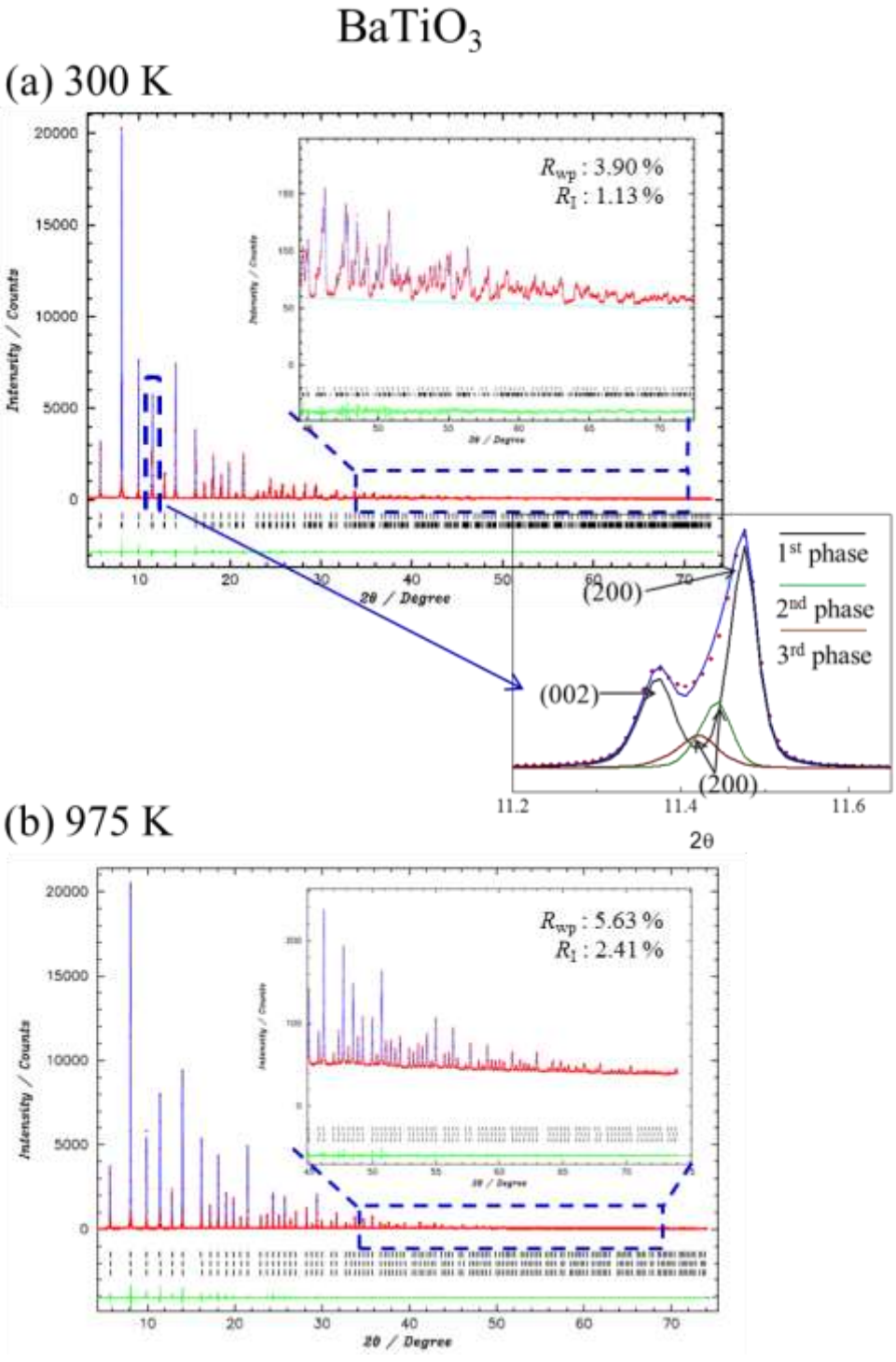

Figure 4-3. Results of Rietveld refinement for $BaTiO_3$ (a) ferroelectric phase at 300 K and (b) paraelectric phase at 510 K.

The structural parameters of $PbTiO_3$ and $BaTiO_3$ are listed in Table 4-2 and Table 4-3, respectively. Reliable factors for $PbTiO_3$ at 300 K (975 K), R_{wp} and R_I, are 2.81 % (2.64 %) and 1.55 % (2.32 %), respectively. For $BaTiO_3$, R_{wp} and R_I are 3.90 % (5.63 %) and 1.13 % (2.41 %) at 300 K (510 K), respectively. Every reliable factor is under 5 %, showing that our refinement was successfully carried out. As it is shown in Figure 4-3, ferroelectric (black line) and paraelectric (green line) phase in $BaTiO_3$ at 300 K was clearly distinguished. Here, we compared ferroelectric phase between $PbTiO_3$ and $BaTiO_3$. At ferroelectric phase of $PbTiO_3$, the lattice parameter of c-axis increased by 4 %, whereas the lattice of a-axis shrank by 2 %; it changed tetragonality which is a ratio of c and a lattice parameter, c/a,[79] by 1.06. On the other hands, in $BaTiO_3$, the change of lattice parameters was below 1 %; the tetragonality was 1.01 %. In addition to the significant changes of lattice parameter, the bond length of Ti-O1 and Pb-O2 shrank with over 10 % in $PbTiO_3$ structure; in $BaTiO_3$, Ti-O1 and Ba-O2 bond shrank by 7 % and 2 %, respectively. The large lattice elongation and bond contraction along c-axis is connected to the large ferroelectricity; it was indicated in the previous report written by Kuroiwa *et al*.[80] Functional structure of $PbTiO_3$ and $BaTiO_3$, such as the electron density and electrostatic potential was obtained for the calculation of polarization. They were compared to find the difference between $PbTiO_3$ and $BaTiO_3$ in the electron density level structure.

Table 4-2. Determined (a) space group, lattice parameter, (b) atom position and (c) bond-length of cation and anion in $PbTiO_3$ by Rietveld refinement at 300 K and 975 K.

(a) $PbTiO_3$		300 K Ferroelectric	975 K Paraelectric
Space group		*P*4*mm*, #99 Tetragonal	*Pm*3*m*, #221 Cubic
Lattice parameters	*a* [Å]	3.90204(1)	3.97291(1)
	c [Å]	4.15316(2)	3.97291(1)
	c/*a*	1.06	1
	V [Å ^{3}]	63.24(1)	62.71(1)

(b) Atom position	300 K			975 K		
	x	*y*	*z*	*x*	*y*	*z*
Pb	0	0	0	0	0	0
Ti	0.5	0.5	0.4622(4)	0.5	0.5	0.5
O1	0.5	0.5	-0.1150(9)	0.5	0.5	0
O2	0.5	0	0.3807(7)	0.5	0	0.5

(c) Bond length	300 K	975 K
Ti-O1 [Å]	1.74(1)	1.99(1)
Pb-O2 [Å]	2.51(1)	2.81(1)

Table 4-3. Determined (a) space group, lattice parameter, (b) atom position and (c) bond-length of cation and anion in $BaTiO_3$ by Rietveld refinement at 300 K and 510 K.

(a) $BaTiO_3$ at 300 K		Phase 1 Ferroelectric	Phase 2 Paraelectric	Phase 2 Paraelectric
Space group		*P*4*mm*, #99 Tetragonal	*Pm*3*m*, #221 Cubic	*Pm*3*m*, #221 Cubic
Volume fraction [%]		72.80	15.96	11.24
Lattice parameters	*a* [Å]	3.99170(1)	4.00273(3)	4.01049(6)
	c [Å]	4.02799(2)	4.00273(3)	4.01049(6)
	c/*a*	1.01	1	1
	V [Å ^{3}]	64.18(1)	64.13(1)	64.50(1)

$BaTiO_3$ at 510 K		Phase 1 Paraelectric	Phase 2 Paraelectric	Phase 3 Paraelectric
Space group		*Pm*3*m*, #221 Cubic	*Pm*3*m*, #221 Cubic	*Pm*3*m*, #221 Cubic
Volume fraction [%]		43.19	36.87	19.94
Lattice parameters	*a* [Å]	4.01550(1)	4.01727(1)	4.01903(3)
	c [Å]	4.01550(1)	4.01727(1)	4.01903(3)
	c/*a*	1	1	1
	V [Å ^{3}]	64.75(1)	64.83(1)	64.92(1)

(b) Atom position (Phase 1)	300 K			975 K		
	x	*y*	*z*	*x*	*y*	*z*
Ba	0	0	0	0	0	0
Ti	0.5	0.5	0.5118(16)	0.5	0.5	0.5
O1	0.5	0.5	-0.0244(5)	0.5	0.5	0
O2	0.5	0	0.48490(13)	0.5	0	0.5

(c) Bond length (Phase 1)	300 K	510 K
Ti-O1 [Å]	1.87(1)	2.01(1)
Ba-O2 [Å]	2.79(1)	2.84(1)

4.2 Charge density study at ferroelectric phase

With bond contraction between cation and anion in both ferroelectric phases, a notable feature was observed in MEM charge density. Two-dimensional MEM electron density map of $PbTiO_3$ and $BaTiO_3$ on the (200) and the (100) planes are shown in Figure 4-4; it is colored from 0.5 e/Å^3 (blue) to 1.3 e/Å^3 (red). Black contour lines are spaced with 0.2 e/Å^3 intervals. The bonding electron density was investigated to compare bonding characteristics and it was defined as the local minimum of the electron density betw een cation and anion. Error bar was estimated by considering the value of neighboring pixels from the minimum point of the bonding electron density. On the (200) plane which shows the Ti-O1 bond character, the bonding electron density of Ti-O1 was 1.52(7) e/Å^3 for $PbTiO_3$ and 1.24(2) e/Å^3 for $BaTiO_3$. The bonding electron density on the (100) plane for Pb-O2 and Ba-O2 was 0.46(4) e/Å^3 and 0.26(2) e/Å^3, respectively. We investigated the change of the bonding electron density from paraelectric to ferroelectric state (Table 4-4). They were larger in ferroelectric state than that in paraelectric state. For the value of the bonding electron density in Ti-O bond, it was increased by 38.82 % and 38.71 % in $PbTiO_3$ and $BaTiO_3$, respectively, showing the similar change tendency. However, it was obviously different in Pb(Ba)-O bond; it was increased by 80.85 % and 42.31 % in $PbTiO_3$ and $BaTiO_3$, respectively. As a result, the higher value of bonding electron density between cation Ti, Pb and anion O was observed in $PbTiO_3$; it indicates a strong covalent property, especially in Pb-O bond. In addition, the strong Pb-O covalent characteristic is a good accordance with the theoretical calculation by Cohen,[62] who reported the hybridization between Pb and O states leads to a large strain and large ferroelectric polarization.

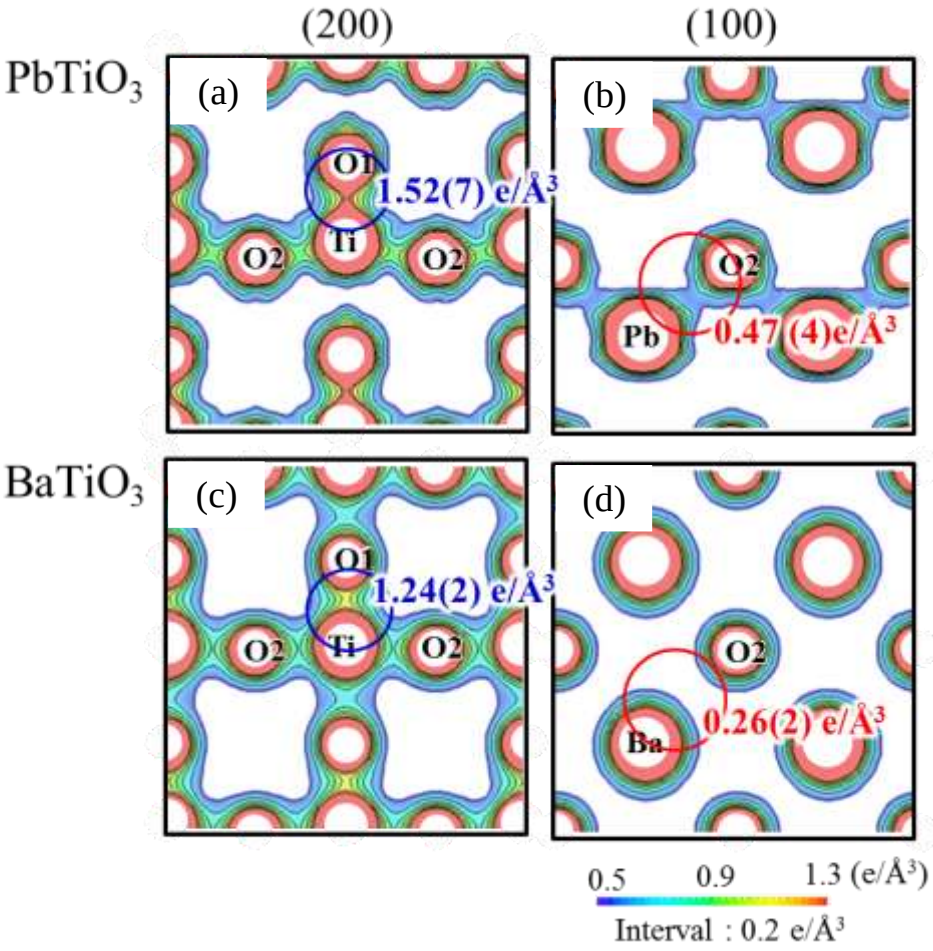

Figure 4-4. MEM charge density distribution on (a) (200) and (b) (100) planes in $PbTiO_3$ and on (c) (200) and (d) (100) in $BaTiO_3$.

Table 4-4. Value of the bonding electron density in $PbTiO_3$ and $BaTiO_3$ at high temperature paraelectric phase.

e/Å ^{3}

	$PbTiO_3$ 975 K	$BaTiO_3$ 510 K
Ti-O	0.93(2)	0.76(2)
Pb(Ba)-O	0.09(4)	0.15(1)

4.3 Electrostatic potential study of $PbTiO_3$ and $BaTiO_3$

In order to investigate the charge density level structure with the strong covalent characteristic, we visualized the electrostatic potential of ferro and paraelectric phase in $PbTiO_3$ and $BaTiO_3$. Figure 4-5 and Figure 4-6 show two-dimensional electrostatic potential maps on the (200) and the (100) planes at ferroelectric and paraelectric state. The electrostatic potential is colored with values from -18 V (blue color region) to 3.6 V (red color region). Black lines are equi-potential lines with 3.6 V intervals. Black arrows in Figure 4-5 indicate the electric vectors obtained by the minus gradient of electrostatic potential at each point.

In $PbTiO_3$, the electrostatic potential around ions was distributed asymmetrically at ferroelectric phase, whereas it showed isotropic distribution at paraelectric phase. The electrostatic potential between Ti and O1 ion at ferroelectric phase, 13.5(4) V, was higher than that at paraelectric phase, -6.2(2) V. The bonding electrostatic potential of Pb-O2 was changed from -22.9(1) V to -11.6(1) V with para and ferroelectric phase transition. Especially, the asymmetrical degree around Pb and O2 ions was significantly enhanced at ferroelectric phase as shown in Figure 4-7; around Pb ion, the lower equipotential line showed a gradual slope with smooth curves, in comparison to the closely spaced upper equipotential line. On the other hands, the electrostatic potential around O2 had an opposite character. These effects led to an extremely asymmetrical distribution of the electrostatic potential around the Pb and O2 ions, which arose from a separated electrostatic potential distribution on the Pb and O2 ions. Such a separated electrostatic potential distribution on

an atom is indicated as a signature of electronic polarization. Electronic polarization is mainly observed in anion. In this result, the electrostatic potential revealed that Pb ion has strong electronic polarization.

Contrary to the $PbTiO_3$, the bonding electrostatic potential of TiO_3 in $BaTiO_3$ was slightly increased from -7.4(2) V to -2.5(3) V with cooling. The electrostatic potential around Ba and O2 ion showed almost symmetrical distribution as shown in Figure 4-7; no electronic polarization of Ba ion was observed in three-dimensional electrostatic potential map.

For overall visualization of polarization in $PbTiO_3$ and $BaTiO_3$, three dimensional electrostatic potential is represented in Figure 4-8. Electrostatic potential is colored on the 0.95 e/Å^3 isosurface of MEM electron density from 0 V (blue) to 8.6 V (red). As shown in Figure 4-8, distinct difference of electrostatic potential distribution between Ti and O1 in both materials was observed. It is indication of ionic polarization at Ti-O2 bond. In addition, the difference was larger in $PbTiO_3$ than that in $BaTiO_3$; it qualitatively visualized that Ti-O2 bond of $PbTiO_3$ has large ionic polarization. Electron density at Ba atom showed blue color of low electrostatic potential without any distribution of it. On the other hands, strongly separated electrostatic potential on the electron density of Pb atom was visualized; the top area of the surface was red, while the bottom area was almost green. This result indicates that electron density of Pb atom was displaced to the center of nucleus charge, which is evident of atomic polarization of Pb atom. These results are correspondent to the reported result which quoted that hybridization between Pb and O causes atomic polarization of Pb atom.

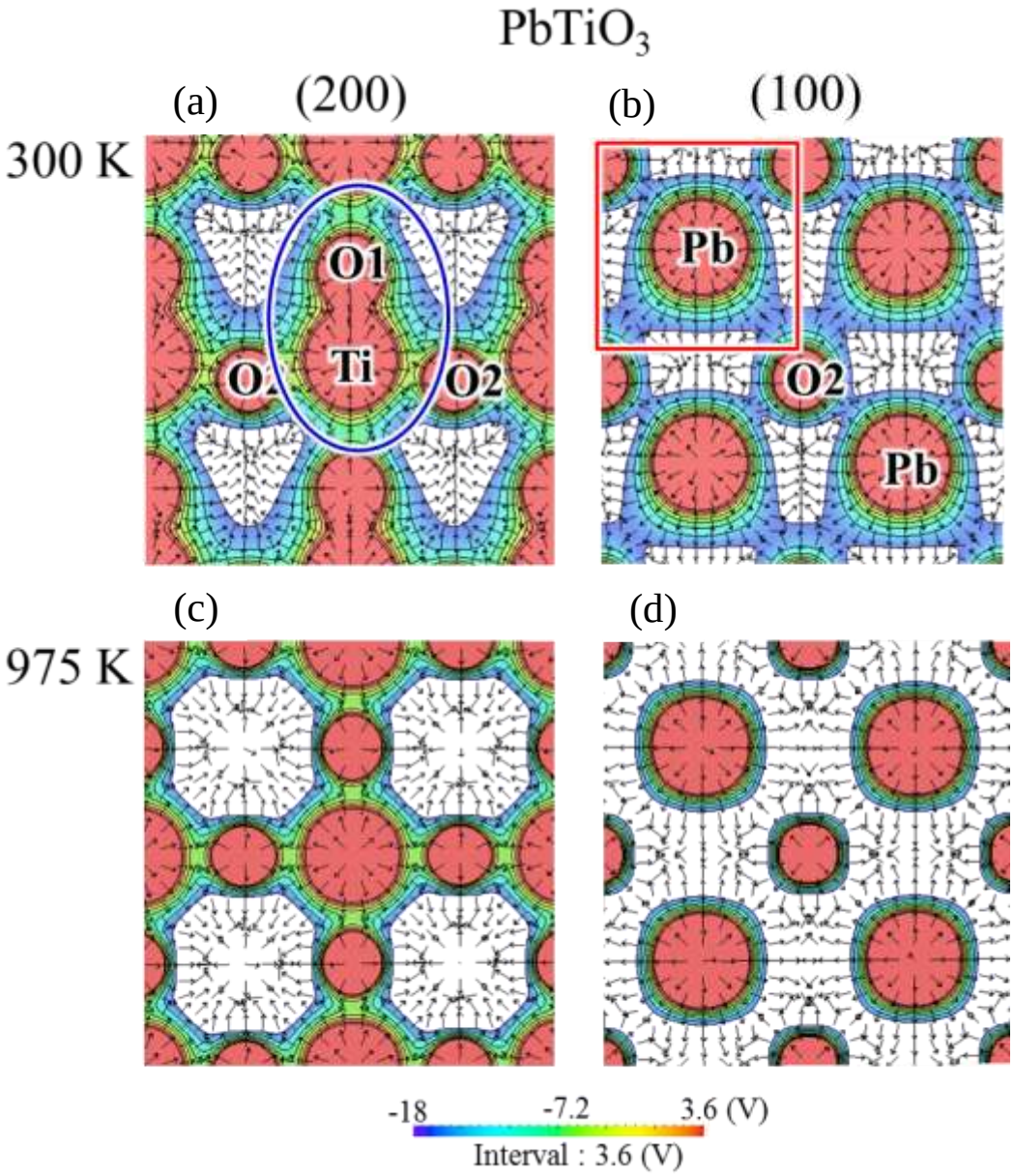

Figure 4-5. Two-dimensional electrostatic potential map of $PbTiO_3$ on (a) (200) and (b) (100) at 300 K and on (c) (200) and (d) (100) at 975 K.

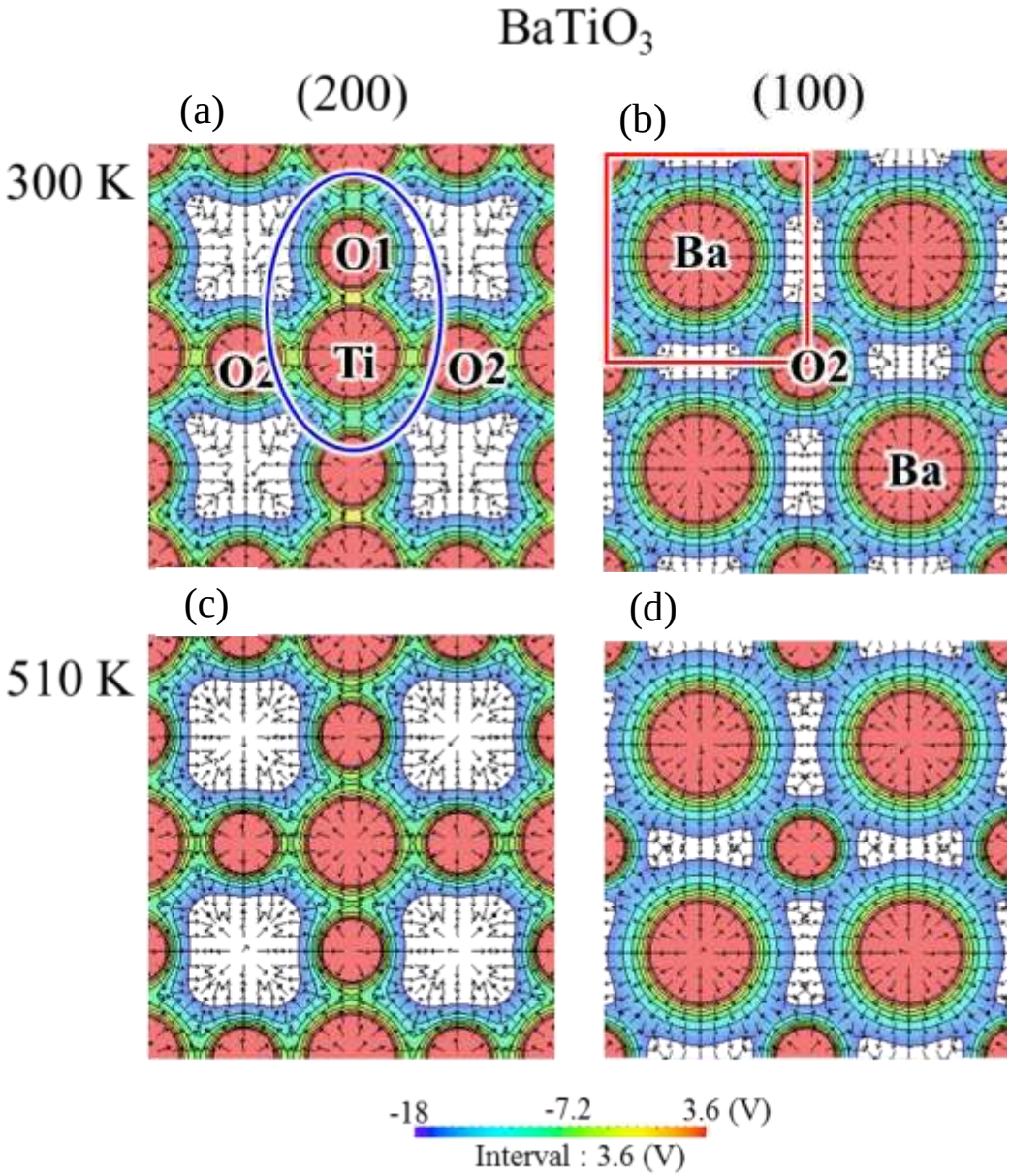

Figure 4-6. Two-dimensional electrostatic potential map of $BaTiO_3$ on (a) (200) and (b) (100) at 300 K and on (c) (200) and (d) (100) at 510 K.

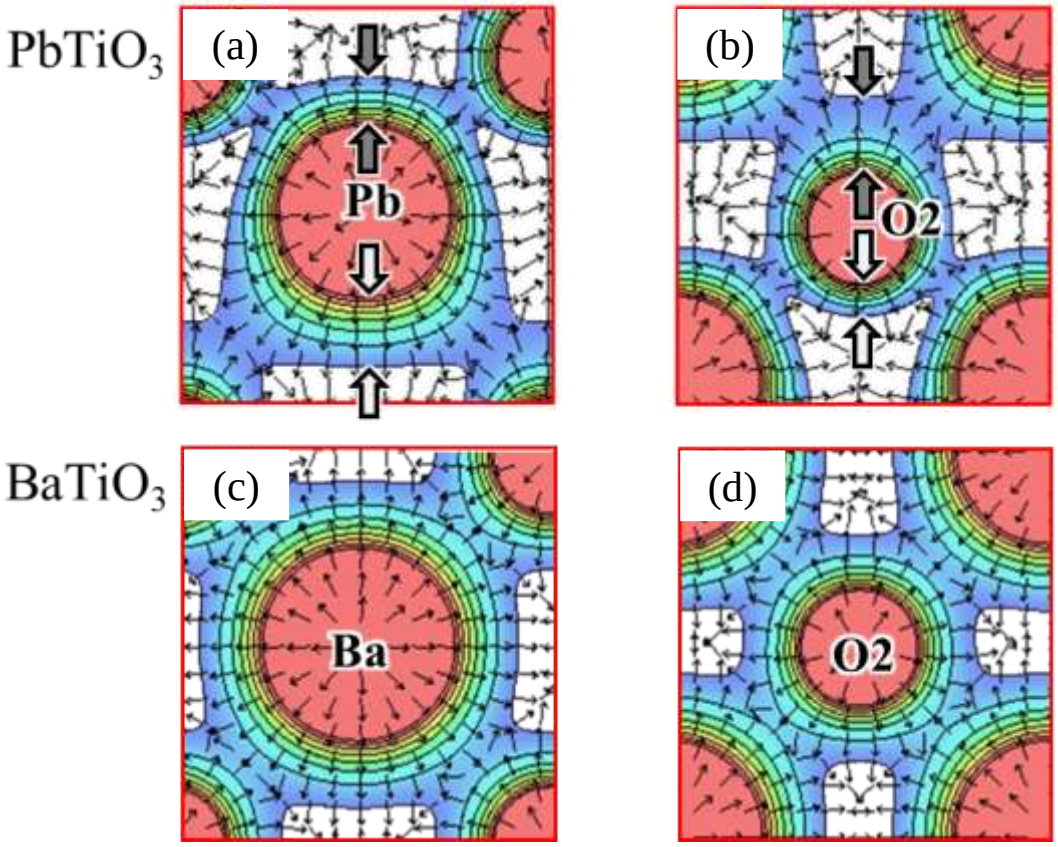

Figure 4-7. Magnified two-dimensional electrostatic potential map around (a) Pb and (b) O2 in $PbTiO_3$ and (c) Ba and (d) O2 in $BaTiO_3$ at 300 K.

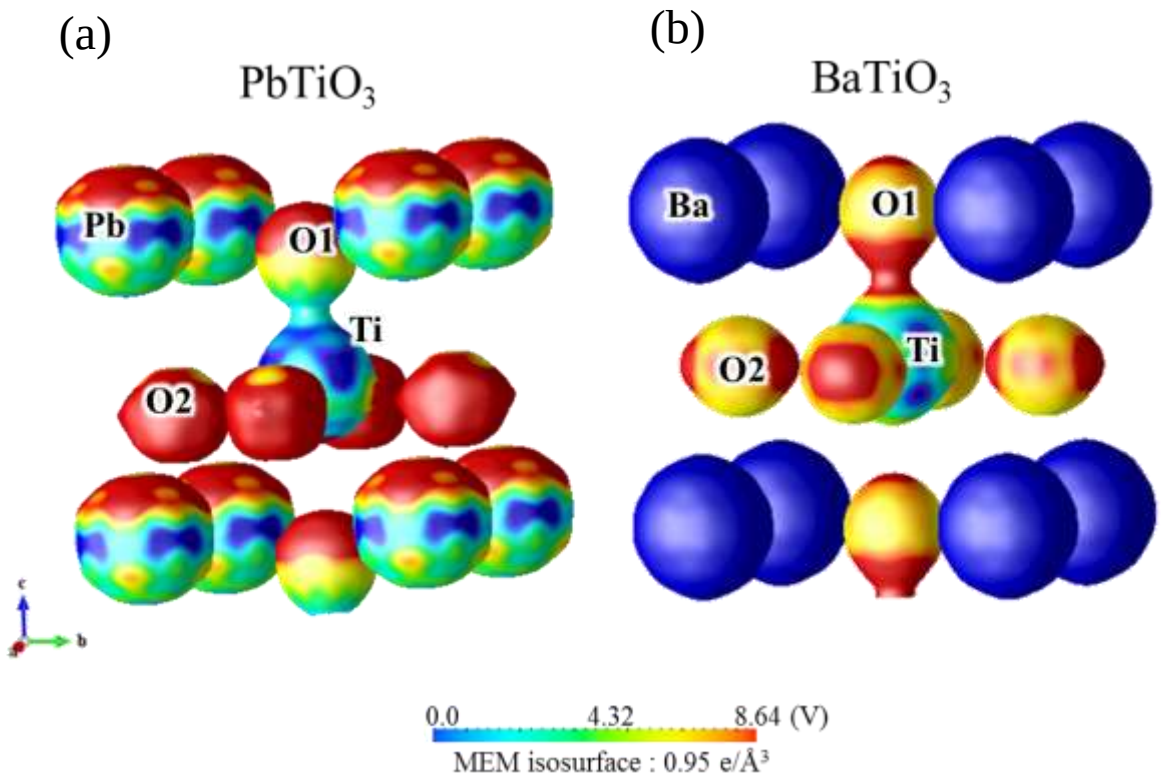

Figure 4-8. Three-dimensional electrostatic potential distribution in (a) $PbTiO_3$ and (b) $BaTiO_3$.

4.4 Local polarization by structural information

– Validity test of the MaxEnt/fragment EP method -

We estimated the polarization value of $PbTiO_3$ and $BaTiO_3$ at different cases to obtain the validity of the MaxEnt/fragment EP method. At first, point charge model, what we call Case 1 was applied. It used the displacement of cation and anion with the formal charge of each atom, for example, Pb(Ba), Ti and O were considered to have +2, +4, -2 formal charge, respectively. Other cases estimated the polarization value using the electron charge density surrounded by the electrostatic potential boundary. The boundary for the electron density at each case was determined by following the local minimum of electrostatic potential. The only different thing for each case was the combination of pair which each atom can compose. We termed them as each atom model, Case 2, neighboring pair model, Case 3, and fragment model, Case 4.

At the each atom model, the electron density distribution of each atom was distinguished without any formation of pair. At the Case 3, the nearest neighboring of cation and anion was treated as a pair. For example, the nearest anion from Ti cation was O1 anion and that from Pb(Ba) cation was O2 anion, showing TiO and $Pb(Ba)O_2$ pairs in the unit cell. The boundary of each pair was determined by following the local minimum of electrostatic potential around cation and anion pair. The Case 4 is the fragment method. In order to determine the fragments in the structure, we investigated the local minimum electrostatic potential value between cation and anion; it was listed in Table 4-5. With O1 as a center, two neighboring cations exist; the bonding electrostatic potential value of O1-Pb was -14.8(1) V and that of O1-Ti was 13.5(4) V. Along with the determination method of the

fragment, the Ti-O1 was designated as a pair. Likewise, the bonding electrostatic potential values of O2-Pb and O2-Ti were compared: O2-Pb is -17.6(1) V and that of O2-Ti is -4.3(1) V. The O2-Ti forms a pair. As a result, O1-Ti-O2 was designated as one fragment and Pb was also decided as the other fragment. It resulted in the Pb and TiO_3 fragments in $PbTiO_3$. In the same method, two fragments, O1-Ti-O2 (TiO_3) and Ba, were decided in $BaTiO_3$.

In Table 4-6, 4-7 and 4-8, we showed the electron density of local structure at each case: the each atom model, the neighboring pair model and the fragment model. Yellow color is the boundary of determined local structure. We found that total number of electron charge in the each local structure was same with total nucleus charge, showing the charge neutrality of local structure by the minimum of electrostatic potential in the error range.

Table 4-5. Bonding electrostatic potential value of $PbTiO_3$ and $BaTiO_3$.

V

Anion	Cation	$PbTiO_3$	$BaTiO_3$
O1	Pb(Ba)	-14.8(1)	-15.6(1)
	Ti	13.5(4)	-2.5(3)
O2	Pb(Ba)	-17.6(1)	-15.7(1)
	Ti	-4.3(1)	-5.3(1)

Table 4-6. Nucleus and electron charge at each atom of (a) $PbTiO_3$ and (b) $BaTiO_3$.

(a)

$PbTiO_3$	Pb	O1	O2(a)	O2(b)	Ti
					
Nucleus charge	82	8	8	8	22
electron charge	81.99(1) e	8.02(1) e	8.00(1) e	8.00(1) e	21.98(2) e

(b)

$BaTiO_3$	Ba	O1	O2(a)	O2(b)	Ti
					
Nucleus charge	56	8	8	8	22
electron charge	55.98(1) e	8.02(2) e	8.02(1) e	8.02(1) e	21.97(1) e

Table 4-7. Nucleus and electron charge at $Pb(Ba)O_2$ and TiO pairs of (a) $PbTiO_3$ and (b) $BaTiO_3$.

(a)

$PbTiO_3$	PbO_2	TiO
		
Nucleus charge	98	30
electron charge	97.99(2) e	30.00(3) e

(b)

$BaTiO_3$	BaO_2	TiO
		
Nucleus charge	72	30
electron charge	72.02(2) e	29.99(3) e

Table 4-8. Nucleus and electron charge in the fragments of (a) $PbTiO_3$ and (b) $BaTiO_3$.

(a)

$PbTiO_3$	Pb fragment	TiO_3 fragment
		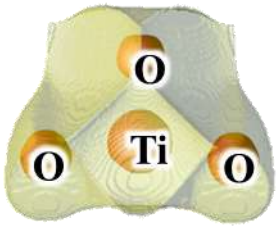
Nucleus charge	82	46
electron charge	81.99(1) e	46.01(1) e

(b)

$BaTiO_3$	Ba fragment	TiO_3 fragment
		
Nucleus charge	56	46
electron charge	55.98(1) e	46.02(4) e

The polarization was calculated with equation 2.32. The position of nucleus charge was obtained from the result of Rietveld refinement. The MEM electron charge density of all pixels in the local was quantized, and it was used as negative charge in the calculation. The results are listed in Table 4-9.

For point charge mode, polarization value for $PbTiO_3$ and $BaTiO_3$ was 57.4(2) $\mu C/cm^2$ and 14.4(1) $\mu C/cm^2$, respectively. The result seems to be in a good accordance with the reported results. However, this method has a problem. It cannot consider the electron density distribution during the calculation process for polarization. For this reason, it may provide the reliable polarization value in the simple structure such like Perovskite structure. This method, however, cannot be directly applied to the complex-structure system, in which the electron density distribution is deeply related to the ferroelectric property.

Therefore, we estimated the polarization value based on the electron charge density in this study. The polarization values of the each atom model, the neighboring pair model and the fragment model were compared, and we tried to find the most appropriate method.

In the Case 2, high covalency and ionic polarization between atoms were not considered during the polarization calculation because there was no pair between cation and anion. The obtained total polarization for $PbTiO_3$ and $BaTiO_3$ was 29.9(2) $\mu C/cm^2$ an d 16.5(9) $\mu C/cm^2$. In the Case 3, there was two local structures, Pb(Ba)-O_2 and Ti-O pairs in the unit cell. Although, it contained the high covalency between Ti and O in Ti-O pair, there was also a large covalency between Pb(Ba)-O_2 and Ti-O pairs with the value of 0.72(2) $e/Å^3$ and 0.79(1) $e/Å^3$ for $PbTiO_3$ and $BaTiO_3$, respectively, as shown in Figure 4-4. In addition, there was high electrostatic potential interaction between pairs, and it was difficult to find the physical property of each local structure. The obtained total polarization for P

$bTiO_3$ and $BaTiO_3$ was 31.9(9) μC/cm^2 and 16.7(9) μC/cm^2 in the neighboring model. As we expected, covalency between the local structures affected the polarization value. Polarization was underestimated, especially in $PbTiO_3$, which has the high covalency characteristics.

On the other hands, fragment method can provide the local structure for the electron density by considering the electrostatic potential interaction. The local structure was termed as fragment, in which the fragments have the minimized covalency as well as the electrostatic potential interaction to each other. Although there is still relatively enhanced covlaency between Pb and TiO_3 fragments with the value of 0.47 e/Å^3, we expect that the fragment model is the most appropriate method for the estimation of polarization using the electron density. The estimated polarization value of TiO_3 fragment for $PbTiO_3$ and $BaTiO_3$ was 32.9(1) μC/cm^2 and 16.8(1) μC/cm^2, respectively. Total polarization of $PbTiO_3$ in the fragment model was the largest than that in the others.

Table 4-9. Polarization of $PbTiO_3$ and $BaTiO_3$ at each case.

μC/cm^2

	$PbTiO_3$	$BaTiO_3$
Case 1	57.4(2)	14.4(1)
Case 2	29.9(2)	16.5(9)
Case 3 $Pb(Ba)O_2$+TiO	31.9(9)	16.7(9)
Case 4 Pb(Ba)+TiO_3	33.5(2)	17.0(1)
PE measurement	52~75 [63,66]	15~25 [68,70,73]
First-principle calculation	70~87 [64,65,67]	23~29 [69,71,72,74]

By the MaxEnt/fragment EP method, we estimated the local polarization at each fragment in $PbTiO_3$ and $BaTiO_3$ in Table 4-10. The estimated polarization value of TiO_3 fragment for $PbTiO_3$ and $BaTiO_3$ was 32.9(1) $\mu C/cm^2$ and 16.8(1) $\mu C/cm^2$, respectively; the value of Pb was estimated with the value of 1.6(2) $\mu C/cm^2$, while Ba showed the almost 0 within the error range. With this result, TiO_3 is the dominant factor for polarization of $PbTiO_3$ and $BaTiO_3$. In addition, polarization value of TiO_3 fragment in $PbTiO_3$ was larger than that in $BaTiO_3$. This is exactly consistent to the visualized result of three-dimensional electrostatic potential; it shows the apparent color separation as large ionic polarization of TiO_3 and atomic polarization of Pb atom in $PbTiO_3$.

As reported result by *PE* measurement and first-principle calculation, the polarization of $PbTiO_3$ was estimated with larger value than that of $BaTO_3$ in our result. The total polarization values were compared to the reported results. For $BaTiO_3$, the resultant value of 17.0(1) $\mu C/cm^2$ showed a very good accordance with reported results. On the other hands, the total polarization of $PbTiO_3$ was under estimated. We assumed that the gap of polarization value between the obtained result and the reported result in $PbTiO_3$ is due to poorly considered covalent property between Pb and O ions.

Although the MaxEnt/fragment EP method has a limited estimation of the polarization value in covalent system, it must be available in the order estimation of polarization. In addition, for the ionic system, the MaxEnt/fragment EP method is a powerful method for obtaining the polarization value. Because of this property, we expect that the MaxEnt/fragment EP method can provide the reliable local/total polarization in a system which has a weak-electrostatic potential interaction such like a layered structure system.

Table 4-10. Polarization of $PbTiO_3$ and $BaTiO_3$ from the MaxEnt/fragment EP method.

$\mu C/cm^2$

		$PbTiO_3$	$BaTiO_3$
MaxEnt/fragment EP method	TiO_3	32.9(1)	16.8(1)
	Pb(Ba)	1.6(2)	0.2(1)
	Total	33.5(2)	17.0(1)
PE measurement		52~75 [63,66]	15~25 [68,70,73]
First-principle calculation		70~87 [64,65,67]	23~29 [69,71,72,74]

Chapter 5

Study of polarization in layered structure Bi_2SiO_5 by the MaxEnt/fragment EP method

We applied the MaxEnt/fragment EP method to recently discovered Pb-free material, Bi_2SiO_5. We successfully estimated the total polarization as well as local polarization of Bi_2SiO_5. In addition, we found that a large polarization of the material result in the polarization of silicate layer; although BiO showed a large polarization, Bi_2O_2 layer revealed a small polarization, because of the opposite direction of BiO local polarization.

In this chapter, we described the result of a precise structure of para- and ferroelectricity as well as local/total polarization of Bi_2SiO_5 in detail. Based on the result of local/total polarization, we discussed the role of polarization in layered structure Bi_2SiO_5.

5.1 Crystal structure and property of Bi_2SiO_5

Bi_2SiO_5 has the Aurivillus-like structure,[81~84] in which the SiO_3 layer was sandwiched by the Bi_2O_2 layer. Schematic view of Bi_2SiO_5 crystal structure is shown in Figure 5-1(a). In the Bi_2O_2 layer, Bi atoms are located alternatively above and below the squared oxygen planes.[85,86] $6s^2$ lone pair electrons of Bi atoms seem to be located in opposite direction relative to the oxygen square plane. As a result, a strong stereochemical activity of the Bi atoms is formed and it leads to the structural distortion of Aurivillius structure materials.[86~88] Between the Bi_2O_2 layers, the SiO_3 chain structure is located with a form of corner-sharing SiO_4 tetrahedrons.

So far, Bi_2SiO_5 was known as insulator buffer layer for the deposition of Bi_4TiO_{12} thin film.[88,89] It is used to reduce the mismatch with silicon oxide. No structural phase transition was reported, although crystal structure was reported as orthorhombic structure with $Cmc2_1$ space group. Recently, ferroelectric property in this material was discovered by the dielectric measurement and the Raman spectrum experiment.[51] In the temperature dependent dielectric measurement, weak thermal hysteresis was observed and the value of dielectric constant was maximized at around 673 K. This temperature was supposed to the Curie temperature, T_c, of ferroelectric Bi_2SiO_5. Raman spectrum measurement revealed that Bi_2SiO_5 material has soft phonon mode: low frequency peak decreases toward zero as temperature is approaching the Curie temperature. These results indicated that Bi_2SiO_5 material has displacive-type ferroelectric phase transition. Although Bi_2SiO_5 showed a property of ferroelectrcity at 300 K, ferroelectric polarization of *a*-axis with a small value was only measured, because of thin-plate shape of single crystal (Figure 5-2(b)); the

ceramic sample cannot be synthesized due to the sensitive heating property. In addition, reported space group of Bi_2SiO_5, *Cmc*2_1, cannot have ferroelectric polarization along the a-axis because of a mirror plane symmetry operation. For this reason, we carried out accurate structure determination of Bi_2SiO_5 at 300 K and estimated the polarization value by Synchrotron radiation X-ray powder diffraction experiment in this study.

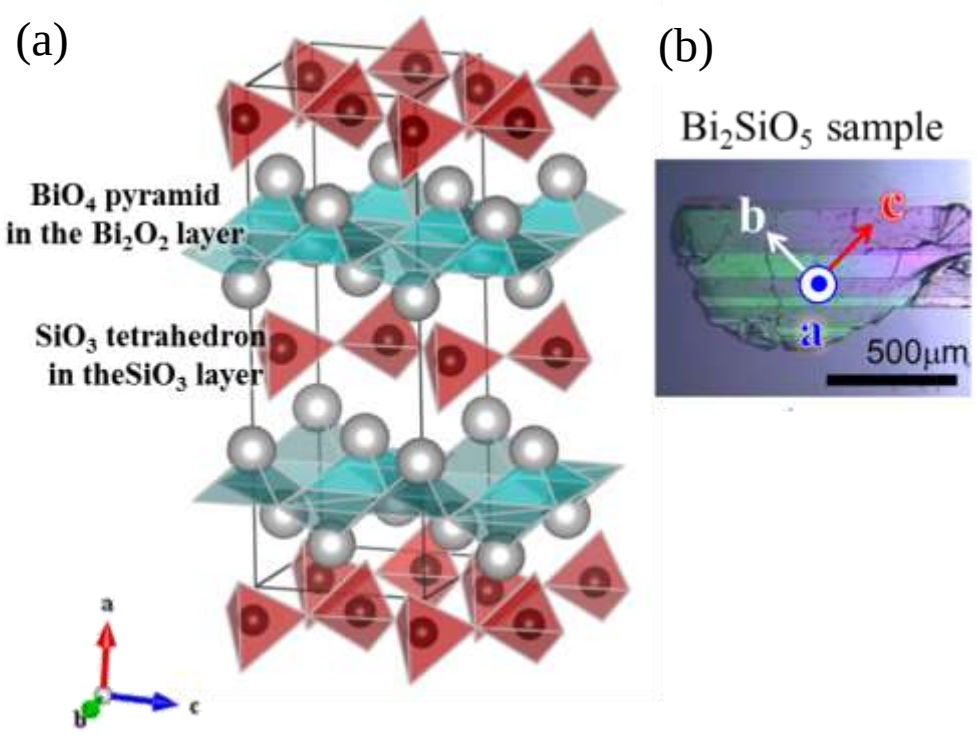

Figure 5-1. (a) Crystal structure of Bi_2SiO_5 and (b) shape of fabricated single crystal sample.

5.2 Crystal structure determination of Bi_2SiO_5 at 300 K

In order to clarify the crystal structure at the atomic position level, we carried out synchrotron X-ray powder diffraction. For determination of space group, Dicvol program was used. It can predict the crystal structure such as the Bravais structure and the lattice parameters using 2θ peak positions. We analyzed the 20 diffraction peaks from low angle in 2θ of the Bi_2SiO_5 powder diffraction data. As a result, the orthorhombic structure and the monoclinic structure are available for Bi_2SiO_5 material at 300 K. (Table 5-1) In addition to the analysis, we carried out TEM measurement;[51] it was found that this material has monoclinic system at 300 K. Using the information of monoclinic system, we investigated the point groups which allows the ferroelectricity and determined the space group using reflection condition.[90]

The monoclinic structure has C_2, C_s and C_{2h} point groups. In these point groups, C_{2h} point group is excluded, because of its inversion symmetry. Therefore, C_2 and C_s point groups are allowed for monoclinic structure with ferroelectricity. The space groups belonged to C_2 and C_s point groups are listed in Table 5-2. Reflection condition of each space group was investigated according to the indexing of diffraction peak as shown in Figure 5-2. It shows that the lowest 2θ peak in Bi_2SiO_5 is the (200) plane, not the (100) plane. For this reason, the primitive space group is removed from the possible lists. Of the remaining space groups, *C*2, *Cm* and *Cc*, we found that *Cc* space group is the most appropriate for this system, because $l = 2n$ condition for 00l reflection only appeared in the *Cc* space group.

Table 5-1. Predicted lattice parameters by using Dicvol program.

	Orthorhombic	Monoclinic
a [Å]	15.115(3)	15.108(5)
b [Å]	5.444(1)	5.442(2)
c [Å]	5.291(1)	5.292(2)
β [°]	90	90.054

Table 5-2. Reflection conditions of space groups in C_2 and C_s point groups.

	*P*2, #3	*P*2$_1$, #4	*C*2, #5	*Pm*, #6	*Pc*, #7	*Cm*, #8	*Cc*, #9
hkl	-	-	$h+k=2n$	-	-	$h+k=2n$	$h+k=2n$
*h*0*l*	-	-	$h= 2n$	-	$l=2n$	$h= 2n$	$h,l = 2n$
0*kl*	-	-	$k=2n$	-	-	$k=2n$	$k=2n$
*hk*0	-	-	$h+k=2n$	-	-	$h+k=2n$	$h+k=2n$
0*k*0	-	-	$k=2n$	-	-	$k=2n$	$k=2n$
*h*00	-	-	$h=2n$	-	-	$h=2n$	$h=2n$
00*l*	-	$l=2n$	-	-	$l=2n$	-	$l=2n$

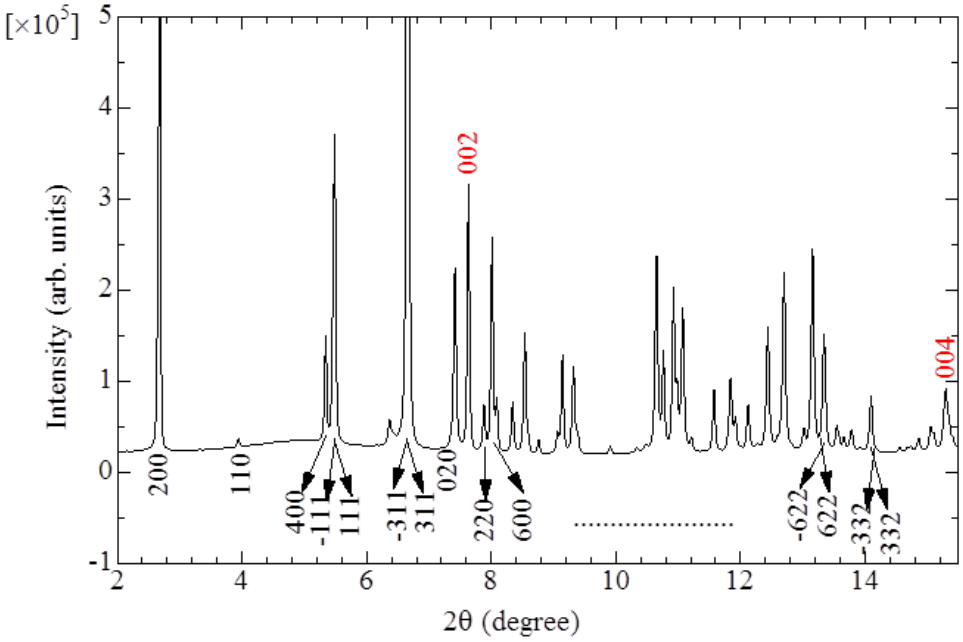

Figure 5-2. Indexing of diffraction peaks of Bi_2SiO_5 by Dicvol program.

With the *Cc* space group at 300 K of Bi_2SiO_5, precise structure analysis was carried out by using MEM/Rietveld refinement. The MEM/Rietveld analysis enables us to construct the optimized structural model based on the charge density level structure. In this way, the structure modeling is provided by the charge density imaging and the Rietveld powder-pattern fitting based on model. Process of structure determination using MEM/Rietveld refinement was shown in Figure 5-3. At first stage, preliminary Rietveld refinement was performed with known structure using Synchrotron Radiation X-ray powder diffraction data. In this case, lattice parameter and only Bi atom position were inputted as primitive structural model. MEM analysis is carried out with the total charge and the structural factor obtained by integral intensities of peaks. Based on the MEM charge density imaging, the model is reconstructed. This iteration was continued until the value of the reliable factors is less than 5 %, and the presumed model was accorded to revised model by charge density imaging. The non-isothermal temperature factor was refined by final result.

The result of Rietveld refinement with optimized crystal structure was shown in Figure 5-4. The observed and calculated results are indicated by red dot and blue line. Sky blue line shows background of the X-ray diffraction data. Green line is the difference between the calculated and observed data. The reliability, R_{wp} and R_I are 3.13 % (3.27 %) and 3.68 % (3.99 %) at 300 K (773 K), respectively. Determined lattice parameter and space group was shown in Table 5-3. Low values of the R-factors (< 4 %) ensure a reliability of the structural parameters determined by Rietveld refinement. The atom position and non-iso thermal displacement parameters are listed in Table 5-4 and 5-5. As a result, we found that Bi_2SiO_5 material has the structural phase transition from the orthorhombic to the monoclinic structure as temperature decreases with subtle change of the beta angle.

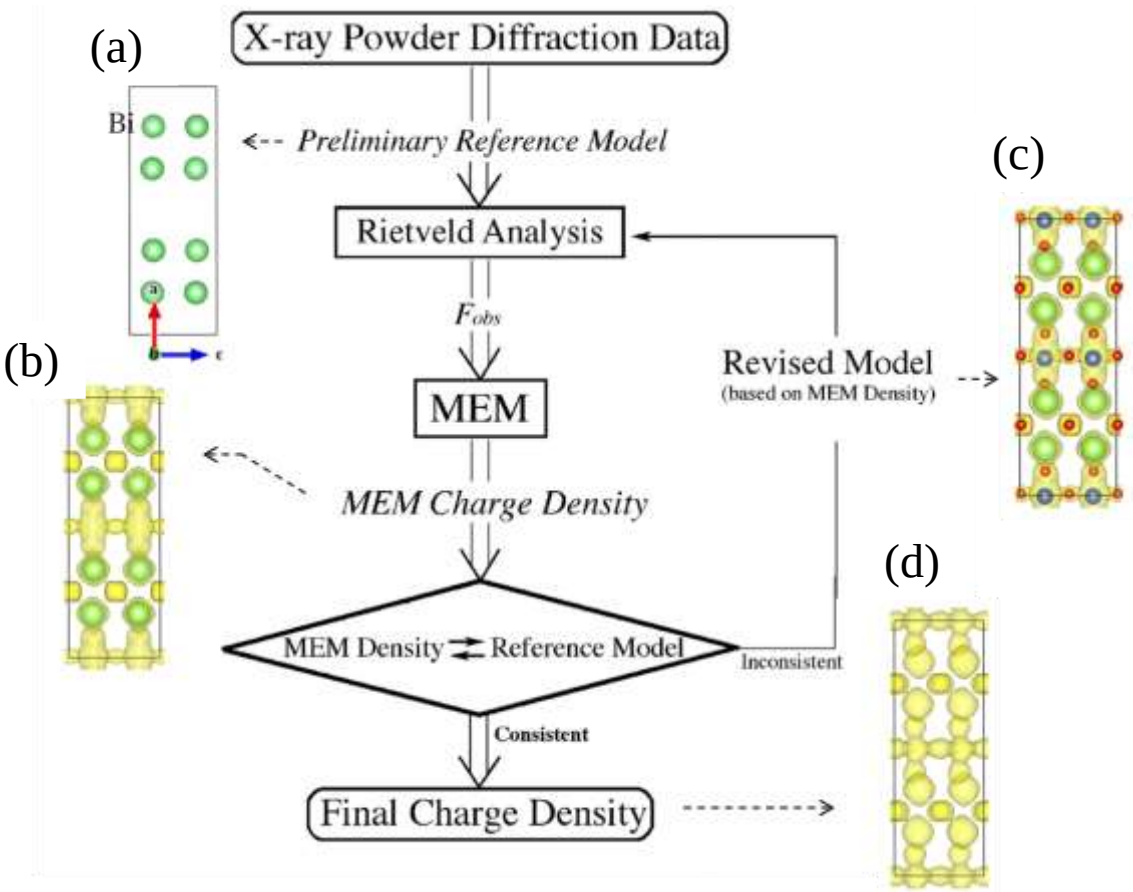

Figure 5-3. Process of precise structure determination by MEM/Rietveld method.

(a)

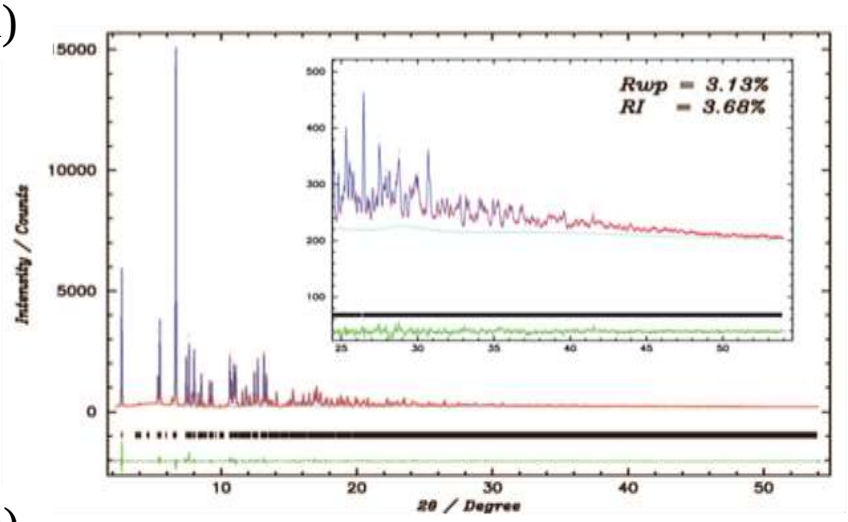

(b)

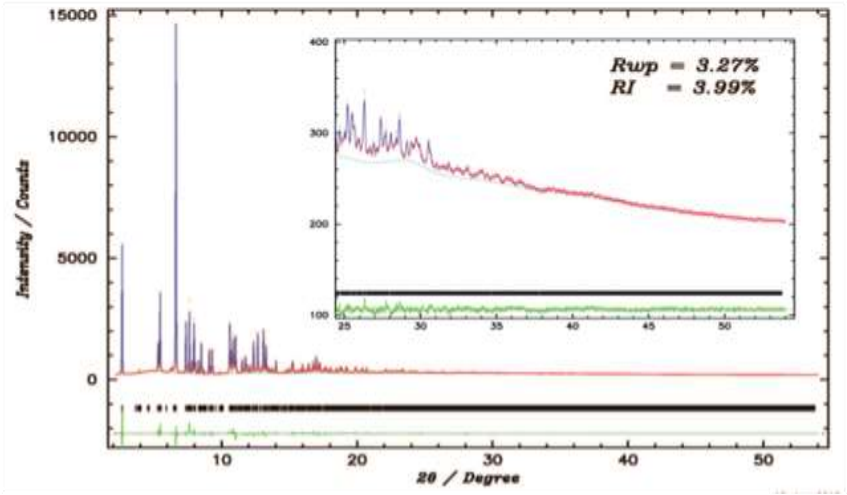

Figure 5-4. Results of Rietveld refinement at (a) 300 K and (b) 773 K.

Table 5-3. Lattice parameters and reliability factors of Rietveld refinement of Bi_2SiO_5

Bi_2SiO_5		**300K Ferroelectric**	**773K Paraelectric**
Space group & crystal system		*Cc*, #9 Monoclinic	*Cmcm*, #63 Orthorhombic
Lattice parameter	*a* [Å]	15.1193(1)	15.1968(1)
	b [Å]	5.4435(1)	5.4843(1)
	c [Å]	5.2892(1)	5.2964(1)
	β [°]	90.070(2)	90°
	V [Å ^{3}]	435.31(1)	441.42(1)
Reliability factors	R_I [%]	3.13	3.27
	R_{wp} [%]	3.68	3.99

Table 5-4. Atom position of Bi_2SiO_5 for (a) monoclinic phase at 300 K and (b) orthorhombic phase at 773 K.

(a) 300 K

Atom	Site	*x*	*y*	*z*
Bi(a)	*4a*	0.170(1)	0.217(1)	0.261(1)
Bi(b)	*4a*	0.840(1)	0.219(2)	0.274(5)
Si	*4a*	0.496(1)	0.172(1)	0.246(1)
O(a),O(b)	*4a*	0.250(2)	0.494(9)	0.495(6)
O(c),O(d)	*4a*	0.256(2)	0.007(12)	0.035(10)
O(e),O(f)	*4a*	0.490(2)	0.017(2)	0.511(5)
O(g)	*4a*	0.586(1)	0.331(2)	0.225(4)
O(h)	*4a*	0.404(1)	0.323(2)	0.227(4)

(b) 773 K

Atom	Site	*x*	*y*	*z*
Bi	*8g*	0.165(1)	0.218(1)	0.250
Si	*4c*	0	0.686(1)	0.250
O(a~d)	*8e*	0.248(1)	0.500	0.500
O(e),O(f)	*4b*	0	0.500	0.500
O(g),O(h)	*8g*	0.092(1)	0.181(2)	0.750

Table 5-5. Thermal displacement parameters of Bi_2SiO_5 at (a) 300 K and (b) 773 K.

(a) 300 K

Atom	U	U_{11}	U_{22}	U_{33}
Bi(a)	-	0.008(1)	0.008(1)	0.007(1)
Bi(b)	-	0.008(1)	0.008(1)	0.007(1)
Si	-	0.013(3)	0.010(3)	0.012(4)
O(a),O(b)	0.029(5)	-	-	-
O(c),O(d)	0.029(5)	-	-	-
O(e),O(f)	-	0.022(9)	0.031(9)	0.031(9)
O(g),O(h)	0.029(5)	-	-	-

(b) 773 K

Atom	U	U_{11}	U_{22}	U_{33}
Bi	-	0.024(1)	0.022(1)	0.025(1)
Si	-	0.019(4)	0.022(4)	0.016(4)
O(a~d)	0.039(3)	-	-	-
O(e),O(f)	-	0.033(11)	0.040(10)	0.049(13)
O(g),O(h)	0.039(27)	-	-	-

Determined structure of Bi_2SiO_5 at 300 K and 773 K is shown in Figure 5-5. It has a layered structure, in which the SiO_3 layer is positioned between the Bi_2O_2 layers and is stretched along the *b*-*c* plane. At high temperature paraelectric phase, the SiO_3 layer was located exactly at the midpoint between the Bi_2O_2 layers. In addition, Si, Bi and O atoms vertically bonded to Si were aligned in the same direction. On the other hands, at room temperature, the SiO_3 layer was displaced to (-) *a*-direction by phase transition and it caused unequal interlayer distance between the SiO_3 and the Bi_2O_2 layer. This structure distortion of the SiO_3 layer seemed like to form the dimer of the SiO_3 and the Bi_2O_2 layer. O atoms in the Bi_2O_2 layer are distorted, and they showed a twisted square plane. Furthermore, O atoms bonded vertically to Si in the SiO_3 layer are also displaced to the (-) *c*-axis.

Structural distortion of the inner layer region is shown in Figure 5-6. It is drawn onto the *b*-*c* plane for the SiO_3 layer and *a*-*c* plane for the Bi_2O_2 layer. For the SiO_3 layer, Si atom is exactly positioned at the midpoint between oxygen atoms at 773 K. However, bond length of Si-O bonding changed to cause unequal bond length between Si and O atoms at ferroelectric phase. Moreover, bonding angle in the SiO_3 layer was also changed from 180 ° to 172 ° with a distortion of the O grid shown as red dot lines. For the Bi_2O_2 layer, angle between O square planes changed from 180 ° to 176.9 ° by phase transition.

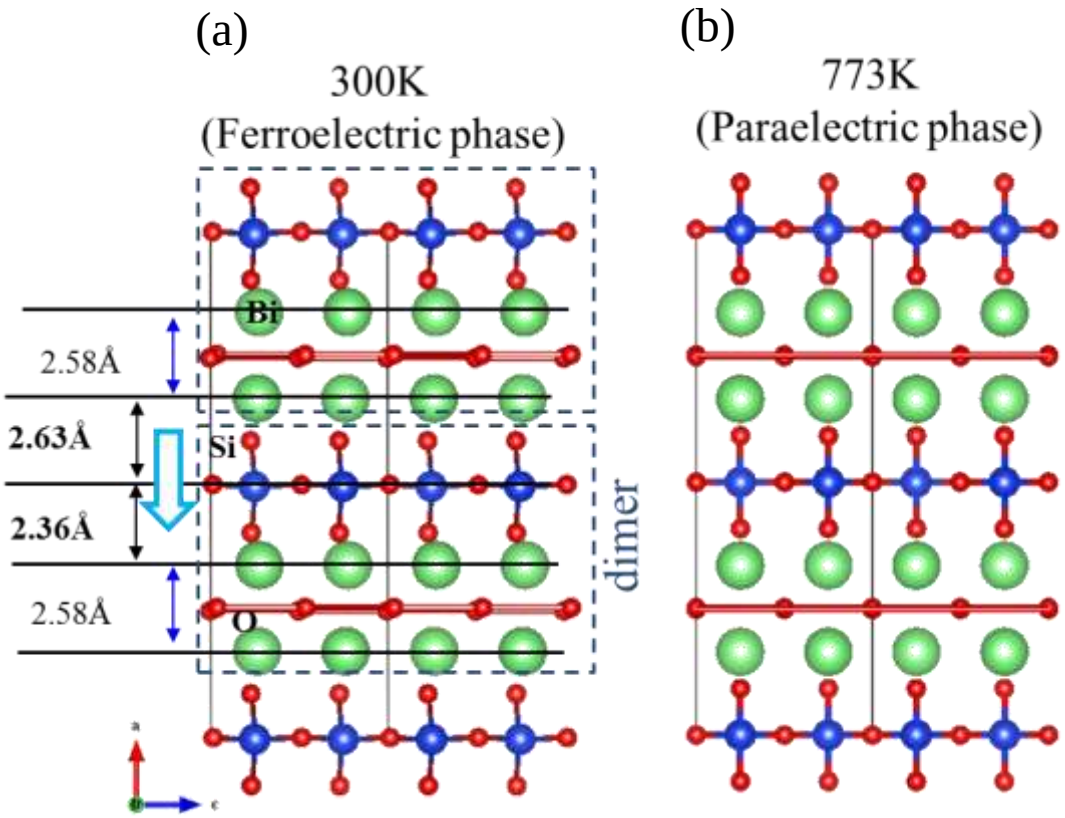

Figure 5-5. Structure of Bi_2SiO_5 projected onto the out-of-plane direction at (a) 300 K and (b) 773 K.

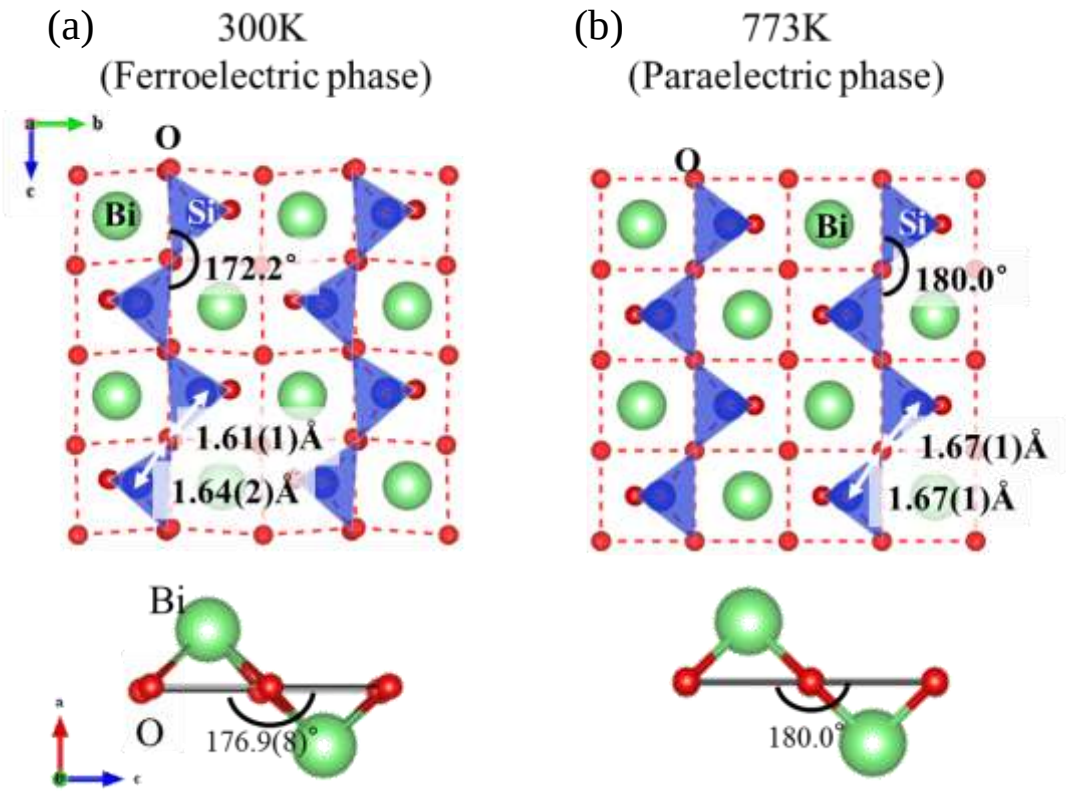

Figure 5-6. Structural distortion of Bi_2SiO_5 at (a) 300 K and (b) 773 K.

5.3 Ferroelectric polarization based on point charge model

At first, we estimated the polarization by point charge model. In this method, the information of structural distortion is significantly considered. The lattice parameters, atom position and formal charge (Bi^{3+}, Si^{4+}, O^{2-}) of each atom are used for calculation of the polarization value. The formal charge (Bi^{3+}, Si^{4+}, O^{2-}) was assumed. The equation for point charge model is equation (5-1)

$$\boldsymbol{P} = \frac{e}{V}\sum_j (q_j \times \delta \boldsymbol{d}_j) \qquad (5.1)$$

where e is the elementary charge (1.602×10^{-19} C) and V is the unit cell volume. q_j is the formal charge of jth ion, and $\delta \boldsymbol{d}_j$ is the displacement of jth ion between paraelectric and ferroelectric structure.

The obtained results were 4.9, 0 and 8.1 μC/cm^2 along *a*, *b* and *c* direction, respectively. (Table 5-6) However, it showed a large gap between point charge model and *PE*-hysteresis measurement for P_a. Because only change of position of ions with formal charge is taken into consideration for the point charge model, it doesn't include change of the electron density distribution in the calculation process or covalent characteristics between ions. In addition, electronic polarization in atom is not also considered. Thus, the point charge model is not appropriate method for estimation of polarization.

Table 5-6. Polarization value calculated by the point charge model.

$\mu C/cm^2$

	P_a	P_b	P_c
Point charge model	4.9	-	8.1
PE-hysteresis measurement	0.8	-	-
Theoretical calculation	0.1	-	14.5

5.4 Charge density study of Bi_2SiO_5

We found that the electron density distribution is also considered to study ferroelectric property of Bi_2SiO_5. For the electron density, MEM analysis was carried out Figure 5-7 (a) is a three-dimensional electron density imaging of Bi_2SiO_5 at 300 K. The isosurface is 0.8 e/Å^3. The blue color is the electron density for the SiO_3 layer and the green color is for the Bi_2O_2 layer. Figure 5-7 (b) is a two-dimensional charge density map in a region which is the sliced plane on center of silicon ion. The MEM charge density map in Figure 5-7 (b) is colored by the value of electron density from 0.6 e/Å^3 to 3.6 e/Å^3, and both layer show the distorted distribution of electron density. Bonding characteristics between layers is changed by the displacement of the SiO_3 layer to (-) *a*-direction. At 773 K, bonding length and bonding electron density for Bi(a)-O(g) and Bi(b)-O(h) were same. The bonding length and the value of bonding electron between Bi(a)/Bi(b) and O(g)/O(h) is 2.45(1) Å and 0.65(1) e/Å^3, respectively. On the other hands, bonding characteristics between the Bi_2O_2 and the SiO_3 layer was changed at 300 K; bonding charge density between Bi ion and O ion of the SiO_3 layer decreased, although bonding distance between Bi ion and O ion of the SiO_3 layer was decreased from 2.45(1) e/Å^3 to 2.37(1) e/Å^3 with cooling. The bonding electron density of Bi(a)-O(g) was decreased by 0.09 e/Å^3 and that of Bi(b)-O(b) was also decreased by 0.06 e/Å^3, respectively. Generally, it is known that bonding charge density increased as bonding length decreased. However, in Bi_2SiO_5, the covalent character between the Bi_2O_2 layer and the SiO_3 layer decrease; it seems that each layer is isolated,

although the layers are closed to each other at ferroelectric phase.

In order to investigate the change of electron density distribution in inner layer region caused by the reduced covalent characteristics between the Bi_2O_2 and the SiO_3 layer, we visualized MEM charge density with a two-dimensional map. Figure 5-8 shows the plane passing the center of cation and anion. The red color is high density region, and the blue color is low density region: they are colored from 0.6 e/Å^3 to 0.8 e/Å^3 for the Bi_2O_2 layer and from 0.75 e/Å^3 to 1.55 e/Å^3 for the SiO_3 layer. The bonding electron density, the minimum value of electron density between cation and anion, is listed in Table 5-7 for quantitative comparison of bonding characteristics.

The bonding electron in the SiO_3 layer shows higher value than that in the Bi_2O_2 layer. As temperature was decreased, the bonding electron density in the Bi_2O_2 layer and the SiO_3 layer were increased by 0.00~0.33 e/Å^3 and 0.00~0.28 e/Å^3, respectively, in comparison with that at paraelectric phase. In addition, bonding electron density as specific bonds, such as Bi(a)-O(a), Bi(a)-O(b), Bi(b)-O(d) and Bi(b)-O(c) bonds, significantly increased. Similarly, same tendency was also observed at Si-O(g) and Si-O(g) bonds in the SiO_3 layer. It showed the paired molecules in three-dimensional electron density imaging.

Figure 5-9 shows that the isosurface of MEM charge density with 0.85 e/Å^3 and 1.50 e/Å^3 for the Bi_2O_2 (blue color) and the SiO_3 (red color) layer, respectively. In the ferroelectric phase at 300 K, the Bi atoms form a stronger covalent network with one of the four equivalent first-neighbored O atoms at 773 K in the paraelectric phase. In addition, the Si atoms in the ferroelectric phase form a stronger covalent bond with three of the for-equivalent first-neighbored O atoms in the paraelectric phase, showing that the SiO_3 molecule. Formed molecules seem to form electric dipoles. They were represented as

arrows in Figure 5-9. The Bi(b)-O(b) and Bi(a)-O(c) pairs formed electric dipole, and the two neighboring electric dipoles formed almost antiparallel configuration in the Bi_2O_2 layer. On the other hand, the electric dipoles of SiO_3 molecule aligned to lead such like the ferroelectric configuration in the SiO_3 layer. As a result, the formation of molecules for BiO and SiO_3 in the layer was revealed with the 3-dimensional MEM charge density. In addition, visualized electric dipole moments in the molecules can explain why the large dipole moment of Bi_2SiO_5 originated from the light element of Si instead of the heavy element of Bi.

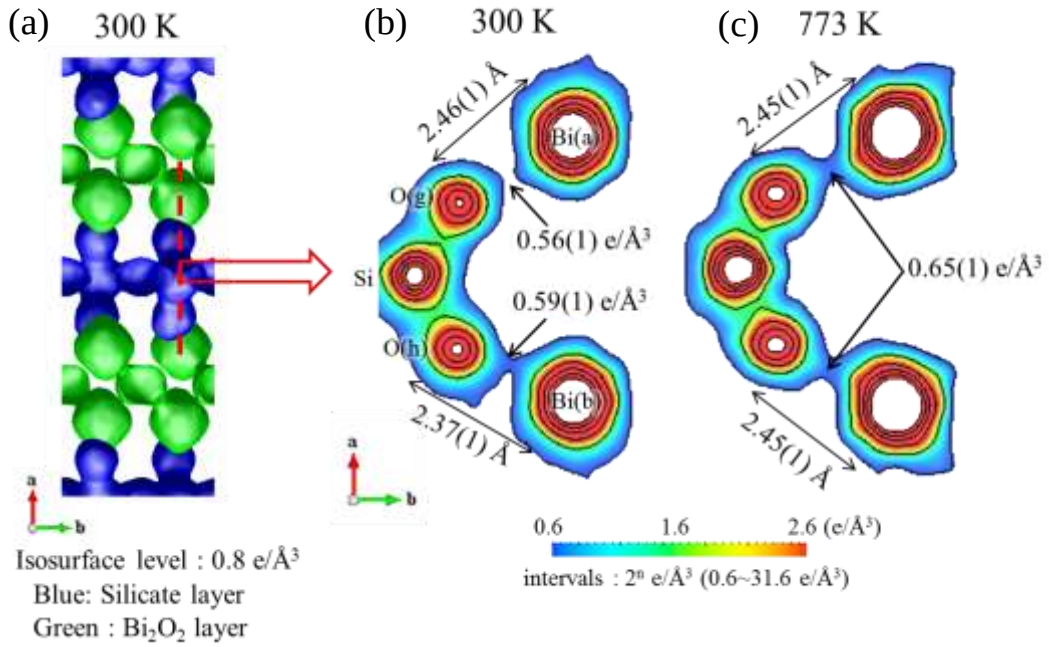

Figure 5-7. (a) Three-dimensional MEM charge density of Bi_2SiO_5 with 0.8 e/Å ^{3} isosurface level. Two-dimensional MEM charge density in inter-layer region at (b) 300 K and (c) 773 K.

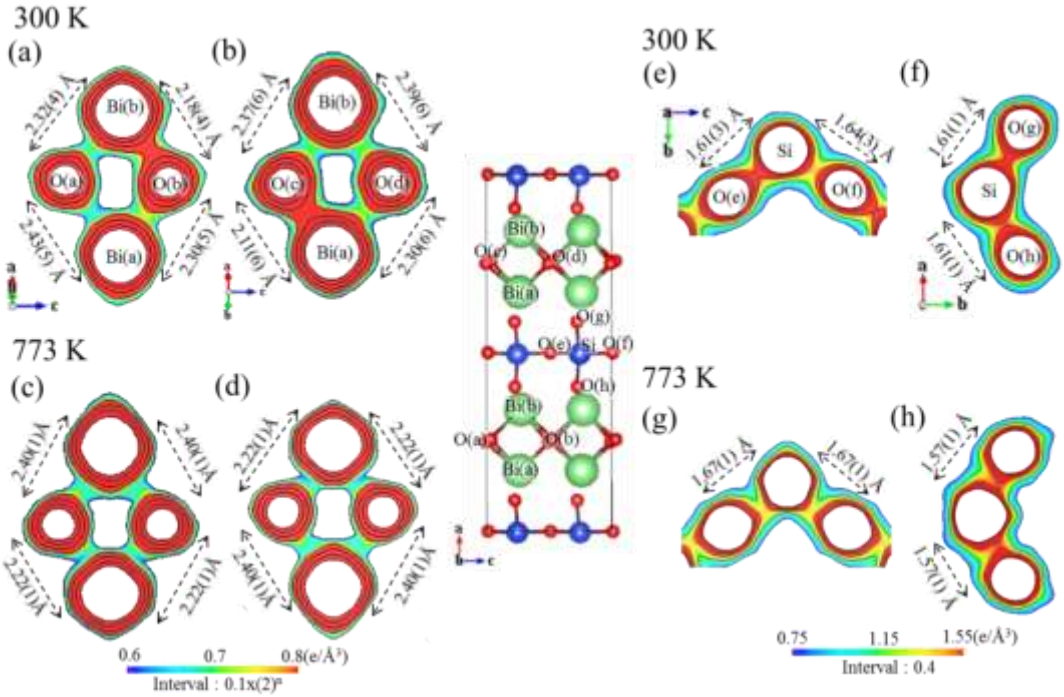

Figure 5-8. Two-dimensional MEM charge density of the Bi_2O_2 layer at (a, b) 300 K and at (c, d) 773 K. That of the SiO_3 layer at (e, f) 300 K and at (g, h) 773 K.

Table 5-7. Value of bonding electron density of Bi_2SiO_5.

$e/Å^3$

Cation	Anion	300 K	773 K
Bi(a)	O(a)	0.65(1)	0.65(2)
	O(b)	0.74(2)	0.65(2)
	O(c)	0.98(1)	0.65(1)
	O(d)	0.71(1)	0.65(1)
Bi(b)	O(a)	0.68(1)	0.65(1)
	O(b)	0.85(1)	0.65(1)
	O(c)	0.68(1)	0.65(2)
	O(d)	0.69(1)	0.65(2)
Si	O(e)	1.57(1)	1.29(8)
	O(f)	1.42(1)	1.29(8)
	O(g)	1.61(1)	1.54(3)
	O(h)	1.54(2)	1.54(3)

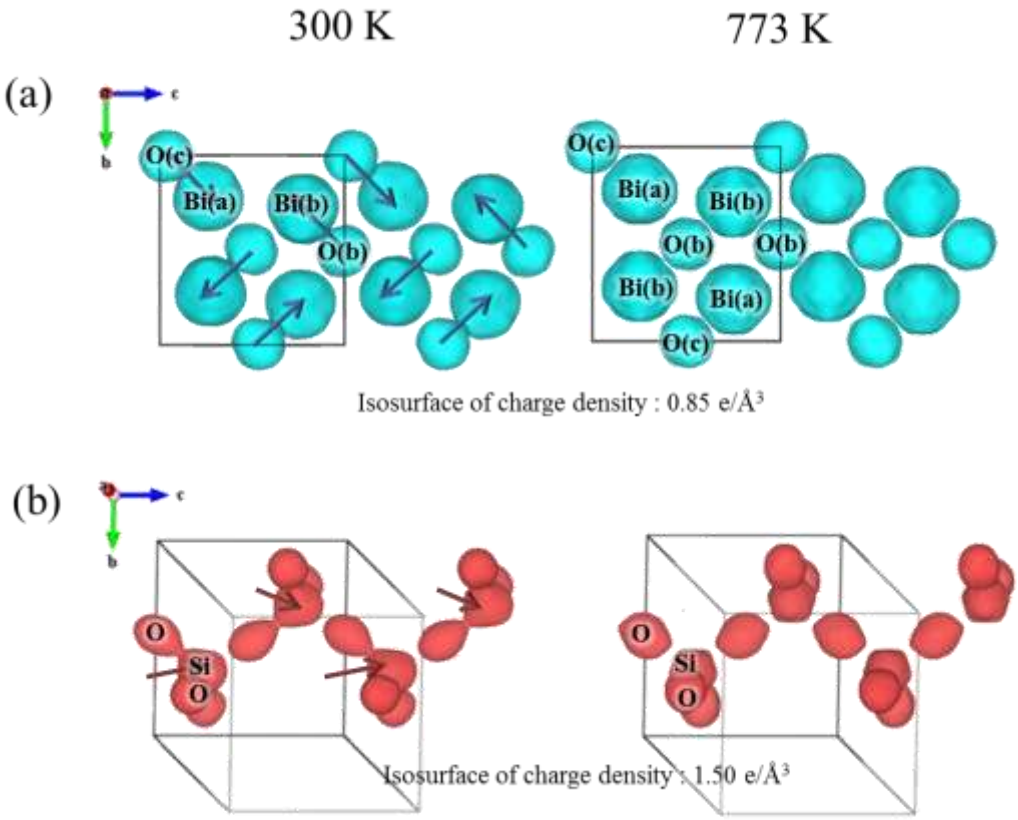

Figure 5-9. Three-dimensional MEM charge density (a) the Bi_2O_2 and (b) the SiO_3 layer.

5.5 Electrostatic potential change with ferroelectric phase transition

5.5.1 Visualization of the ferroelectric polarization

Electrostatic potential can visualize ionic/electronic polarization in a material. Electrostatic potential at 300 K and 773 K was analyzed in Figure 5-10. It shows the out-of-plane direction (*b*-*c* plane). Electrostatic potential is colored from 25.9 V to 40.3 V: red is high potential (40.3 V) and blue is low potential (25.9 V) region, respectively. As seen in Figure 5-10, there was a large difference of electrostatic potential between ferroelectric and paraelectric phase. For 773 K, small difference of the electrostatic potential between anion and cation was observed. On the other hands, for 300 K, distinct difference of electrostatic potential appeared at both layers which have off-center structural distortion for electron density distribution. Such phenomena are indicated as ionic polarization the previous research.[21] A significantly enhanced ionic polarization of each layer at 300 K is strongly associated to the ferroelectricity of Bi_2SiO_5 material. When we examined change of electrostatic potential on each layer at 300 K, the color gradation was observed at Si atom in the SiO_3 layer. It means the SiO_3 layer has atomic polarization caused by distortion of electron density distribution toward (-) *c* direction relative to center of nucleus charge.

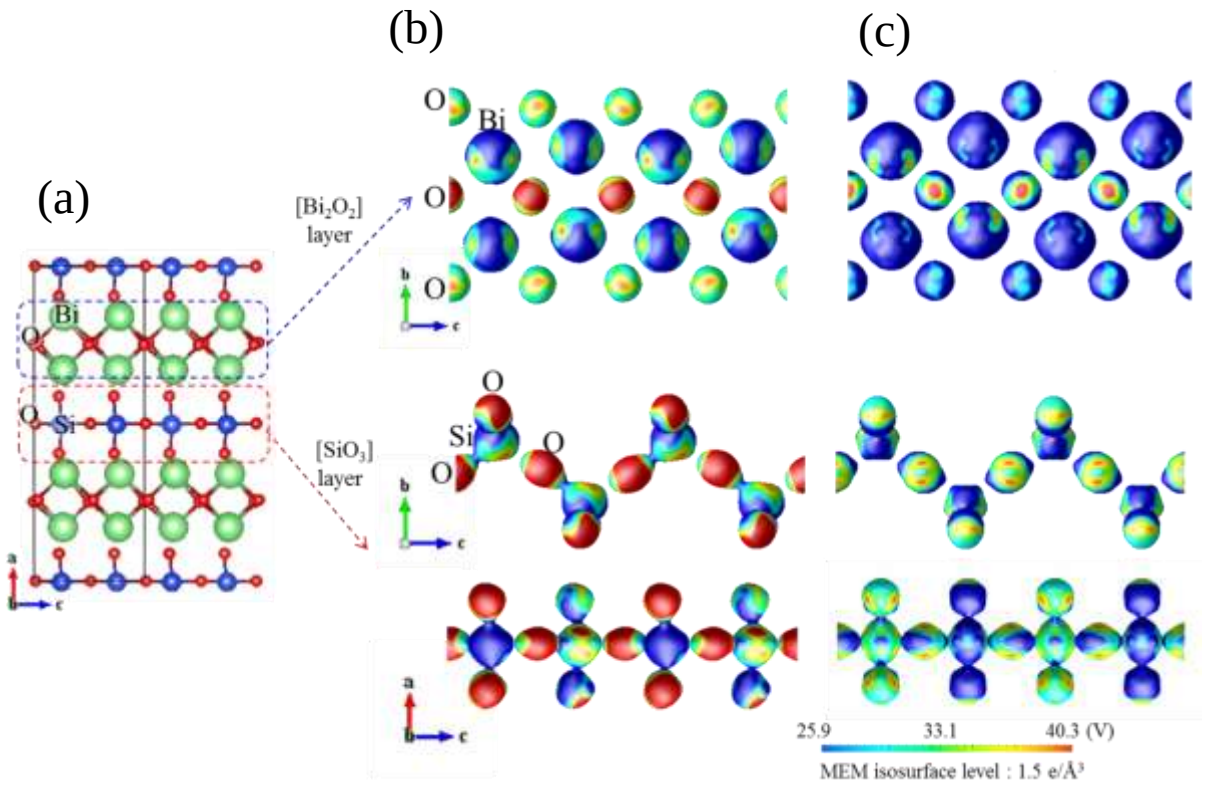

Figure 5-10. (a) Crystal structure of Bi_2SiO_5 and three-dimensional electrostatic potential distribution at (b) 300 K and (c) 773 K.

5.5.2 Determination of the fragments in the structure

In order to estimate the values of ionic polarization quantitatively, the MaxEnt/fragment EP method was applied. We verified that this method is powerful for polarization estimation in the system with ionic character. For using this method, we determined the fragment in layers. Figure 5-11 shows a two-dimensional electrostatic potential map on (004) plane of Bi_2SiO_5 at 300 K, as an example for determination of fragment. Electrostatic potential is colored from -31 V to 31 V. The black arrows are the electric vectors calculated by the minus gradient of the electrostatic potential at each point. According to the determination method of fragment, we investigated the minimum bonding electrostatic potential between cation and anion. These values are listed in Table 5-8. At a first step, bonding electrostatic potential value of all bonds is compared: O(g) in Figure 5-11 has two neighboring bonds with Bi(a) and Si atoms with bonding electrostatic potential value -7.3(2) V and 19.9(7) V, respectively. The Si-O(g) is selected with higher value than that of Bi(a)-O(g); Si-O(g) bond is pared for fragment. Same process is also applied to other bonds. Finally, obtained fragments are Bi(a)-O(c), Bi(b)-O(b) and Si-O(e)-O(g)-O(h).

MEM electron density has continuous distribution in terms of pixels in the unit cell. To estimate the local polarization in the fragment, it is required to determine the boundary of fragment. In this case, the boundary was determined by following the point which has the local minimum value of electrostatic potential. At that point, electrostatic interaction between fragments was minimized. Figure 5-13 shows the electrostatic potential value along the path between Bi(a) and O, which corresponded to the inter fragments region. At the position of atoms, they show the local maximum value of electrostatic potential. As the

point gets apart from the position of atom, the value of electrostatic potential is lower and it finally reached to the minimum point for electrostatic potential as indicated by an arrow in Figure 5-13. By following these kinds of the local minimum points around fragment, it is possible to determine the boundary of fragments. Determined boundary for SiO_3 fragment was indicated as white dotted lines in Figure 5-11.

Same process was also applied to the Bi_2O_2 layer. Figure 5-12 shows a two dimensional electrostatic potential map on (011) plane. It was colored from -28.8 V to 288.0 V. In order to show high and low electrostatic potential at the same time, two kinds of color ranges were used. Equipotential lines are drawn from -28.8 V to 0.0 V with 7.2 intervals in low electrostatic potential region and from 0.0 V to 288.0 V with 72.0 V intervals in high electrostatic potential region, respectively. When the bonding electrostatic potential values were compared, Bi(a)-O(c) and Bi(b)-O(b) bonds show the highest value among the four equivalent first-neighbored O bonds with the 6.9(1) V and 4.8(2) V, respectively. Using this result, fragments in the Bi_2O_2 layer were designated. The boundary for the fragments was indicated as white dotted lines in Figure 5-12, which is determined based on the minimum value of electrostatic potential value around fragments.

Determined fragments for BiO and SiO_3 were listed in Table 5-9. Yellow color in the Table 5-9 is the boundary of determined fragments and blue color is electron density of 0.8 e/$Å^3$ isosurface. As shown in the Table 5-9, fragment method can determine the local structure enclosed by the minimum value of electrostatic potential. Total number of electron charge in the each fragment was same with total nucleus charge, showing the charge neutrality of fragments.

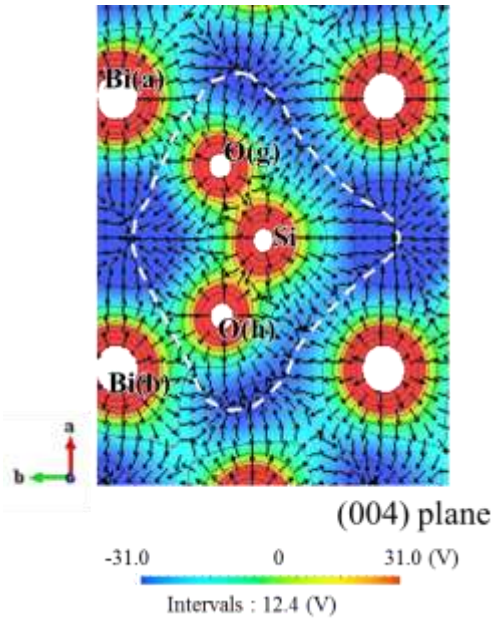

Figure 5-11. Electrostatic potential map on (004) plane of Bi_2SiO_5 at 300 K.

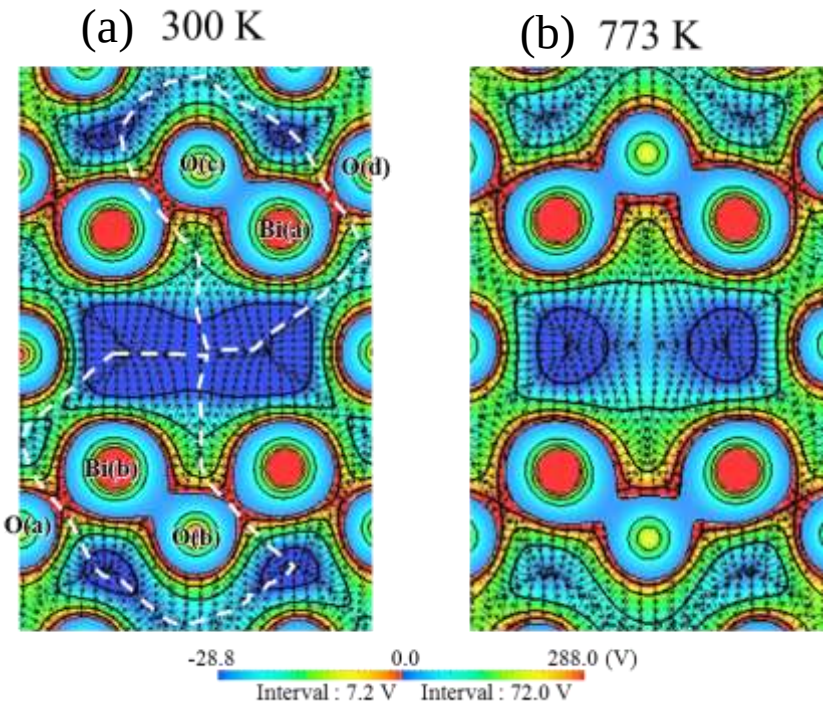

Figure 5-12. Two-dimensional electrostatic potential map on (011) plane of Bi_2SiO_5 at (a) 300 K and (b) 773 K.

Table 5-8. Bonding electrostatic potential value of Bi_2SiO_5.

V

Anion	Cation	300 K	773 K
O(a)	Bi(a)	-7.8(3)	-7.1(3)
	Bi(b)	-1.2(1)	3.5(2)
O(b)	Bi(a)	-3.6(4)	-7.1(3)
	Bi(b)	4.8(2)	3.5(2)
O(c)	Bi(a)	6.9(1)	3.5(2)
	Bi(b)	-6.3(3)	-7.1(3)
O(d)	Bi(a)	-1.3(3)	3.5(2)
	Bi(b)	-6.6(4)	-7.1(3)
O(e)	Si	27.8(4)	20.3(4)
O(f)	Si	25.9(1)	20.3(4)
O(g)	Bi(a)	-7.3(2)	-9.8(2)
	Si	19.9(7)	23.9(1)
O(h)	Bi(b)	-4.3(4)	-9.8(2)
	Si	20.3(1)	23.9(1)

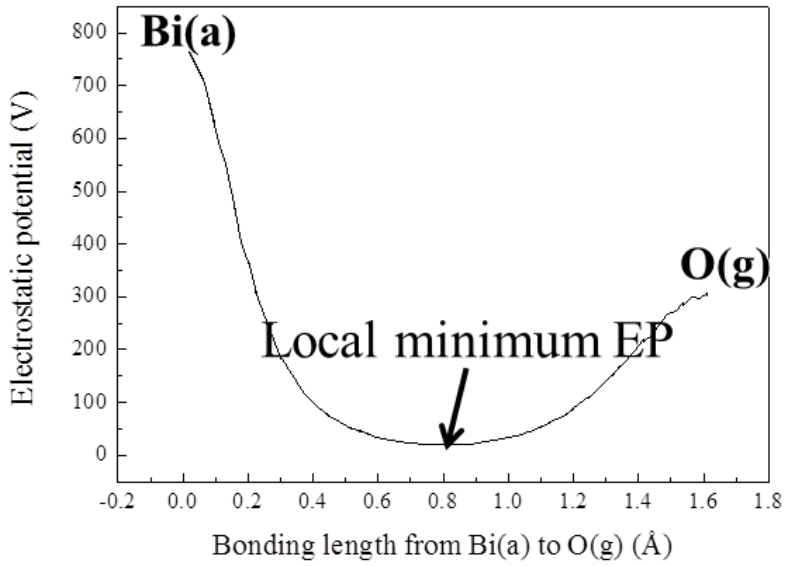

Figure 5-12. Change of electrostatic potential between Bi(a) and O(g).

Table 5-9. Nucleus and electron charge in fragment of Bi_2SiO_5.

	SiO_3	Bi(a)-O(c)	Bi(b)-O(b)
	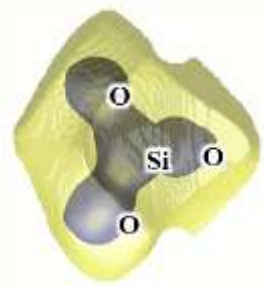	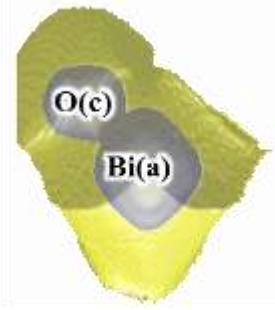	
Nucleus charge	38	91	91
electron charge	37.99(1) e	91.01(1) e	91.01(1) e

5.6 Local polarization of the BiO and SiO_3 fragment by the MaxEnt/fragment EP method

We applied the MaxEnt/fragment EP method to estimate the polarization in Bi_2SiO_5. Position of nucleus charge from Rietveld refinement and electron density distribution within fragment are used for calculation of polarization with equation (2.32).

Obtained results are listed in Table 5-10. Polarization along *b* (P_b) axis was zero because of inversion symmetry operation in *Cc* space group of Bi_2SiO_5 at 300 K. BiO fragments showed polarization value along the *a* and the *c* axis with relatively large value. However, the direction of polarization at each BiO fragment was different to each other. As a result, it led quite small net polarization in the Bi_2O_2 layer. On the other hands, the SiO_3 layer showed a large polarization along the *c*-axis with 27.3(1) μC/cm^2. By using the polarization value at each layer, the total P_a and P_c of Bi_2SiO_5 was 0.3(2) μC/cm^2 and 23.5(1) μC/cm^2 for the *a* and the *c* axis, respectively. These results were compared to the reported result. The value of P_a was consistent with the value of the theoretical calculation and *PE*-hysteresis measurements. In addition, existence of large polarization along the *c*-axis was also demonstrated with experimental method. Thus, we show the obtained polarization P_a and P_c from the MaxEnt/fragment EP method is in good agreement with the reported results.

The MaxEnt/fragment EP method can estimate the local polarization in fragment. For Bi_2SiO_5, polarization in the Bi_2O_2 and the SiO_3 layer was quantitatively estimated. Small difference of polarization between Bi_2O_2 and the SiO_3 along the *a* axis lead small value of P_a in Bi_2SiO_5 material. On the other hands, intensity of P_c at the SiO_3 layer was

apparently larger than that at the Bi_2O_2 layer. Therefore, it was found that large polarization P_c in Bi_2SiO_5 originated from SiO_3 layer of light elements not from the heavy Bi_2O_2 layer.

Based on the polarization result at each fragment, we represented the schematic view of polarization. Figure 5-14 shows the local polarization in fragment (left) and layer (right). Intensity and direction of polarization was expressed as arrow in the figure and it was normalized for comparison. In the Bi_2O_2 layer, polarization direction of BiO fragments was different to each other, such like antiferro configuration. It caused small value of polarization in the Bi_2O_2 layer by offsetting each other. On the other hand, SiO_3 layer showed ferroelectric ordering, it was supposed to relate to large polarization along *c*-axis. SiO_3 fragment and BiO fragment showed a relation of antiferro configuration. This antiferro configuration made the coupled layer as indicated in Figure 5-14. In addition, the couple layer was departed by ferroelectric configuration between BiO and SiO_3 fragment. It resulted in the displacement of SiO_3 layer to the (-) *a*-axis direction. We assumed large ferroelectric polarization of SiO_3 layer is stabilized by a local anti-ferroelectric configuration with BiO local layer.

Table 5-10. Polarization of Bi_2SiO_5 by the MaxEnt/fragment EP method.

$\mu C/cm^2$

		Polarization	Projected Polarization		
		$\|P\|$	P_a	P_b	P_c
MaxEnt/fragment EP method	**Bi_2O_2 layer**	**4.21(7)**	**-1.8(1)**	**0**	**-3.8(1)**
	Bi(b)-O(b) sublayer	26.8(3)	24.0(2)	0	-11.9(1)
	Bi(a)-O(c) sublayer	27.0(4)	-25.8(4)	0	8.0(1)
	SiO_3 layer	**27.3(1)**	**1.4(1)**	**0**	**27.3(1)**
	Bi_2SiO_5	**23.5(1)**	**0.3(2)**	**0**	**23.5(1)**
PE measurement[51]	Bi_2SiO_5	-	0.8	-	-
First-principle calculation[51]	Bi_2SiO_5	14.5	0.1	0	14.5
PC model	Bi_2SiO_5	9.4	4.9	0	8.1

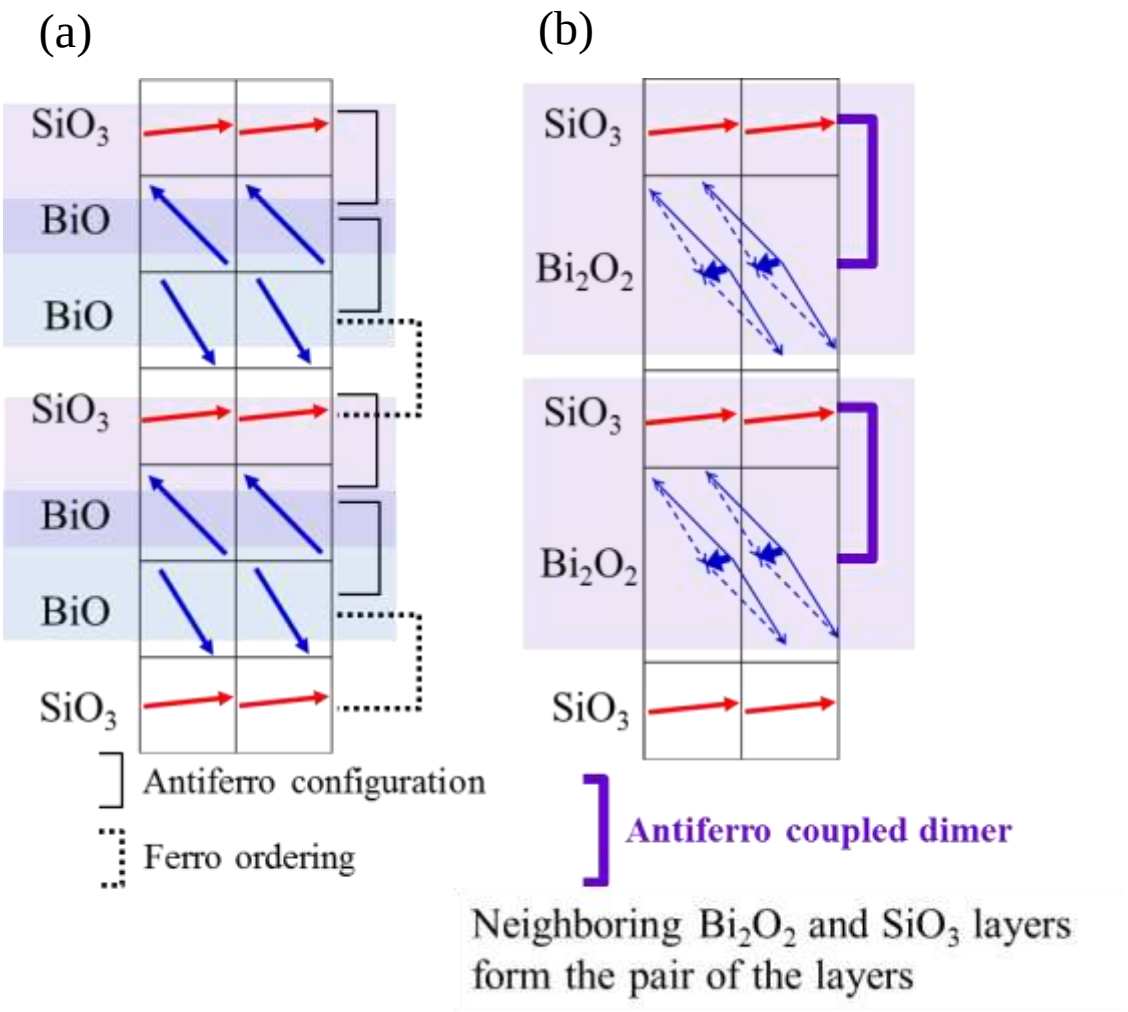

Figure 5-13. Schematic view of polarization at (a) each fragment in Bi_2SiO_5 and (b) antiferro coupling between the SiO_3 and Bi_2O_2 layer.

Chapter 6

Summary

We have developed a novel estimation method, the MaxEnt/fragment EP method, of ferroelectric polarization by means of Synchrotron Radiation X-ray powder diffraction. T his is a new approach to estimate the local/total polarization based on the structural information such as lattice parameter, atom position, electron density and electrostatic potential. It should be emphasized that this method only needs a tiny amount of the powder samples. Through validity test of this method using $BaTiO_3$ and $PbTiO_3$ powder sample, we found that this is an appropriate method for order estimation of polarization value; it is a powerful method to estimate the local/total polarization in the system with strong ionic bonding character.

The MaxEnt/fragment EP method was applied to the estimation of ferroelectric polarization of Bi_2SiO_5 which has an isolated the SiO_3 and the Bi_2O_2 layer. We found that this material has a large polarization along the *c*-axis, and it originated from the SiO_3 layer having ferroelectric configuration. Although Bi-O molecule has a large polarization along the *a*-axis, their antiparallel alignments cancel out the polarization in the Bi_2O_2 layer. As a result, the dipole is ordered hierarchically. The hierarchical dipole ordering in crystal structure stabilizes the ferroelectric configuration of the SiO_3 layer resulting in a large

polarization P_c in Bi_2SiO_5. This result provides that the newly developed our approach is a powerful and widely applicable method to visualize the local polarization and their ordering states in crystal system using only a few microgram powder samples.

For the future work, I would like to find a way to enhance the MaxEnt/fragment EP method and apply it for the design of the novel material.

As it was shown in the example of Perovskite materials, the MaxEnt/fragment EP method resulted in a little gap of the obtained polarization for the high covalent character system; high covalency between fragments reduced the polarization value. However, the reason why the MaxEnt/fragment EP method cannot provide the good polarization value is not still clear. In order to improve the method, at first, I would like to increase the total number of pixel in a unit cell. In the calculation process, the electron density was quantized at each pixel. If we increase the number of pixel, it is possible to obtain more accurate boundary and the electron density distribution for each fragment as well as the obtained polarization value. Secondly, this MaxEnt/fragment EP method was applied to only 1 unit cell. Thus, if we increase the number of unit cell as many as possible, it is expected to have the converged value of ferroelectric polarization.

As an application of the MaxEnt/fragment EP method, we think that this method can be used for the designing of the novel material. The MaxEnt/fragment EP method revealed the ferroelectric polarization at each local structure, for example, it was found that the polarization of Bi_2SiO_5 is originated from the SiO_3 layer. Because the SiO_3 layer has a form of one-dimensional chains of the SiO_4 tetrahedral unit, it is easy to cause the structural displacement of SiO_3 layer by the change of environment. Change of the SiO_3 layer structure is directly related to the ferroelectric polarization of Bi_2SiO_5, and it is supposed to

enhance the property of Bi_2SiO_5. Therefore, the MaxEnt/fragment EP method is expected to provide a part of useful guidance to manipulate the local structure for further development of materials. We believe this will contribute to the development of green environment materials and devices in various scientific fields.

References

1 G. H. Haertling, *J. Am. Ceram. Soc*. **82**, 797 (1999).

2 Y. Chung *et al*., *Nano Lett*., **11**, 1161 (2011).

3 H.Yamada, T. Yoshimura and N. Fujimura, *Jpn. J. Appl. Phys*. **51**, 11PB01 (2012).

4 A. Schilling, R. M. Bowman, G. Catalan, J. F. Scott and J. M. Gregg, *Nano Lett*., **7**, 3787 (2007).

5 Y. S. Kang *et al*., *Appl. Phys. Lett*. **88**, 123508 (2006).

6 Y. S. Kang *et al*., *Proc*. *SPIE*, **6121**, 61210S (2006).

7 K. Aizawa and H. Ishiwara, *Jpn. J. Appl. Phys*. **31**, 3232 (1992).

8 A. Masuda *et al*., *J. Cryst. Growth* **189/190**, 227 (1998).

9 R. Yimnirun, S. Ananta and P.Laoratakul, *CMU. Journal*, **3**, 53 (2004).

10 W. Zhong, D. Vanderbilt and K. M. Rabe, *Phys, Rev. B*. **52**, 6301 (1995).

11 S. Suzuki *et al*., *Phys, Rev. B*. **86**, 060102(R) (2012).

12 H. Chaib, T. Otto and L. M. Eng, *phys.stat. sol*. (b) **233**, 250 (2002).

13 M. Rieth and W. Schommers, *Handbook of Theoretical and Computational Nanotechnology*, American Scientific Publisher (2006).

14 S. Chomnilpan, R. Liminga and R. Tellgren, *J. Appl. Cryst*. **13**, 176 (1980).

15 Y. Iwata, *J. Phys. Soc. Jpn*. **43**, 961 (1977).

16 C. Gatti and P. Macchi, *Modern Charge-Density Analysis*, Springer (2012)

17 M. Sakata and M. Sato, *Acta Cryst. A* **46**, 263 (1990).

18 M. Takata *et al*., *Nature,* **377**, 46 (1995).

19 M. Takata, *Acta Cryst. A* **64**, 232 (2008).

20 M. Takata and M. Sakata, *Acta Cryst. A* **52**, 287 (1996).

21 H. Tanaka, Y. Kuroiwa and M. Takata, *Phys. Rev. B* **74**, 172105 (2006).

22 H. Tanaka, Y. Kuroiwa and M. Takata, *J. Korean Phys. Soc*. **55**, 803 (2009).

23 C. R. Wang *et al., Nature,* **408**, 426 (2000).

24 Y. Kubota *et al*., *J. Phys. Condens. Matter.* **12**, 1253 (2000).

25 J. Kim, H. Tanaka, K. Kato, M. Takata and Y. Moritomo, *Appl. Phys. Express* **4**, 25801 (2011).

26 A. Fujiwara *et al*., *Phys. Rev. B.* **85**, 144305 (2012).

27 Y. Kuroiwa *et al*., *J. Korean Phys. Soc*. **46**, 296 (2005).

28 D. Damjanovic, *Rep. Prog. Phys*. **61**, 1267 (1998).

29 H. Ibach and H. Luth, *Solid-state Physics*, 3rd edition, Springer (2003).

30 R. E. Newman, *Properties of Materials*, Oxford University Press (2005).

31 Kittel, C. *Introduction to solid state physics*; Wiley New York (1996).

32 M. Lines and A. Glass, *Principles and applications of ferroelectrics and related materials*. Clarendon Press, Oxford (1979).

33 M. B. Boisen and G. V. Gibbs, *Am. Mineral*. **61**, 145 (1976).

34 D. B. Litvin, *Acta Cryst. A***42**, 44 (1986).

35 B.E. Warren, *X-ray Diffraction*. New York (1969).

36 B.D. Cullity, *Elements of X-Ray Diffraction* (2nd), Addison-Wesley Publishing Company (1978).

37 E. E. Lattman, *Acta Cryst. A***28**, 220 (1972).

38 S. F. Gull and G. J. Daniell, *Nature*, **272**, 686 (1978).

39 D. M. Collins, *Nature*, **298**, 49 (1982).

40 Grant, W.R. Phillips, *Electromagnetism* (2nd ed.). Manchester Physics, John Wiley & Sons (2008).

41 P. Matthews, *Vector Calculus*. Springer (1998).

42 D. E. Dugdale, *Essentials of Electromagnetism*. Springer (1993).

43 R. Tilley, *Understanding Solids*, Wiley, (2004).

44 J. C. Cramer, *Essentials of computational chemistry* (2 ed.) Wiley (2004).

45 R. Resta and D.Vanderbilt, *Theory of Polarization: A Modern Approach. Topics Appl. Physics* **105**, 31 (2007).

46 N. A. Spaldin, *J. Solid. State. Chem*. **195**, 2 (2012).

47 T. Gohda, M. Ichikawa, T. Gustafsson and I. Olovsson, *Acta Cryst*. B **56**, 11 (2000).

48 H. Tanaka *et al*., *J. Appl. Cryst*. **35**, 282 (2002).

49 H. L. Monaco, *Experimental Methods in X-ray Crystallography, in Fundamentals of Crystallography*, edited by C. Giacovazzo, Oxford University Press (1992).

50 E. M. Wilks and J. Wilks, *MINERAL MAG.* **51**, 746 (1987).

51 H.Taniguchi, *et al*., *Angew. Chem. Int. Ed.* **52**, 8088 (2013).

52 K. D. Rouse *et al*., *Acta Cryst*. A **26**, 682 (1970).

53 A. W. Hewat, *Acta Cryst*. A **35**, 248 (1979).

54 J. Valasek. *Physical Review*, **17**, 475 (1921).

55 W. J. Lee, H. G. Kim and S. G. Yoon, *J. Appl. Phys*. **8**0, 5891 (1996).

56 Wenk, Hans-Rudolf, Bulakh, Andrei, *Minerals: Their Constitution and Origin*, New York, NY: Cambridge University Press (2004).

57 V. K. Wadhawan, *Introduction to ferroic materials*, CRC Press (2000).

58 F. Jona and G. Shirange, *Ferroelectric Crystals, Monographs on Solid State Physics*, Pergamon, Oxford (1962).

59 T. Higuchi *et al*., *Jpn. J. Appl. Phys*. **38**, 5667 (1999).

60 K. Miura and M. Tanaka, *Jpn. J. Appl. Phys.* **37**, 6451 (1998).

61 R. E. Cohen and H. Krakauer, *Phys. Rev. B*, **42**, 6416 (1990).

62 R. E. Cohen, *Nature*, **358**, 136(1992).

63 J.P. Remeika *et al*., Mater. Res. Bull. **5**. 37 (1970).

64 M.J. Haun, E. Furman, S. J. Jang, H.A. Mckinstry and L. E. Cross, *J. Appl. Phys.* **62**, 3331 (1987).

65 E. K. Akdogan, C. J. Rawn, W. D. Porter, E. A. Payzant and A. Safari, *J. Appl. Phys.* **97**, 084305 (2005).

66 Li Sun *et al*., *Appl. Phys. Lett*. **68,** 3728 **(**1996).

67 T. Qi, I. Grinberg and A. M. Rappe, *Phys. Rev. B*, **82**, 134113 (2010).

68 J. Shieh, J.H. Yeh, Y.C. Shu and J.H. Yen, *Materials Science and Engineering* B **161**, 50 (2009).

69 J.E. Huber, *Curr. Opinion. Solid State Mater. Sci.* **9**, 100 (2005).

70 V. Wadhawan. *Introduction to ferroelectric materials*, CRC press (2000).

71 H. H. Wieder, *Phys. Rev.* **99**, 1161 (1955).

72 M. Fechner, S. Ostanin and I. Mertig, *Phys. Rev. B* **77**, 094112 (2008).

73 S. H. Wemple, M. Didomenico, Jr. and I. Camlibel, *J. Phys. Chem. Solids* **29**, 1797 (1968).

74 J. J. Wang, F. Y. Meng, X. Q. Ma, M. X. Xu and L. Q. Chen, *J. Appl. Phys*. **108**, 034107 (2010).

75 S. C. Jeon *et al*., *J. Am. Ceram. Soc*. **95**, 2435 (2011).

76 M. T. Buscaglia *et al*., *Chem. Mater*., **18**, 4002 (2006).

77 G. Liu *et al*., *J. Appl. Phys*. **98**, 044105 (2005).

78 T. Lee and I. A. Aksay, *Cryst. Growth Des.* **1**, 401 (2001).

79 L. Hong, Y. Li, P. Wu and L. Chen, *J. Appl. Phys*. **114**, 144103 (2013).

80 Y. Kuroiwa, *et al*., *Phys. Rev. Lett.* **87**, 217601 (2001).

81 C. Pirovano, M. S.Islam, R. N.Vannier, G. Nowogrocki and G. Mairesse. *Solid State Ionics* **140**, 115 (2001).

82 S. Georges, F. Goutenoire and P. Lacorre, *J. Solid. State. Chem.* **179**, 4020 (2006).

83 B. H. Park, B. S. Kang, S. D. Bu, T. W. Noh, J. Lee and W. Jo, *Natur*e, **401**, 682 (1999).

84 M. Takashi, Y. Hiroyuki, W. Hitoshi and P. de Araujo Carlos A, *Jpn. J.Appl. Phys.* **34**, 5233 (1995).

85 B. S. Kang, B. H. Park, S. D. Bu, S. H. Kang and T. W. Noh, *Appl. Phys. Lett*., **75**, 2644 (1999).

86 R. Seshadri and N. A. Hill, *Chem. Mater*. **13**, 2892 (2001).

87 J. B. Neaton, C. Ederer, U. V. Waghmare, N. A. Spaldin and K. M. Rabe, *Phys. Rev. B*, **71**, 014113(2005).

88 T. Kijima and H. Matsunaga, *Jpn. J. Appl. Phys*. **37**, 5171 (1998).

89 J. Harjuoja, S. Vayrynen, M. Putkonen, L. Niinisto and E. Rauhala, *J. Cryst. Growth* **286**, 376 (2006).

90 *International Tables for Crystallography* A

Abstract

Designing and controlling of electric polarization in solids are vital for emerging electronics, such as high-performance field-effect transistors, Ferroelectric Random Access Memories (FeRAMs) and multiferroic devices in nano-scale. Neither microscopic characterization nor design of individual dipoles, however, has been intensively investigated so far: the properties have been mainly described in terms macroscopic properties based on measurements of dielectric permittivity and electric polarization *P* under electric field *E* for bulk samples. Recently, the electrostatic potential (EP) analysis based on the electron charge density using Maximum Entropy Method (MEM), what we call MaxEnt/EP, has been developed for the characterization of specific features originating from the electrostatic field/force in microscopic scale. Using the MaxEnt/EP analysis, the relationship between internal electric field and physical properties was successfully visualized; based on the visualized result, thermal conductivity affected by rattling and superconductivity related to the bipolaron were understood in aspect of density level crystal structure.

In this research, we introduced the concept of fragment, which is determined by electrostatic potential boundary around particular pair in addition to the MaxEnt/EP method; we quantitatively investigated a local polarization in the fragment. In order to verify the validity of this method, the polarization of typical pervoskite materials, $PbTiO_3$ and $BaTiO_3$ were estimated. Furthermore, we applied the MaxEnt/fragment EP method to the polarization estimation of Pb-free novel ferroelectrics, Bi_2SiO_5.

In visualized electron density of $PbTiO_3$ and $BaTiO_3$, enhanced covalency property between cation and anion was observed at the ferroelectric phase in both materials; this covalent property was significantly enhanced in $PbTiO_3$ than in $BaTiO_3$. The enhanced covalency is strongly related to large polarization value. Using the MaxEnt/fragment EP method, we estimated to polarization value of $PbTiO_3$ and $BaTiO_3$. We found that polarization estimated by the MaxEnt/fragment EP method is in good accordance with the previous results; this method is a powerful for the estimation of polarization in the system with weak electrostatic potential interaction between fragments.

The method is applied to the Bi_2SiO_5 material, which has unmeasurable ferroelectric polarization along the specific axis due to facet feature of the fabricate sample. We have precisely determined the crystal structure of layered structure Bi_2SiO_5, which composed of the SiO_3 and the Bi_2O_2 layers. The material has structural phase transition from orthorhombic phase with *Cmcm* space group to monoclinic phase with *Cc* space group. In addition, charge density level structure visualized the ionic polarization of Si-O and Bi-O at ferroelectric phase. Using the result of electron density level structure, we estimated the polarization at each layer of Bi_2SiO_5. As a result, the SiO_3 layer was primary component of large polarization in the Bi_2SiO_5. The dipole of layers was visualized with hierarchical order. We deduce that the dipole order stabilized the strong ferroelectric configuration of the SiO_3 layer. Thus, these results provide that the newly developed approach is powerful and widely applicable method to visualize the local polarization and their ordering states in crystal system using only a few microgram powder samples. Furthermore, the information of local electric polarization patterns will conduce to designing and developing a novel high potential material.

Acknowledgement

First of all, my deepest appreciation must go to my supervisor Professor Masaki Takata of the University of Tokyo (UTokyo) and RIKEN SPring-8 Center (RSC). He gave me not only plenty of perspective and kind advices in my research, but also continuous encouragement. Three-year experience in Takata Structural Materials Science Laboratory was very precious time for my life. I also would like to express my appreciation to the RIKEN International Program Associate Program for full financial support. At the same time, I also thank all other committee members, Professor Yoshiyuki Amemiya of UTokyo, Professor Kaoru Kimura of UTokyo, Professor Takahisa Arima of UTokyo, Professor Yuji C. Sasaki of UTokyo and Professor Yoshihiro Iwasa of UTokyo for their valuable comments and suggestions.

I would like to offer sincere thanks to Professor Akihiko Fujiwara of Japan Synchrotron Radiation Research Institute (JASRI) and Professor Eiji Nishibori of RSC. They provided me many critical comments and helped me a lot in my thesis work.

Especially, I am very grateful to Dr. Jungeun Kim of JASRI for her endless help from beginning to end of my research. Without her help, I would never have finished my Ph. D study in UTokyo.

My thanks should also go to all of co-research groups, especially, Professor Mitsuru Itoh of Tokyo Institute of Technology, Professor Hiroki Taniguchi of Nagoya University and Professor Hiroshi Tanaka of Shimane University.

During my study and thesis work for Ph. D course, there are many people provided guidance, valuable instruction and generous comment. I would like to thank all the people who have contributed to this work: Dr. Kenichi Kato of RSC, Dr. Kunihisa Sugimoto of JASRI, Dr. Hiroyuki Ohsumi of RSC, D. Bagautdin Bagautdinov of JASRI, Dr. Chulho Song of JASRI, Dr. Takashi Kosone of RSC, Dr. Samuel Tardif of RSC, Dr. Akihiro Hori of RSC, Dr. Hidetaka Kasai of RSC, and Ms. Alicia Manjon sanz of RSC.

Finally, I would like to thank my family for their love and patience.

2014. May. Younghun Kim